2008

# Damage Detection of Rotors Using Magnetic Force Actuator: Analysis and Experimental Verification

Alexander Hans Pesch
*Cleveland State University*

## Recommended Citation

Pesch, Alexander Hans, "Damage Detection of Rotors Using Magnetic Force Actuator: Analysis and Experimental Verification" (2008). *ETD Archive*. 666.
https://engagedscholarship.csuohio.edu/etdarchive/666

# DAMAGE DETECTION OF ROTORS USING MAGNETIC FORCE ACTUATOR: ANALYSIS AND EXPERIMENTAL VERIFICATION

ALEXANDER H. PESCH

Bachelor of Science in Mechanical Engineering

Ohio University

June, 2006

Submitted in partial fulfillment of requirements for the degree

MASTER OF SCIENCE IN MECHANICAL ENGINEERING

at the

CLEVELAND STATE UNIVERSITY

December, 2008

This thesis has been approved

for the Department of MECHANICAL ENGINEERING

and the College of Graduate Studies by

---

Dr. Jerzy T. Sawicki, Thesis Committee Chairperson
Department of Mechanical Engineering, CSU

---

Dr. John L. Frater
Department of Mechanical Engineering, CSU

---

Dr. Ana V. Stankovic
Department of Electrical and Computer Engineering, CSU

---

Dr. John D. Lekki
NASA Glenn Research Center

# ACKNOWLEDGEMENTS

I would first like to thank Dr. Jerzy T. Sawicki for his guidance and support and superior performance in the role of advisor and director of the Center for Rotating Machinery Dynamics and Control (RoMaDyC) at Cleveland State University where the research was conducted. Without Dr. Sawicki's mentoring, this work would not have been possible. His passion for research is an inspiration. I would also like to thank Dr. John L. Frater, Dr. Ana V. Stankovic, and Dr. John D. Lekki, who served on the thesis committee, for their time, counsel and evaluation.

I also recognize my lab mate Adam Wroblewski for his support and encouragement and Dave Epperly, Fenn College prototype machinist, for his expertise and aid with the test rig.

This work was funded by the NASA Aviation Safety and Security Program. My gratitude goes to NASA for making this work possible.

# DAMAGE DETECTION OF ROTORS USING MAGNETIC FORCE ACTUATOR: ANALYSIS AND EXPERIMENTAL VERIFICATION

ALEXANDER H. PESCH

## ABSTRACT

The ability to monitor the structural health of rotordynamic systems is becoming increasingly important as critical components continue to be used despite aging and the associated potential for damage accumulation. The aim of this thesis is to investigate a novel structural health monitoring approach for the detection of damage in rotating shafts, which utilizes a magnetic force actuator for applying multiple types of force inputs on to a rotating structure for analysis of resulting outputs. The magnetic actuator will be used in conjunction with conventional support bearings and also be applied to rotor under full magnetic levitation. The results of numerical simulations of the cracked rotor system will be compared with experimental data obtained with the crack detection dedicated test rig.

# TABLE OF CONTENTS

APPENDICES

# NOMENCLATURE

$A$ = area of active magnetic bearing pole face [$\mathrm{m}^2$]

$\mathbf{a}$ = two dimensional x-y acceleration vector [$\frac{\mathrm{m}}{\mathrm{s}^2}$]

$\mathbf{C}$ = two dimensional x-y damping matrix [$\frac{\text{N-s}}{\mathrm{m}}$]

$C$ = active magnetic bearing force calibration factor [$\frac{\text{N-}\mu\mathrm{m}^2}{\mathrm{A}^2}$]

$c_y$ = damping in Y direction [$\frac{\text{N-s}}{\mathrm{m}}$]

$D_b$ = ball diameter in ball bearings [mm]

$e$ = eccentricity [m]

$\mathbf{F}$ = two dimensional x-y force vector [N]

$F$ = force from active magnetic bearing on rotor [N]

$f(\theta)$ = steering function that dictates if crack is open or closed [unitless]

$F_b$ = radial load on ball bearings [N]

$F_E$ = external excitation force from magnetic actuator [N]

$F_x$ = force in X direction [N]

$F_y$ = force in Y direction [N]

$g$ = acceleration due to gravity [$\frac{\mathrm{m}}{\mathrm{s}^2}$]

$g_{ap}$ = effective gap between active magnetic bearing pole and rotor [μm]

$I(s)$ = current flowing through active magnetic bearing coil [A]

$I_b$ = number of active rows in ball bearings

$I_{bias}$ = bias current in top and bottom active magnetic bearing coils [A]

$I_{bottom}$ = current in active magnetic bearing bottom coil [A]

$I_{control}$ = control current in active magnetic bearing system [A]

$I_{top}$ = current in active magnetic bearing top coil [A]

$\mathbf{K}$ = two dimensional x-y (stationary coordinates) stiffness matrix [$\frac{\mathrm{N}}{\mathrm{m}}$]

$\tilde{\mathbf{K}}$ = two dimensional $\zeta$- $\eta$ (rotating coordinates) stiffness matrix of healthy shaft [$\frac{\mathrm{N}}{\mathrm{m}}$]

$k$ = stiffness of healthy shaft in x and y direction [$\frac{\mathrm{N}}{\mathrm{m}}$]

$k_b$ = radial stiffness of ball bearings [$\frac{\mathrm{N}}{\mathrm{m}}$]

$\mathbf{K_{cr}}$ = two dimensional x-y (stationary coordinates) stiffness matrix of cracked shaft [$\frac{\mathrm{N}}{\mathrm{m}}$]
$\mathbf{\tilde{K}_{cr}}$ = two dimensional $\zeta$- $\eta$ (rotating coordinates) stiffness matrix of cracked shaft [$\frac{\mathrm{N}}{\mathrm{m}}$]
$k_i$ = linearized active magnetic bearing current stiffness [$\frac{\mathrm{N}}{\mathrm{A}}$]
$k_q$ = linearized active magnetic bearing position stiffness [$\frac{\mathrm{N}}{\mu\mathrm{m}}$]
$k_y$ = stiffness in Y direction [$\frac{\mathrm{N}}{\mathrm{m}}$]
$k_\eta$ = stiffness in $\eta$ direction [$\frac{\mathrm{N}}{\mathrm{m}}$]
$k_\zeta$ = stiffness in $\zeta$ direction [$\frac{\mathrm{N}}{\mathrm{m}}$]
$L$ = inductance of active magnetic bearing coil [H]
$\mathbf{M}$ = two dimensional x-y mass matrix [kg]
$m$ = mass [kg]
$N$ = number of windings in an active magnetic bearing coil
n = any integer, used in combinational frequency equation
$\mathbf{q}$ = two dimensional x-y position vector [m]
$q$ = lateral displacement of the rotor in active magnetic bearing [µm]
$\mathbf{q_{dy}}$ = dynamic component of position vector $\mathbf{q}$ [m]
$\mathbf{q_{st}}$ = static component of position vector $\mathbf{q}$ [m]
$R$ = resistance of active magnetic bearing coil [Ω]
$\mathbf{T}$ = transformation matrix from rotating to stationary coordinates
$t$ = time [s]
$V(s)$ = voltage supplies to active magnetic bearing coil [V]
$x$ = displacement in X direction [m]
$y$ = displacement in Y direction [m]
$Z$ = number of balls in ball bearings
$\alpha$ = angle of active magnetic bearing pole face [rad]
$\Delta k_\eta$ = reduction in stiffness in $\eta$ direction due to crack [$\frac{\mathrm{N}}{\mathrm{m}}$]
$\Delta k_\zeta$ = reduction in stiffness in $\zeta$ direction due to crack [$\frac{\mathrm{N}}{\mathrm{m}}$]
$\mu_0$ = permeability of a vacuum [$\frac{\mathrm{H}}{\mathrm{m}}$]
$\theta$ = angle of rotation [rad]

$\theta_b$ = contact angle in ball bearings [degrees]

$\psi$ = angle between whirl vector and crack direction [rad]

$\mathbf{\Omega}$ = combinational frequency [ $\frac{\mathrm{rad}}{\mathrm{s}}$ ]

$\omega$ = rotor spin speed [ $\frac{\mathrm{rad}}{\mathrm{s}}$ ]

$\omega_i$ = ith natural frequency of the rotor [ $\frac{\mathrm{rad}}{\mathrm{s}}$ ]

# LIST OF TABLES

Table

## LIST OF FIGURES

Figure

# CHAPTER I

# INTRODUCTION

## 1.1 Background and Motivation

Simply put, work is force times distance. And, power is the time rate change of work. Another way of saying this is power is force times speed. Rotating machinery offer a way to achieve high speeds in compact, efficient, able to be harnessed ways. It is because of this that the modern world is built upon rotating machinery, be it a turbine used for power generation, a mill used for manufacturing, or a jet engine used for travel. A failure in a rotating machine can potentially be dangerous to people in the vicinity and costly to repair. The time the machine is stopped for repair can be more costly than the actual machine itself. Rieger et al [1990] reported on the costs associated with rotating machinery failure.

Because of the costs involved, industry seeks to prevent rotating machine failure. There are a variety of malfunctions that will be reviewed in the following section, however the main focus of this work is on shaft transverse cracks.

One way to prevent failure due to developing cracks is to replace the rotor according to some predetermined maintenance schedule. This can be disadvantageous because expensive rotors that are still in working order may be scrapped. Also, if a crack develops in a rotor before the rotor is due to be replaced, it may be left in operation. A method of failure prevention (often complimentary to the previous method) is to regularly examine the rotor for cracks with some non-destructive evaluation (NDE) techniques such as X-ray or fluorescent penetrant inspection. The cracked rotor can then be either repaired or replaced. There is, however, the added economic burden of the inspection process. And, many inspection techniques are never fully reliable because they depend on the inspector's judgment. The NDE methods still require the machine (and possibly production) to be stopped.

There is thus the desire to detect rotor faults while the machine is in operation. This is called condition based maintenance (CBM) where the condition of the rotor is continuously monitored in some way and its health evaluated [Mitchell, 1993]. Vibration monitoring is a widely used and effective in evaluating several rotor malfunctions [Ehrich 1992]. Detection of damage, such as a crack, is essential part of effective failure prevention technology [Sawicki, 2002]. But, it is important that other possible malfunctions be understood because crack detection must be put in context.

## 1.2 State-of-the-Art of Diagnosis of Rotor Systems

Ehrich [1992] offers a good overview of diagnosis of rotating machinery malfunctions. The author will summarize them briefly. Vibration level assessment techniques have existed since the late 1960's. Wave form analysis is a display of one displacement location measure plotted against time. It shows the history of rotor motion in one dimension and may not be useful for complex vibrations. Orbital analysis is the "x vs y" motion of the rotor and is often displayed with a once per revolution timing marker. The shape of an orbit and the location and occurrence of the timing marker can indicate possible malfunctions. Spectrum analysis, conducted with a Fast Fourier Transform (FFT) algorithm will display the different frequencies and relative energy levels of components of a vibration. Many malfunctions will cause a rotor vibration component at multiples (nX) or fractions ($\frac{n}{m} \times X$) of the running speed.

A mass unbalance will, of course, cause a large frequency component at one times the operating speed (1X). Also, the orbit is generally circular or elliptical. Every rotor has some residual unbalance. Bearing misalignment will induce the rotor vibrations to display 2X, 3X, etc. components that are equal or even higher than the 1X. A bowed shaft has an easy to visualize 1X component. Steam loading causes a load sensitive 1X component. Worn bearings lead to a higher than otherwise 1X and ½ X components. Also, the rotor will not be able to be balance correctly.

Ehrich [1992] also gives information on rotor asymmetry, thermal instability, and cracks, as well as malfunctions relating to bearings that can be monitored through CBM. Evans [2002] in another excellent resource offers standards for acceptable machine vibrations.

Many machine monitoring methods incorporate system modeling [Sawicki 2001]. Comparing the model to the state of the rotor system can indicate if the rotor is healthy or faulty. During run up and cost down, the rotor passes through a range of speeds. With this information, and the vibration magnitudes at each speed, a bode plot can be drawn [Bently 1995] and [Muszynska 1995]. Obviously, this is disadvantageous because it still required the machine to be stopped. However in systems that start and stop often anyway, it can be more useful. Online perturbation for gathering similar data is also explored.

One rotor malfunction that has recently received much study, both experimental and through simulation is rubbing. Adams [2001] used a Jeffcott rotor simulation to show the usefulness of bifurcation diagrams and Poincare map in identifying impact-rubbing behavior. Spectra power analysis is also used to interpret the highly nonlinear dynamics. Sawicki et al [2003] experimentally investigated the sub-harmonics and amplitude discontinuities of rotor stator rubbing. Also, Sawicki [1999] analyzed experimentally identify sub harmonics caused by rubbing using FFT and Al-Khatib [1997] was able to show system parameter changes that could not be detected with FFT could be detected using bifurcation diagrams and Poincare maps. Al-Khatib showed the potential of chaos signal processing in this area.

One interesting aspect of rotor rubbing is the thermal consequences and how vibrations are affected. Taylor [1924] studied shaft rubbing above and below the critical speed and after Taylor's results, Newkirk [1926] pointed out that rubbing below the first critical speed brings with it vibrations with amplitude increasing with time. This is due to uneven heating of the shaft and subsequent thermal expansion causing warping. More recent studies in this area include [Dimaroganas 1973], [Dimaroganas 1983], and [Muszynska 1993]. Kellenberger [1980] studied this effect in turbogenerators in relation to seal rings.

An example of an industry greatly concerned with all types of rotating machinery malfunctions and how to detect them online is the jet engine industry. Two recent studies in this area are [Gyekenyesi 2002] and [Baaklini 2002]. The application of health diagnosis through vibration monitoring is examined.

Dimarogonas [1996] conducted a review of the vibration of cracked structures and Doebling et al [1996] conducted an extensive survey of the crack detection field including works using external force perturbation. The survey does not include rotating machinery, but it is useful for further detail on the topic.

The most basic form of crack detection is by observing the vibration for a 2X frequency component. Dimentberg [1961] showed that the total motion of an asymmetric shaft center is the sum of a vector that turns with the angular velocity and a vector that turns with twice the angular velocity. The result is a spiral like orbit that is determined by the relative lengths of the two vectors. The reason for this phenomenon is the shaft switches between a strong axis and weak axis twice per revolution. When the weak axis is resisting gravity the shaft sits lower than when the strong axis does. This oscillation added to the dynamic orbit of the shaft causes the 2X component. A transverse crack makes a shaft have asymmetric stiffness.

Unlike a simple asymmetric shaft, a shaft with a transverse crack may exhibit so called breathing. That is the crack opens and closes with the rotation of the shaft. The crack will be open when it is directed downward because the shaft bends downward with its own weight. The crack will likewise be closed when it is directed upward because the shaft is bowed away from it. This is of course only the case when the weight of the shaft is greater than the dynamic force due to rotation. This is called weight dominance. If dynamic forces are greater than the weight, the crack will either remain closed or open, depending on the crack's phase with relation to high spot. Weight dominance will be the assumption for the analysis in this work.

For a transverse crack in a shaft under weight dominance, Gasch [1976] proposed a hinge like model for the opening and closing of the crack and subsequent time varying stiffness. In his work, the crack opens and closed abruptly, changing from maximum to minimum stiffness instantly and the motion of the rotor was analyzed. A modified crack model was put forth by Mayes [1976] where the crack opens and closes with a cosine function. Simulations using fracture mechanics have shown that the two models' behavior is nearly identical [Jun 1992]. Gasch [1993] conducted a survey of the topic which should be consulted for further detail. Another survey that is a good resource is [Wauer 1990].

All of the above techniques for health monitoring are passive. That is, they do not affect the rotor and only observe its motion. In order to widen the range of situations where online health monitoring is affective, active methods were explored. Active online monitoring is where the rotor is affected in some way and the response in observed. By comparing the response to the expected response, the state of the system can be monitored. Rotating systems present certain difficulties in active monitoring because of their motion. It will be seen that active magnetic bearings (AMB), either as an additional actuator to a conventional bearing system or through a superimposed signal injection to a full AMB system is a useful tool to active condition monitoring to rotating machinery.

Morton [1975] was one of the first who identified dynamic properties of a full operating turbomachine by means of a broadband excitation technique. The rotating shaft was preloaded with a static force via an additional foil bearing. The excitation force was created by a sudden release of the preload due to the use of a breaking link, while the applied forces were measured with strain gauges. The method was used for the identification of rotordynamic coefficients of oil film bearings. Nordmann [1984] and Tonnesen [1988] excited a rotating Jeffcott rotor supported on oil film bearings by a hammer. The impact force and displacement signals were used for identification of the modal parameters of the rotating system. One of the disadvantages of the broadband excitation in general is the distribution of the energy over a certain frequency range, which may cause a poor signal to noise ratio. Iwatsubo *et al.* [1992] used external excitation technique to analyze the response of the cracked shaft. He showed the presence of combination harmonics due to interaction between impact force and rotation of shaft as the crack indicators.

Nordmann [2004] showed experimentally that the transfer function of a centrifugal pump levitated in AMB's could be measured and used to diagnose faults. Bash [2005] used AMB actuator to perform a sine sweep on a test rotor and measure the change in natural frequency due to a transverse crack. Kasarda et al [2005] showed experimentally that AMB could be used to accurately excite natural frequencies of a test rig with a variety of input types such as sine sweep and random noise. Also, the usefulness of these measurements was demonstrated using simulations. Quinn et al [2005] showed experimentally that timed force injections from an AMB can be used to identify the time varying stiffness of a rotor with a transverse crack.

Penny et al [2006] and Mani et al [2006] showed with numerical simulations that the combinational frequencies present in a cracked rotating system can be excited by a harmonic force input from a magnetic bearing (MB). Sawicki et al [2008] confirmed the simulations with experimental results. Also, the sub harmonics in such a system were experimentally found using a sine sweep from AMB actuator [Ishida 2006].

### 1.3 Scope of Work

The aim of this thesis is to investigate a novel structural health monitoring approach for the detection of damage in a form of transverse crack in rotating shafts, which utilizes an active magnetic bearing (AMB) as an actuator for applying multiple types of force inputs on to a rotating structure for analysis of resulting outputs. To that end, the scope of this work includes discussing and demonstrating the approach. Discussion of the approach will include the modeling of a simple Jeffcott rotor, evaluation how a transverse crack and force injection will affect the model, and making predictions for the rotor's motion using numerical integration. Demonstrating the approach will enforce the prediction with experimental results. The experimental test rig will be described and the dynamics will be identified using FEA and a sine sweep analysis. Then actual position data will be taken for a "healthy" i.e., undamaged shaft running on ball bearings and compared to that for a damaged shaft under the same conditions. To ad breadth to the demonstration the same comparison will be made for a rotor levitated on active magnetic bearings.

In Chapter 2 the modeling of the Jeffcott rotor will be provided and used to make prediction for the difference in motion of a cracked and un-cracked Jeffcott rotor when it is harmonically excited. Chapter 3 will describe the test rig used to perform the experiment in detail, including rotor configuration, data acquisition, magnetic bearing modeling, and force estimation. The results of the experiment will be presented and discussed in Chapter 4. Chapter 4 will include a section for the rotor on traditional ball bearing supports and a section for the rotor levitated magnetically. Conclusions and recommendations will be in Chapter 5.

# CHAPTER II

# THE CRACKED JEFFCOTT ROTOR

## 2.1 Introduction

The crack detection approach investigated in this work can be fully demonstrated by experiment alone. However, to gain a deeper understanding of the method and when it is applicable, equations of motion for a rotating, externally excited rotor will be derived, for the healthy case and cracked case, and the solutions will be found numerically. A Jeffcott rotor model will be used in the modeling for simplicity. The solution will serve as a rough prediction for the experimental results in terms of the general form but not in terms of actual values because the Jeffcott rotor is an idealized model which does not resemble the actual test rig. Actual physical parameter values of the test rig will be used to generate values for the Jeffcott rotor model with the intention of making the solution on the similar order as the actual experimental results.

## 2.2 Model of Jeffcott Rotor

A Jeffcott rotor, sometimes called a de Laval rotor, has one disk and two support bearings. The bearings are at the ends of the rotor and assumed to be rigid. Because they are rigid, the bearings have infinite stiffness, and will not deflect as the shaft rotates. The bearings are also considered to be at a point location and as such, will allow free rotation around them. The shaft is assumed to have no mass but can deform and has stiffness. The disk at the bearing midspan is treated as a point mass or a lumped mass. It has some mass at a specific location and can translate and rotate. The disk is also assumed to be rigid and will not deform.

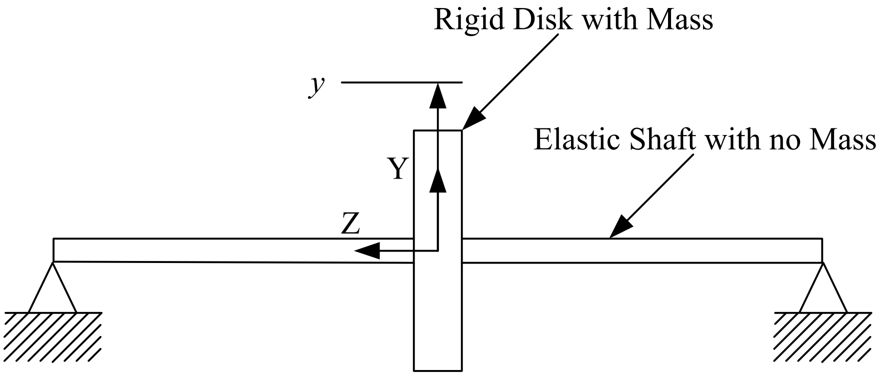

**Figure 2.1 Jeffcott rotor.**

The equation of motion for lateral movement of the disk is derived from Newton's Second Law.

$$m\mathbf{a} = \mathbf{F} \tag{2.1}$$

$$m\begin{Bmatrix} \ddot{y} \\ \ddot{x} \end{Bmatrix} = \begin{Bmatrix} F_y \\ F_x \end{Bmatrix} \tag{2.2}$$

This of course uses Newton's fly speck notation to denote time derivatives. The lateral force on the disk comes from damping, stiffness of the shaft, centrifugal force due to unbalance and weight of the disk.

$$m\ddot{y} = me\omega^2 \sin(\omega t) - mg - c_y \dot{y} - k_y y \tag{2.3}$$

$$m\ddot{y} + c_y \dot{y} + k_y y = me\omega^2 \sin(\omega t) - mg \tag{2.4}$$

Putting this in matrix form with the vector **q** being the x-y position vector yields:

$$\mathbf{M}\ddot{\mathbf{q}} + \mathbf{C}\dot{\mathbf{q}} + \mathbf{K}\mathbf{q} = me\omega^2 \begin{Bmatrix} \sin(\omega t) \\ \cos(\omega t) \end{Bmatrix} - mg \begin{Bmatrix} 1 \\ 0 \end{Bmatrix} \tag{2.5}$$

This is of a well known form and has an exact analytical solution. Taking the possible crack into account complicates the model.

## 2.3 Model of Cracked Jeffcott Rotor

### 2.3.1 Crack Models

A crack will have the effect of decreasing the stiffness of the shaft. But, this is only true when the crack is open. Under weight dominance (static deflection being greater than dynamic deflection) a transverse crack will open and close repeatedly during rotation. And, the reduction in stiffness will be different in the axis perpendicular to the crack than in the axis parallel to the crack. These axes are of course rotating because the shaft is rotating. As a result, the shaft will have a time varying stiffness.

The rotating coordinates that describe the location of the crack are the $\zeta$ axis, perpendicular to the edge of the crack, and the $\eta$ axis, parallel to the edge of the crack. Figure 2.2 below shows the rotating coordinates in relation to a cross section of the shaft at the location of a transverse crack when the shaft is rotating.

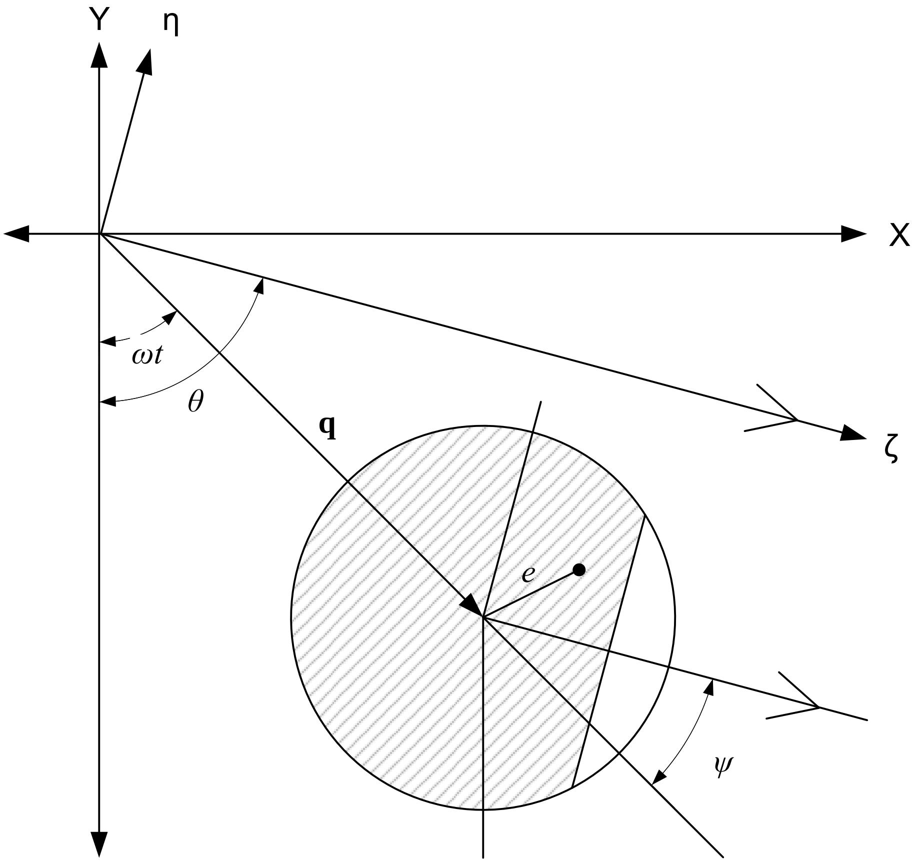

**Figure 2.2 Shaft cross section at crack plane near disk showing rotating coordinate system.**

If the stiffness of the undamaged shaft in rotating coordinates is given by:

$$\tilde{\mathbf{K}} = \begin{bmatrix} k_\zeta & 0 \\ 0 & k_\eta \end{bmatrix} \tag{2.6}$$

Of course, for the undamaged round shaft, the stiffness in the $\eta$ and $\zeta$ directions are the same and can be denotes as simply $k$. Then the stiffness of the cracked shaft will be:

$$\tilde{\mathbf{K}}_{\mathbf{cr}}(\theta) = \begin{bmatrix} k & 0 \\ 0 & k \end{bmatrix} - f(\theta) \begin{bmatrix} \Delta k_\zeta & 0 \\ 0 & \Delta k_\eta \end{bmatrix} \tag{2.7}$$

which is the stiffness of the healthy shaft reduced by the change in stiffness in the strong ($\eta$) and weak ($\zeta$) axes due to the crack. The function $f\left(\theta\right)$ is a steering function that dictates if the crack is open or closes and therefore whether or not the stiffness is reduced. There are two main steering functions proposed for the description of a transverse crack opening and closing. One proposed by Gasch [1976] is a step function where the crack is either open or closed. The other proposed by Mayes and Davies [1976] is a cosine function, where the crack opens and closes smoothly, as shown in Figure 2.3 below. Jun et al. [1992] conducted a detailed simulation of the opening and closing of a transverse shaft crack using fracture mechanics and found the approximate stiffness reduction is in between these two steering function and that they yield almost identical results for the lateral displacement of the shaft over time during rotation.

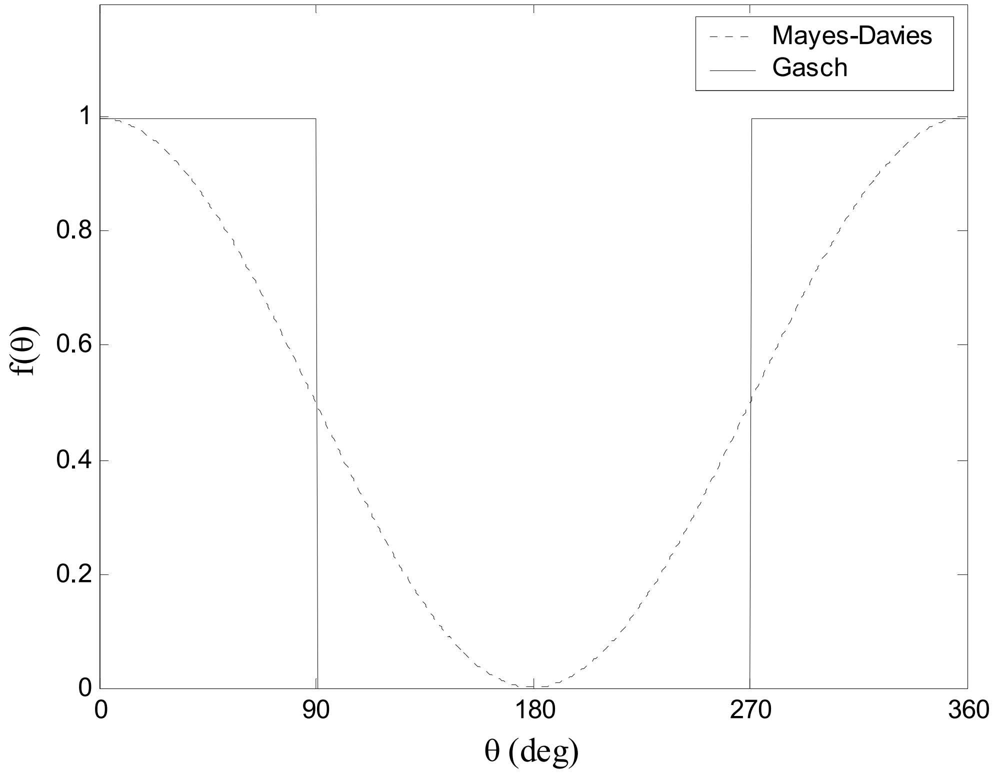

**Figure 2.3 Gasch and Mayes-Davies transverse crack stiffness reduction steering functions.**

Figure 2.4 below shows a cross section of a shaft at the transverse crack for various rotation angles. It illustrates approximate behavior of the crack as it breaths with rotation. The axes are consistent with those in Figure 2.4 and the angles of rotation are consistent with those in Figure 2.3. Keep in mind that the assumption is made that the dynamic deflection is less than the static deflection such that the crack is pressed closed when it is on the top side of the shaft and is pulled open when it is on the bottom.

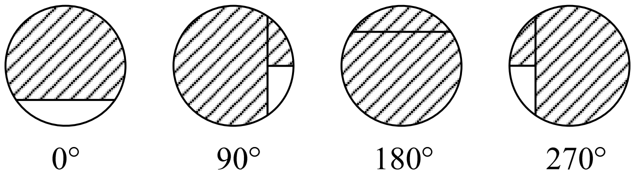

**Figure 2.4 Cross section of shaft at transverse crack for various rotation angles.**

Which ever steering function, $f(\theta)$, is used, it will be a function of rotation angle, $\theta$, therefore, the stiffness will be a function of $\theta$. However, the angle is related to time by the constant speed of rotation, $\omega$ and the angle $\psi$.

$$\theta = \omega t + \psi \tag{2.8}$$

The angle $\psi$ is the angle between the whirl vector and the crack direction and is a function of the angle between the crack direction and unbalance direction and the ratio of spin speed to critical speed. As $\omega$ is constant, $\psi$ is also constant. The stiffness can therefore be expressed as a function of time.

$$\tilde{\mathbf{K}}_{\mathbf{cr}}(t) = \begin{bmatrix} k_\zeta & 0 \\ 0 & k_\eta \end{bmatrix} - f(t)\begin{bmatrix} \Delta k_\zeta & 0 \\ 0 & \Delta k_\eta \end{bmatrix} \tag{2.9}$$

This stiffness matrix must then be transformed into stationary coordinates to be put into the equation of motion. This is done using **T**, the transformation matrix.

$$\mathbf{T} = \begin{bmatrix} \cos(\omega t) & \sin(\omega t) \\ -\sin(\omega t) & \cos(\omega t) \end{bmatrix} \tag{2.10}$$

$$\mathbf{K_{cr}}(t) = \mathbf{T}^{\mathrm{T}}\tilde{\mathbf{K}}_{\mathbf{cr}}(t)\mathbf{T} \tag{2.11}$$

$$\mathbf{K_{cr}}(t) = \begin{bmatrix} k & 0 \\ 0 & k \end{bmatrix} - \mathbf{T}^{\mathrm{T}}\left( f(t)\begin{bmatrix} \Delta k_{\zeta} & 0 \\ 0 & \Delta k_{\eta} \end{bmatrix}\right)\mathbf{T} \tag{2.12}$$

### 2.3.2 Equation of Motion of a Cracked Jeffcott Rotor

Substituting the stiffness matrix for the cracked Jeffcott rotor in stationary coordinates into the equation of motion for the healthy Jeffcott rotor gives the equation of motion for the cracked Jeffcott rotor. Note that $\mathbf{K_{cr}}$ is a function of time.

$$\mathbf{M\ddot{q}} + \mathbf{C\dot{q}} + \mathbf{K_{cr}}(t)\mathbf{q} = me\omega^2 \begin{Bmatrix} \sin(\omega t) \\ \cos(\omega t) \end{Bmatrix} - mg\begin{Bmatrix} 1 \\ 0 \end{Bmatrix} \tag{2.13}$$

The position vector $\mathbf{q}$ can be separated into its static and dynamic components, $\mathbf{q_{st}}$ and $\mathbf{q_{dy}}$ respectively.

$$\mathbf{q} = \mathbf{q_{st}} + \mathbf{q_{dy}} \tag{2.14}$$

Substituting equation (2.14) into equation (2.13) gives:

$$\mathbf{M\ddot{q}_{dy}} + \mathbf{C\dot{q}_{dy}} + \mathbf{K_{cr}}(t)\left(\mathbf{q_{st}} + \mathbf{q_{dy}}\right) = me\omega^2 \begin{Bmatrix} \sin(\omega t) \\ \cos(\omega t) \end{Bmatrix} - mg\begin{Bmatrix} 1 \\ 0 \end{Bmatrix} \tag{2.15}$$

As the shaft rotates and the crack opens and closes, the stiffness changes and so the static displacement will change. This change is neglected because the change in stiffness due to a crack is usually small and the resulting change in static equilibrium is small. With this simplification, the static displacement is constant and effectively equal to the weight divided by the stiffness of the healthy shaft. The static displacement multiplied by the stiffness cancels out with weight yielding equation (2.16).

$$\mathbf{M}\ddot{\mathbf{q}}_{\mathbf{dy}} + \mathbf{C}\dot{\mathbf{q}}_{\mathbf{dy}} + \mathbf{K}_{\mathbf{cr}}(t)\mathbf{q}_{\mathbf{dy}} = me\omega^2 \begin{Bmatrix} \sin(\omega t) \\ \cos(\omega t) \end{Bmatrix} \tag{2.16}$$

Equation (2.5) is the equation of motion for a Jeffcott rotor. Equation (2.5) is modified for a transverse crack and the weight dominance assumption to get equation (2.16). For the active crack detection method, the equation must again be modified to include an external force.

$$\mathbf{M}\ddot{\mathbf{q}}_{\mathbf{dy}} + \mathbf{C}\dot{\mathbf{q}}_{\mathbf{dy}} + \mathbf{K}_{\mathbf{cr}}(t)\mathbf{q}_{\mathbf{dy}} = me\omega^2 \begin{Bmatrix} \sin(\omega t) \\ \cos(\omega t) \end{Bmatrix} + \begin{Bmatrix} F_E \sin(\Omega t) \\ 0 \end{Bmatrix} \tag{2.17}$$

Here, $F_E$ is the magnitude of external excitation and $\Omega$ is the frequency of excitation which will be discussed in the next section.

## 2.4 Combinational Frequency Excitation

There exists in such a system, frequencies that are the combination of the running speed, natural frequencies, and external injection frequency at which resonance occurs. Mani et al. (2005) and Quinn et al. (2005) used multiple scales analysis to determine the conditions required for these combinational frequencies. This is given by the following equation.

$$\Omega = |n\omega - \omega_i|, \quad \text{for} \quad n = \pm 1, \pm 2, \pm 3 \ldots \tag{2.18}$$

where $\Omega$ is the combinational frequency, $\omega$ is the rotor spin speed and $\omega_i$ is the ith natural frequency. Note that because of the particular assumptions made for the Jeffcott rotor, the system only has one natural frequency and that it will be tuned to match the first natural frequency of the test rig. By selecting an $n$ value, solving for $\Omega$ and injecting that frequency into the system, the combinational frequencies corresponding to all other *n* values will be induced and can be observed if damage such as a crack is present. In the Jeffcott rotor simulation, an external force excitation is applied to the disk in the direction of gravity. It is this force, at such a frequency, that provides external excitation and excites resonances at the combinational frequencies. Because the Jeffcott rotor model has the same natural frequency (36 Hz) and running speed (27 Hz) as the experimental test rig on ball bearings, the combinational frequency values are the same. Some of these values are shown in Table I below.

**Table I Combinational frequencies corresponding to the rotor test rig supported on ball bearings.**

| *n* | Combined Frequency (Hz) |
|---|---|
| -1 | 63 |
| 0 | 36 |
| 1 | 9 |
| 2 | 18 |
| 3 | 45 |
| 4 | 72 |
| 5 | 99 |

## 2.5 Method of Solution and Numerical Simulation Results

A numerical solution to the above equation of motion is found using the Runga-Kutta method for numerical integration via the ode45 function in MatLab. The set values for the simulation are 3.388 kg and 173,345 N/m for mass of the disk and stiffness of shaft respectively. This gives a natural frequency of 36 Hz. The reduction of stiffness due to a 25% diameter crack $\Delta k_\zeta$ and $\Delta k_\eta$ are taken to be $0.25k$ and $0.038462k$ respectively. The reduction of stiffness due to a 40% diameter crack $\Delta k_\zeta$ and $\Delta k_\eta$ are taken to be $0.4k$ and

0.0678$k$ respectively. Here, $\Delta k_\zeta$ is assumed and $\Delta k_\eta$ is found using the axis stiffness reduction ratio interpolated from Gasch (1993). The rotation is set at 27 Hz. Damping is taken as 5 $\frac{\text{N-s}}{\text{m}}$ in both $x$ and $y$ directions with no cross coupling. The external excitation amplitude was set at 10 N. Remember that the values are chosen to be similar to the actual experimental rig but the rig is not a true Jeffcott rotor so the simulation only makes a prediction as to the approximate form of the experimental results.

After the position over time is solved for, the Fast Fourier Transform (FFT) is performed. The time sampling was selected so as to have an integer number of vibrations and a number of samples equal to a power of two in order to minimize leakage. The first few seconds are discarded to minimize transient effect however a small peak can still be seen at the natural frequency.

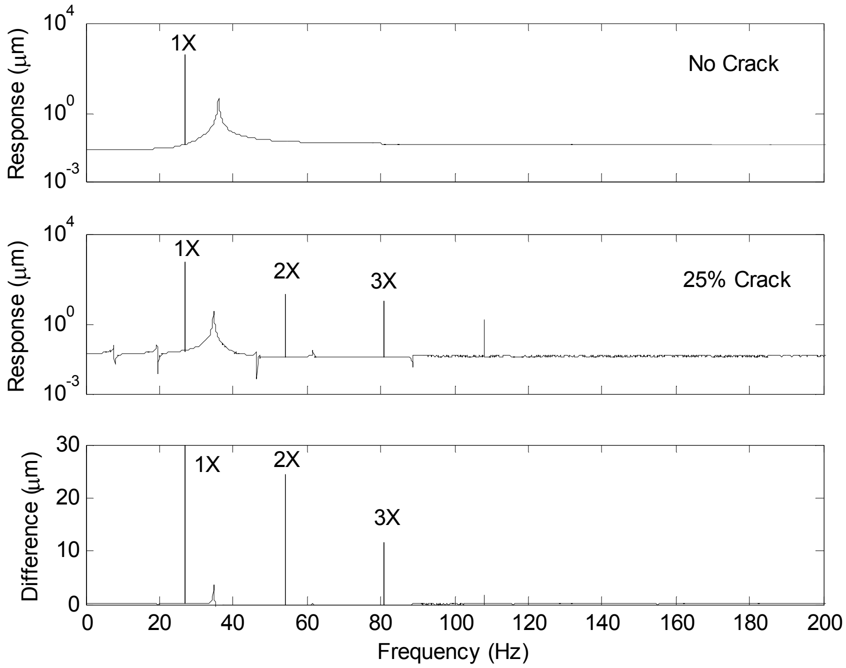

**Figure 2.5 Simulated Jeffcott rotor frequency spectrum of healthy shaft and 25% cracked shaft rotating at 27 Hz with no force injection.**

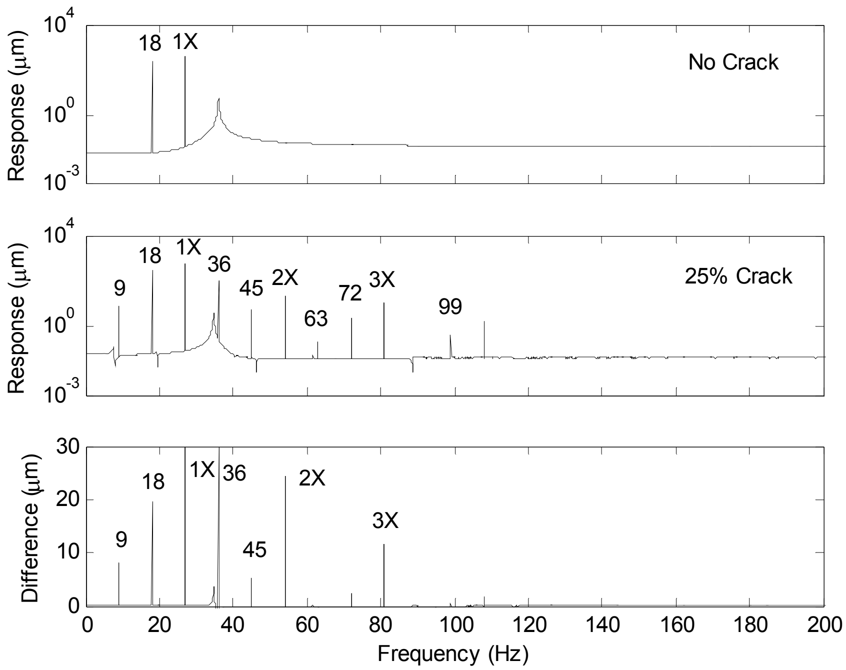

**Figure 2.6 Simulated Jeffcott rotor frequency spectrum of healthy shaft and 25% cracked shaft rotating at 27 Hz with 10 N force injection at 18 Hz.**

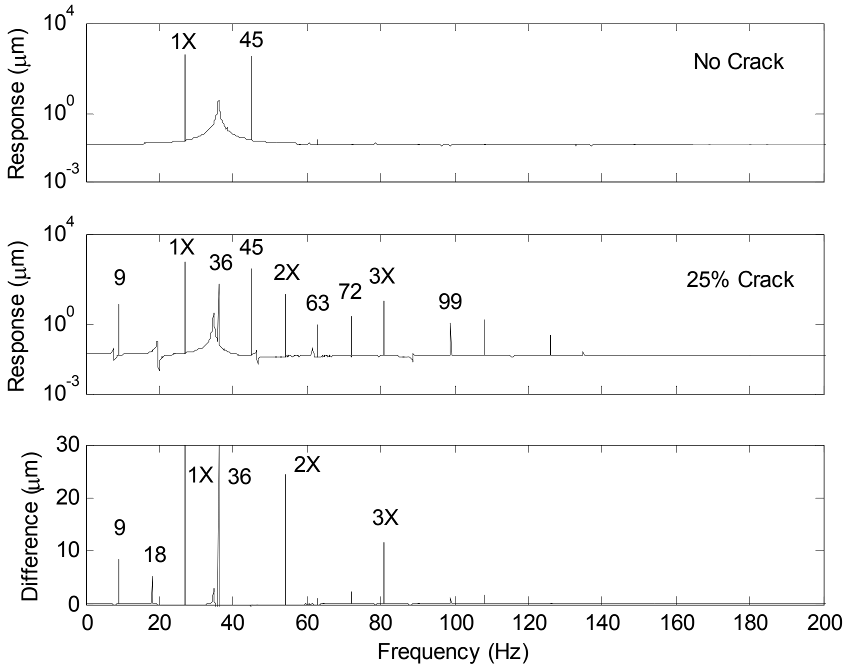

**Figure 2.7 Simulated Jeffcott rotor frequency spectrum of healthy shaft and 25% cracked shaft rotating at 27 Hz with 10 N force injection at 45 Hz.**

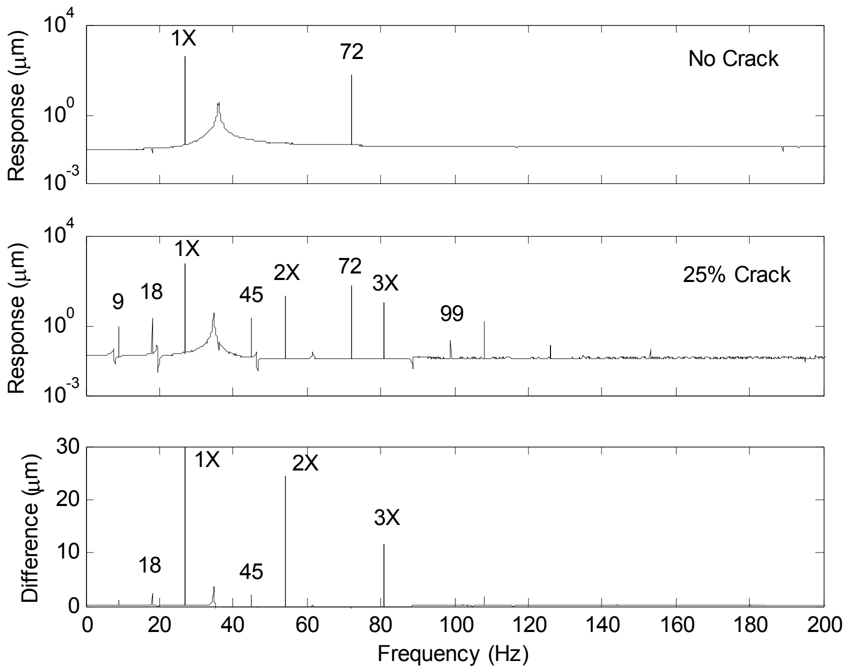

**Figure 2.8 Simulated Jeffcott rotor frequency spectrum of healthy shaft and 25% cracked shaft rotating at 27 Hz with 10 N force injection at 72 Hz.**

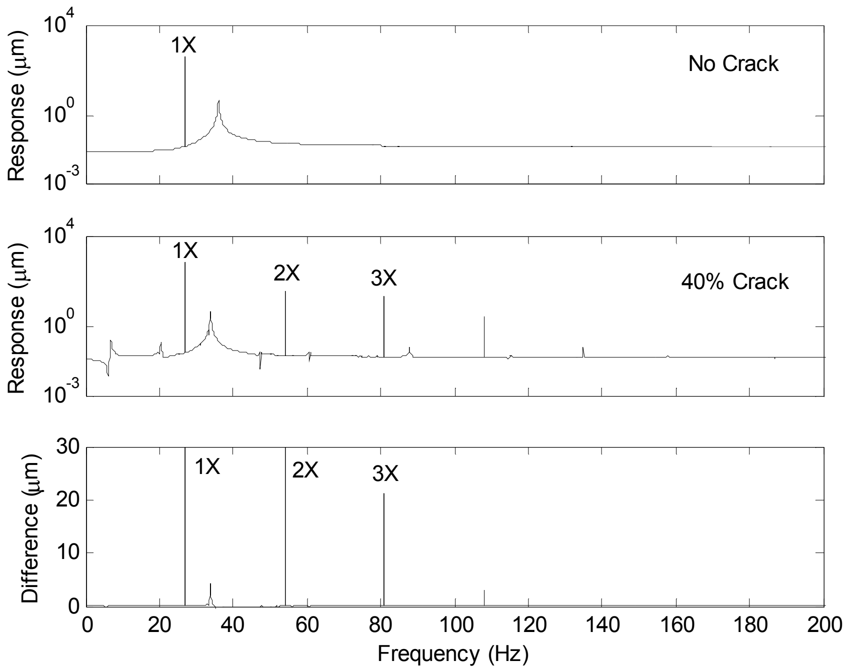

**Figure 2.9 Simulated Jeffcott rotor frequency spectrum of healthy shaft and 40% cracked shaft rotating at 27 Hz with no force injection.**

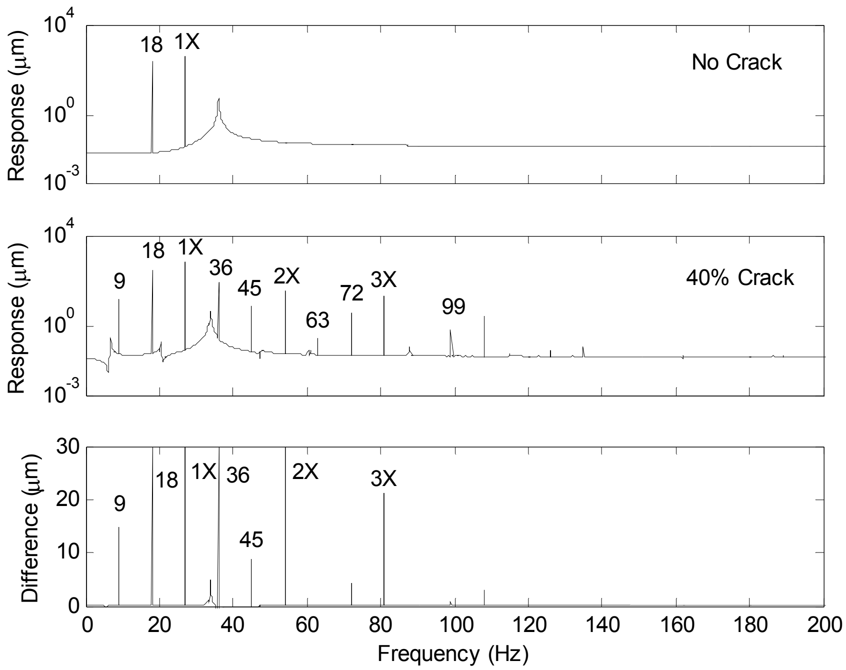

**Figure 2.10 Simulated Jeffcott rotor frequency spectrum of healthy shaft and 40% cracked shaft rotating at 27 Hz with 10 N force injection at 18 Hz.**

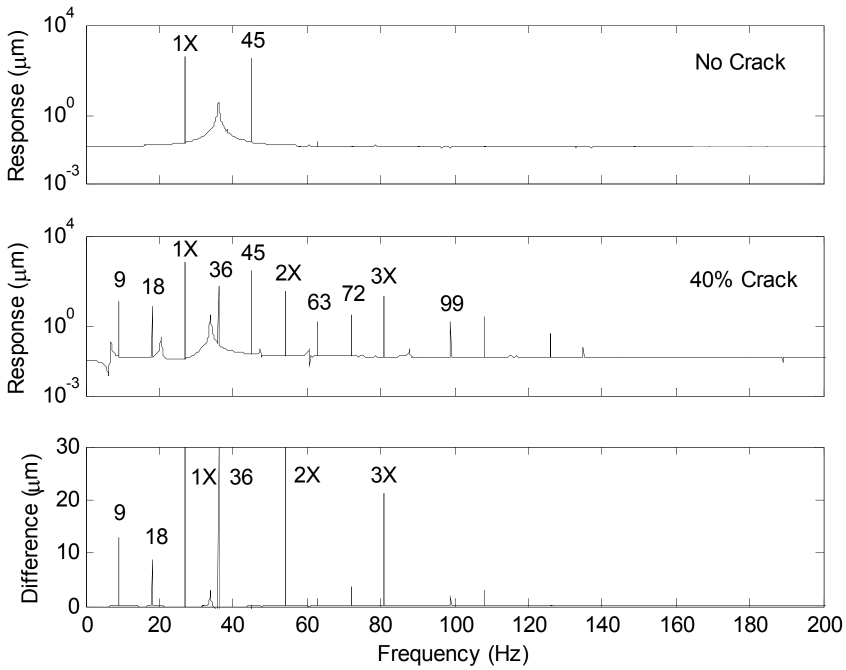

**Figure 2.11 Simulated Jeffcott rotor frequency spectrum of healthy shaft and 40% cracked shaft rotating at 27 Hz with 10 N force injection at 45 Hz.**

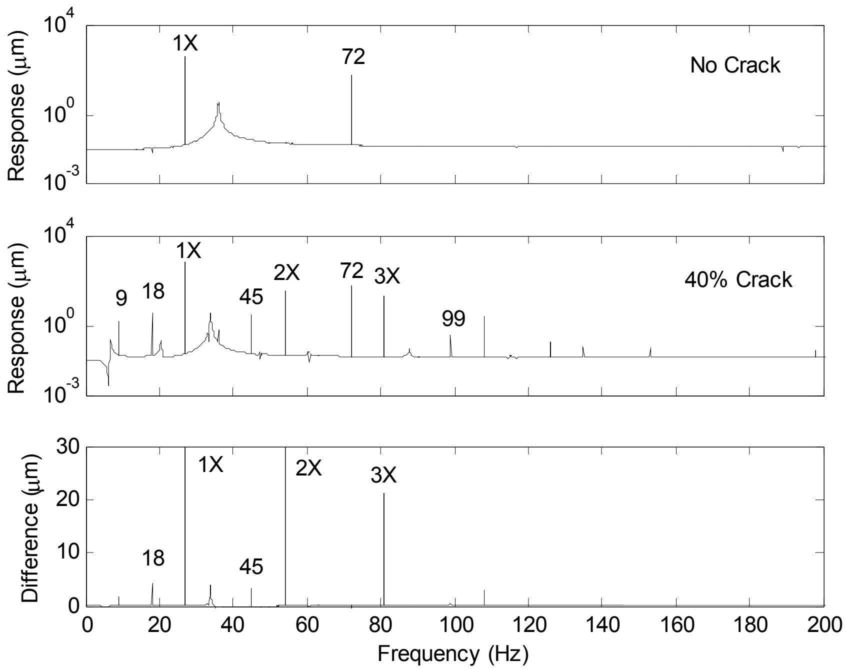

**Figure 2.12 Simulated Jeffcott rotor frequency spectrum of healthy shaft and 40% cracked shaft rotating at 27 Hz with 10 N force injection at 72 Hz.**

# CHAPTER III

# THE CRACK DETECTION TEST RIG

## 3.1 Overview of the Test Rig

For the experimentation, a test rig manufactured by SKF Magnetic Bearings (currently S2M) was used and is shown in Figure 3.1(a). The test rotor consists of a carbon steel disk and three specialized magnetic bearing target rotors mounted on a 26 inch long, 0.625 inch diameter 416 stainless steel shaft driven by a 48 volt D.C. brush-type motor via a flexible coupling. The nominal masses and moment of inertia for components of the rotor are listed in Table II. The outline of major dimensions of the rotor assembly configured with magnetic bearing rotors, exciter rotor, shaft and the disk is presented in Figure 3.1(b). Note that the “large disk” is used for the trials on ball bearing supports and the “small disk” is used, in the same location, for trials in magnetic bearing supports.

The motor is controlled with a PI controller. The rotor runs on bearings, either conventional deep-groove Conrad type ball bearings or active magnetic bearings, depending on the type of experimental trial. Part of the magnetic bearing housings is a conventional ball bearing with an oversized inside diameter to fit the rotor shaft but smaller than the inside diameter of the magnetic bearing stators. These are called touchdown (also auxiliary, backup, or catcher) bearings and serve to protect the magnetic bearing stators in case levitation failure occurs. For the experimental trials involving conventional ball bearing supports, the touchdown bearings are replaced with ball bearings that actually support the rotor. In that case, AMB coils are deactivated but the sensors are still used to gather position data. More details on the capabilities of the magnetic bearings are in following sections.

The controllers for the magnetic bearings are the SKF model MB340g4-ERX, 5 axis, fully digital controllers. One unit controls the two AMB's used for levitation and the motor. A second unit controls the exciter magnetic bearing. The exciter has no active control system and the only force on the rotor comes from the injected excitation signal. The controllers are programmed using a PC equipped with the software package, MBScope2000 version 4.07. These controllers are useful in research because of the ability to collect position and current data, and inject perturbations through a BNC interface called the MBResearch Board. The data collection and signal injection is accomplished using dSPACE Inc.'s DS1103 PPC Controller Board. Because the dSPACE system is a digital control rapid prototyper, it is flexible such that it can collect data from many channels and inject any user specified signal, in this case, a sine wave in the exciter at a particular frequency. The dSPACE programming is compiled from a Simulink model and the collected data is saved in MatLab format, also making it ideal for research. More details on the magnetic bearings are provided in Appendix A.

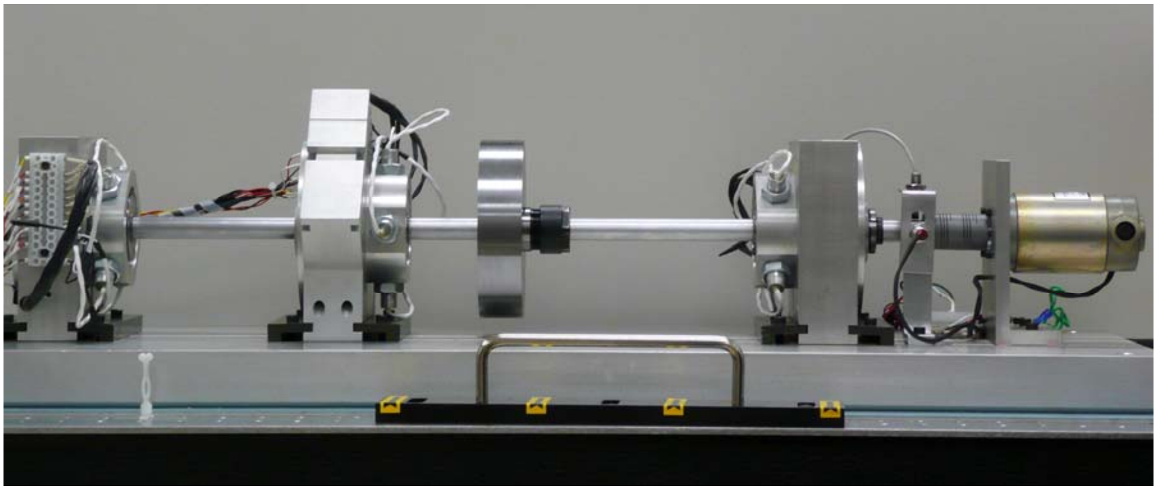

Figure 3.1(a)  Crack detection test rig mounted on ball bearings with large disk.

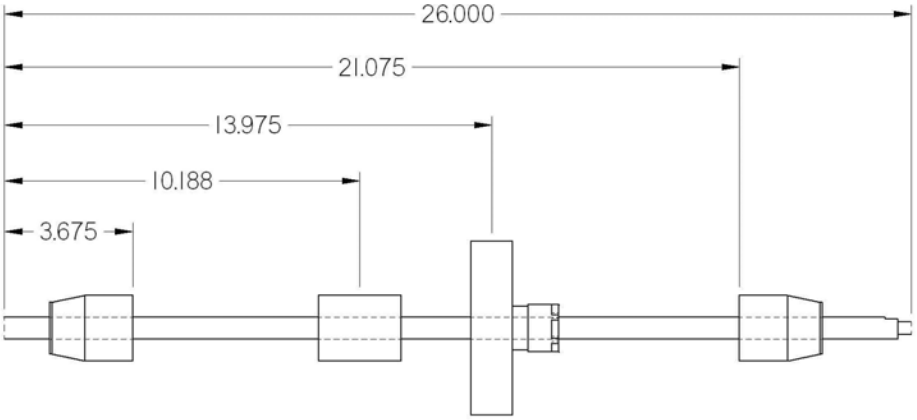

Figure 3.1(b)  Major dimensions in inches of the rotor assembly shown with conical magnetic bearing rotors, exciter's rotor and unbalance disk.

Table II  Nominal masses and moments of inertia for the rotor components.

| Component | Mass (kg) | Polar Moment of Inertia (kg-m$^2$) | Transverse Moment of Inertia (kg-m$^2$) |
|---|---|---|---|
| Shaft | 1.02113 | $3.200\times10^{-5}$ | $3.642\times10^{-2}$ |
| Large Disk | 3.17799 | $6.171\times10^{-3}$ | $3.513\times10^{-3}$ |
| Small Disk | 1.33810 | $2.470\times10^{-3}$ | $1.267\times10^{-3}$ |
| Radial MB rotor | 0.75205 | $2.394\times10^{-4}$ | $3.526\times10^{-4}$ |
| Conical MB rotor | 0.67721 | $2.037\times10^{-4}$ | $2.903\times10^{-4}$ |

## 3.2 Overview of Active Magnetic Bearings: Modeling and Control

### 3.2.1 One-Axis Control

Active magnetic bearings use an electromagnet to suspend a ferromagnetic mass. (The mass is usually a target rotor affixed to a shaft. Thus the suspension of the rotor allows the entire rotor to rotate with no contact frictions. In this way, the system acts as a bearing. Because such a magnet can only create attractive forces on the mass and that force is inversely proportional to the square of the distance to the target mass, the system is inherently unstable. Permanent magnets, which can produce repulsive forces on each other, have been shown by Earnshow in 1842 to be unable to create stable levitation as well (Earnshow [1842]). An active control system must be used to achieve stable levitation. Figure 3.2 shows the basic negative feedback control loop applied to one axis of a magnetically levitated rotor. This is a single input, single output, (SISO) system. As shown in this figure, each displacement transducer detects the mass position at the coil location and its signal is fed back to the controller. Deviation from the reference center is delivered to the controller. This controller can, for example, implement a proportional, integral and differential actions (PID) control algorithm. The controller drives the power amplifiers to supply the coil current. If the mass moves downward, the upper electromagnetic coil is activated to lift the mass upward by the magnetic force. Since, in this manner, the magnetic force acts upon the mass so as to maintain the mass at the reference (neutral) position inside the bearing, the AMB accomplishes both levitation and vibration control.

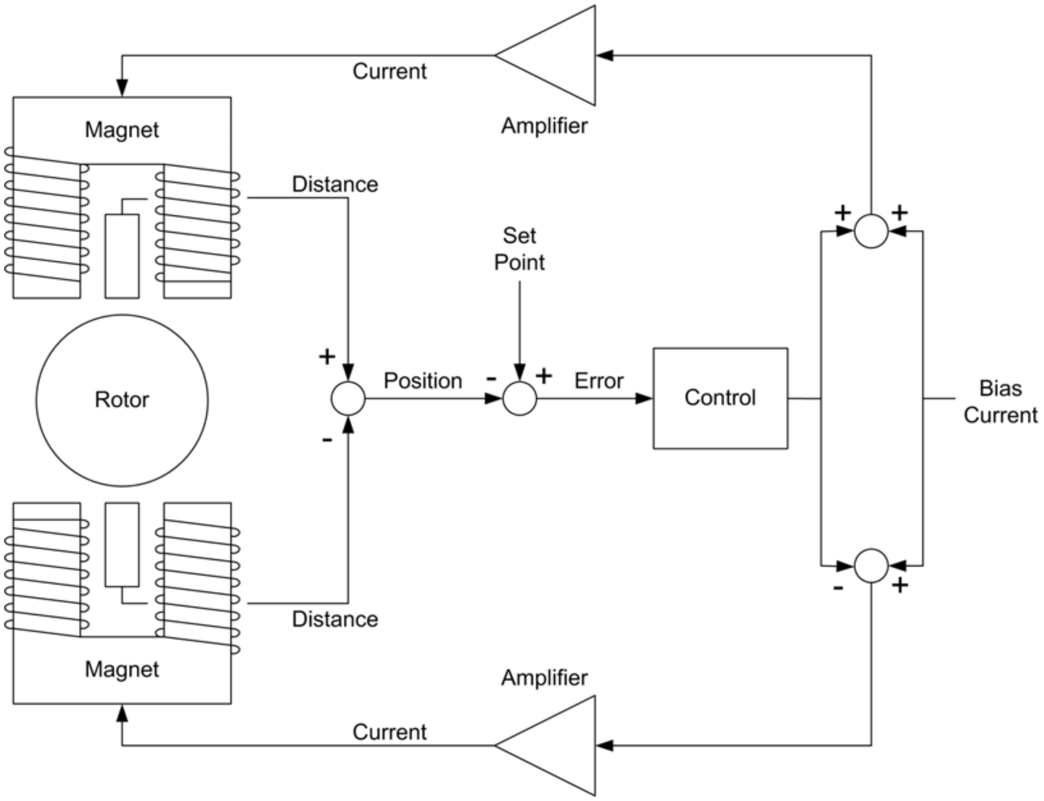

Figure 3.2 Control scheme for one-axis control.

This is one axis control (only in one direction), because the magnet can only pull. To create force in the opposite direction, an identical magnet is put on the other side of the rotor. In order to accommodate this, differential type of control is used. The position probes are wired in series such that when the rotor is equidistant between them, the voltage generated is zero. The sensors are calibrated in that configuration and the geometric center of the rotor is tracked. An equal bias current is sent to each opposing magnetic coil and the control current from the PID is added to one current and subtracted from the other. See Figure 3.2 above. Of course, a negative control current may result from the controller but it can not over take the bias current for proper operation. The resulting force from the opposing magnets can now be positive or negative and can be controlled.

Although the force on the rotor from the magnetic bearing is highly nonlinear, the force can be linearized at the set point for control purposes. The structure of the actuator is assumed to have position stiffness, $k_q$, and current stiffness, $k_i$. These stiffnesses are derived in section 3.4 of this chapter, which discusses the force resulting from a magnetic bearing. In Figure 3.3, below, is a generalized feedback control loop, for one axis, using these approximations.

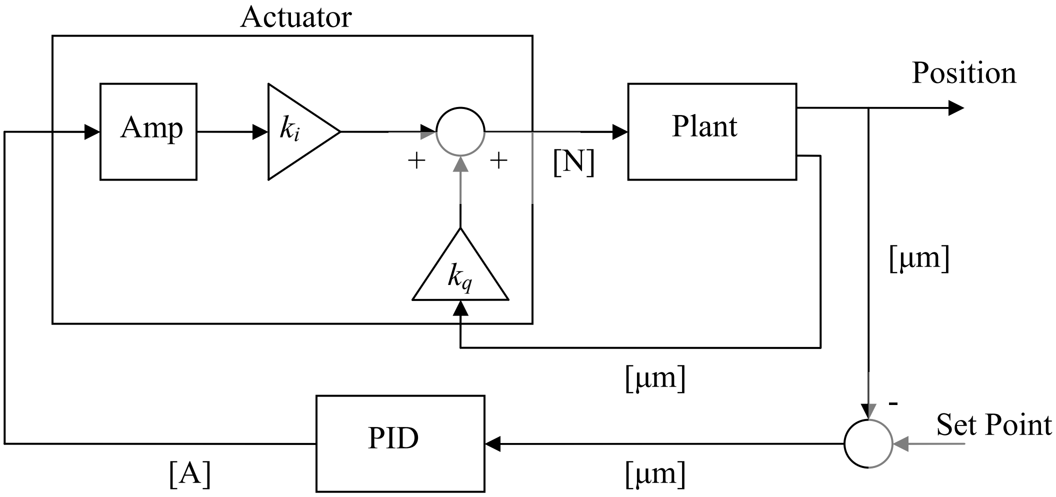

**Figure 3.3 Feedback control loop for one axis active magnetic bearing system with linearized force actuator model.**

### 3.2.2 PID Control of an AMB Rotor System

The entire rotor system, however, has multiple inputs and outputs. Each AMB axis has its own independent controller. The experimental test rig has five axes for AMB levitation. The two axes used for excitation are controlled using a separate MB340 unit.

Figure 3.4 below shows additional insights into the actual test rig control system beyond the basic negative feedback control loop.

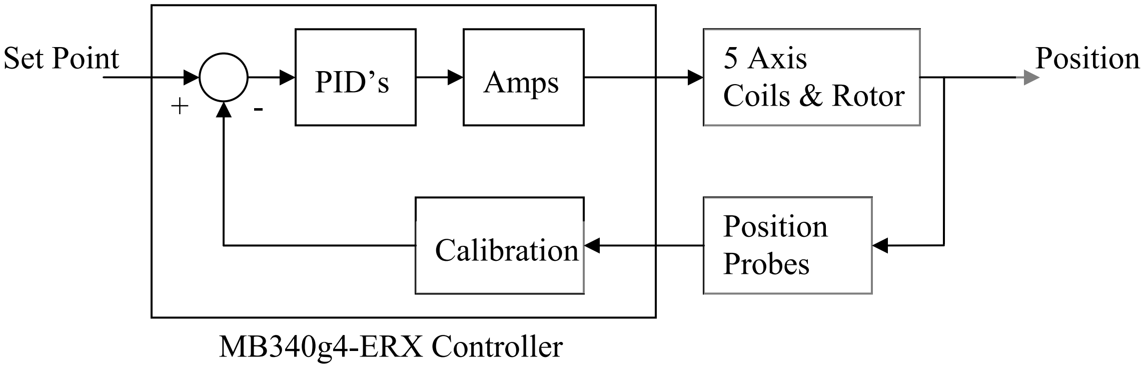

**Figure 3.4 Feedback control loop for 5 axis PID AMB system showing MB340g4-ERX controller.**

In the test rig used for the experiment, the MBScope software is used to program the set point in the MB340-ERX controller which receives voltage signal from the position probes and uses a digital PID algorithm and an amplifier to send current to the magnetic bearing coils on four axes. Note that the MB340g4-Erx is equipped with 10 PWM power amplifiers capable of supplying 3 Amps continuously at 48 Volts unregulated and have a switching frequency of 20 kHz. Also note that the position sensors are variable reluctance sensors. The sensors are not collocated with the magnetic actuators. Because of space restrictions inside the magnetic bearings, the sensors are approximately one inch away from the center of the magnetic poles.

The experimental rig involves conical magnetic bearings. That is, the magnetic target rotors affixed to the shaft are angled by 20° to have a cone shape. Because of this, the force from the magnetic coil has lateral and axial components. This axial force is used in place of a thrust magnetic bearing that independently controls axial displacement in a normal radial (not axial) magnetic bearing. In this way, five independent control loops use four magnetic bearing coil pairs to control position in five axes. For more background on magnetic bearings, see Schweitzer [1994] and Maslen [2000].

The PID controller has been developed for levitating the rotor over the wide range of speeds. The exemplary controller parameters used for experiment are shown in Table III. The transfer function of the developed controller is shown in Fig 3.5.

**Table III Controller parameters**

| Controller Parameter | Value |
|---|---|
| Proportional Gain | 70 A/μm |
| Integral Gain | 100 A/μm-s |
| Derivative Gain | 0.1 A-s/μm |
| Total Gain | 0.00006 |
| Notch Filter Frequency | 300 Hz |
| Notch Damping | 0.3 |
| Low Pass Filter Cut-off Frequency | 1200 Hz |
| Low Pass Damping | 0.707 |

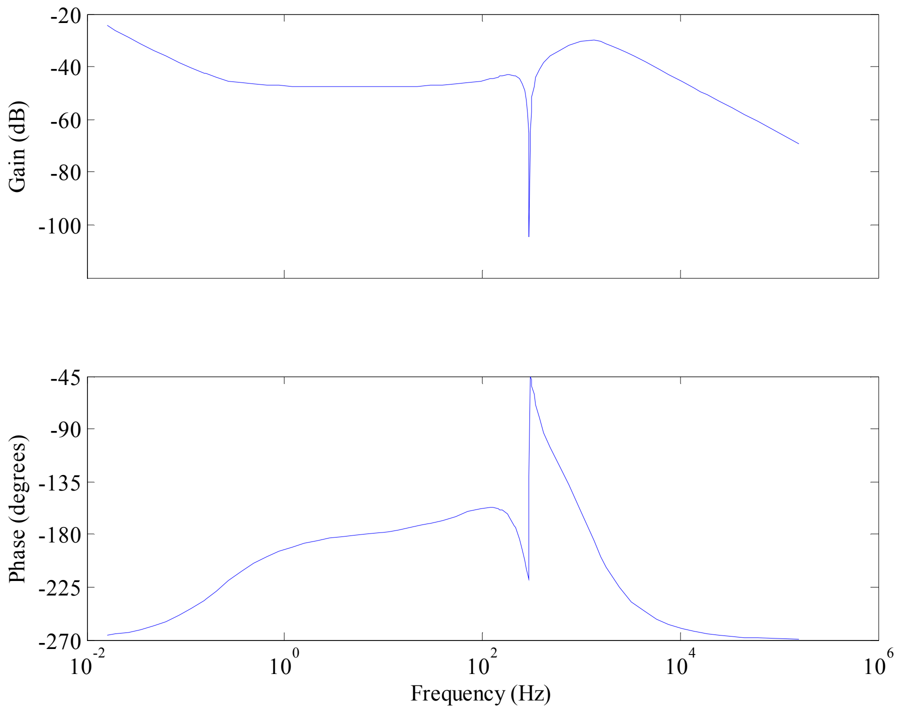

**Figure 3.5 Bode plot of the PID controller used for magnetic bearing active control.**

### 3.3 Rotordynamic Modeling

Finite element approach was applied in modeling of rotor-bearing system. The rotor was discretized into finite elements using Timoshenko beam elements. The finite element modeling program, XLRotor version 3.52 by Rotating Machinery Analysis Inc., was used. The rotordynamic analysis involves generation of the Campbell Diagram and calculation of critical speeds and mode shapes for the rotor on ball bearings and active magnetic bearings. Also included is the prediction of static deflection of the rotor and the critical speed map. For detailed geometry of the rotors, see XLRotor input files in Appendix B.

#### 3.3.1 Conventional Bearing Supports

The FE model with 32 stations, for the configuration with large disk and ball bearings support, is shown in Fig. 3.6. The Campbell diagram for the rotor supported on ball bearings is presented in Fig. 3.7, and indicates number of rotor natural frequencies (critical speeds) and their change as function of speed. The summary of critical speeds and corresponding mode shapes is listed in Table 3.8. The static deflection of the rotor supported on ball bearings is shown in Figs. 3.9. The influence of stiffness of supporting bearings on rotor critical speeds is illustrated by the critical speed map shown in Fig. 3.10.

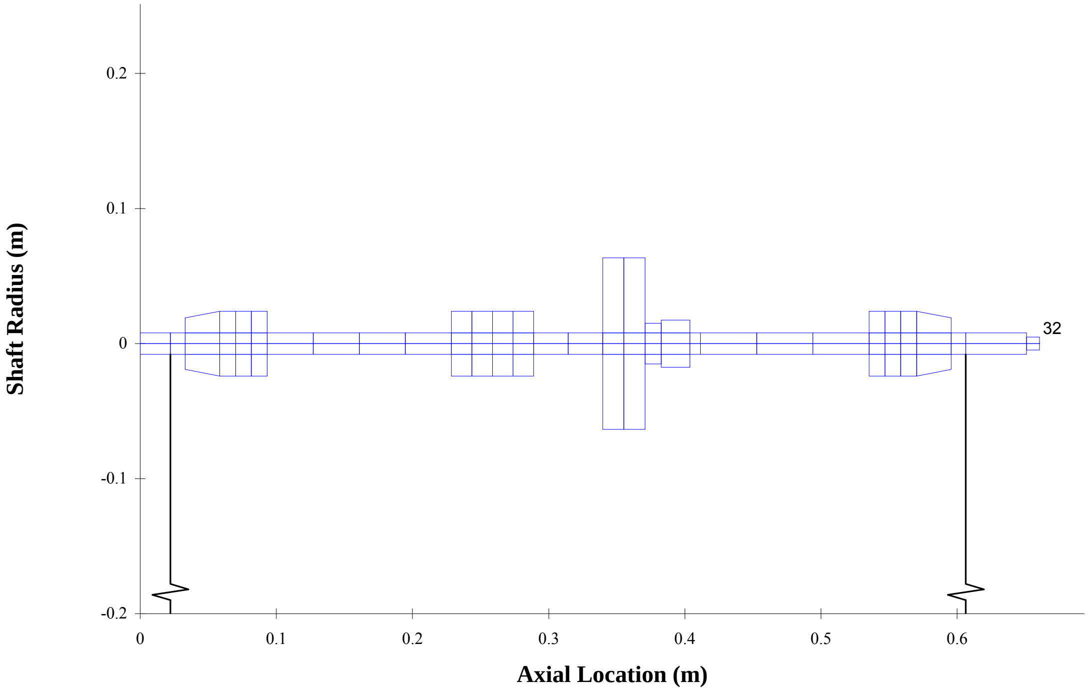

**Figure 3.6 XLRotor finite element model of rotor supported on ball bearings showing dimensions.**

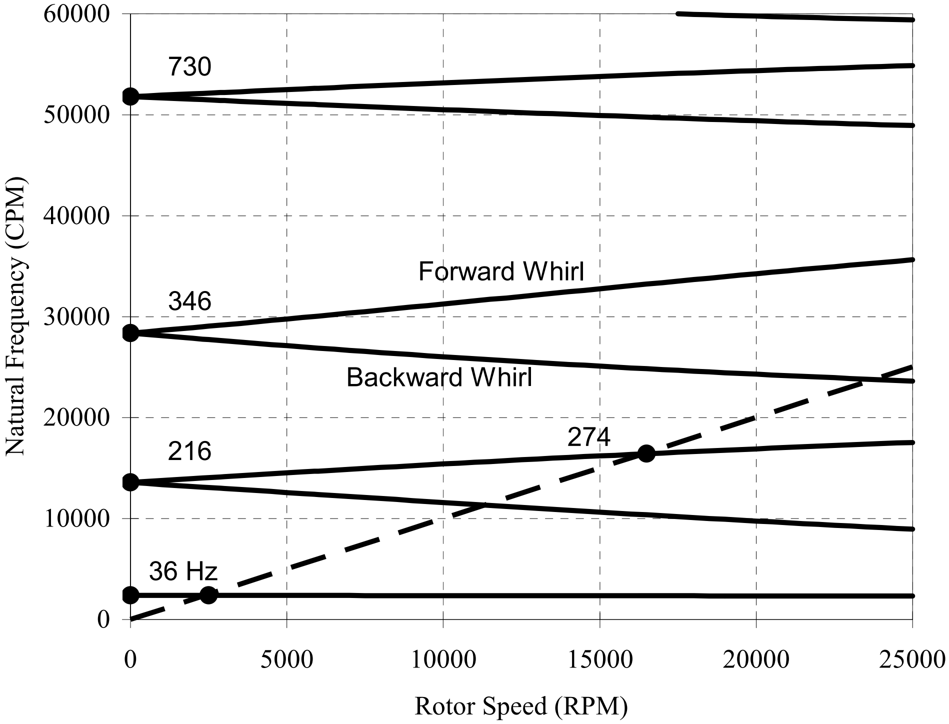

**Figure 3.7 Campbell diagram for rotor on ball bearings.**

The Campbell diagram is a graph of natural frequency as a function of running speed. As the rotor speeds up, gyroscopic effects cause an affective stiffening of the rotor which in turn causes a change in natural frequency. Significant change in natural frequency occurs in modes that have significant tilting at disks. The dashed line has a slope of 1. The critical speed can be read at the intersection point of a unity-slope line with the forward branch of each natural frequency.

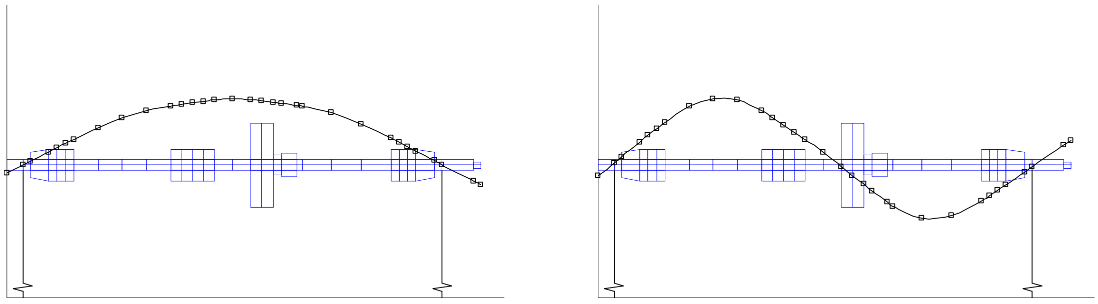

(a) 36 Hz

(b) 216 Hz

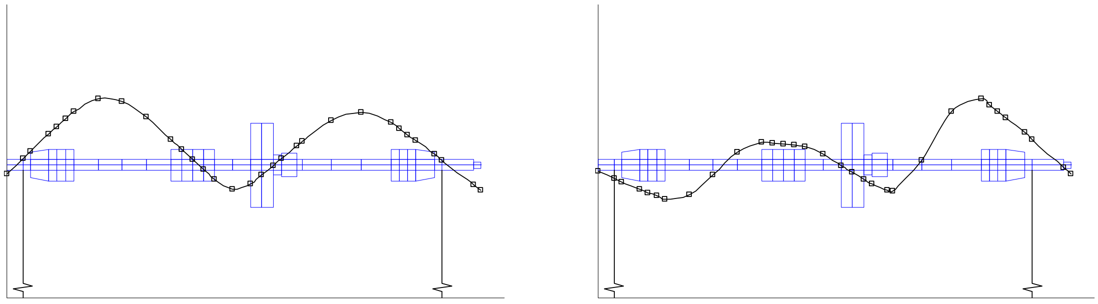

(c) 346 Hz

(d) 730 Hz

**Figure 3.8 Natural frequencies and mode shapes of the rotor supported on ball bearings.**

The maximum running speed of the test rig is 15000 RPM (250 Hz). Only the first mode can be excited in this range. Note that the second mode changes natural frequency significantly because of the tilting of the disk where as the first mode natural frequency is nearly unchanged.

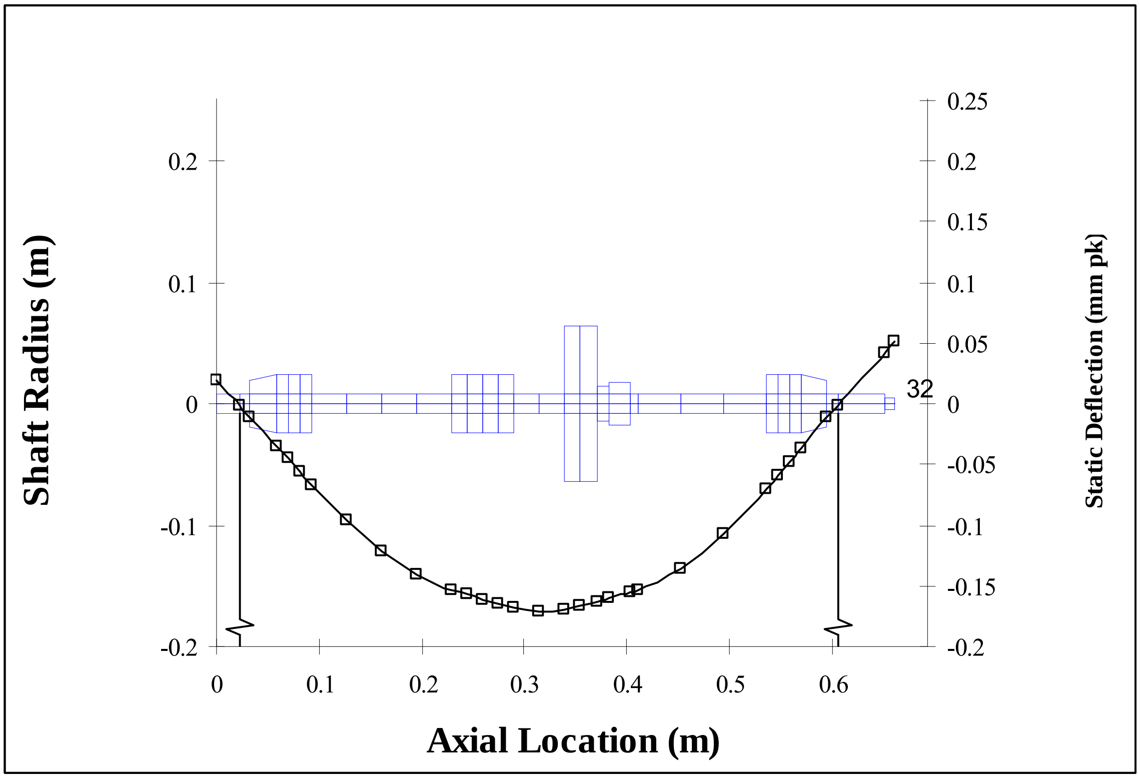

**Figure 3.9 Static deflection of the shaft is predicted to be 0.19 mm..**

XLRotor software was used to find static deflection of the rotor at the crack location to be approximately 0.19 mm and over 0.16 mm at the exciter sensor location. The orbit at running speed at the exciter sensor was found to have vertical amplitude of about 0.11 mm. These values show that the test rig does fall under the category of weight dominance. Because of this, the derivation of time varying stiffness in the Jeffcott rotor simulation is applicable to this case.

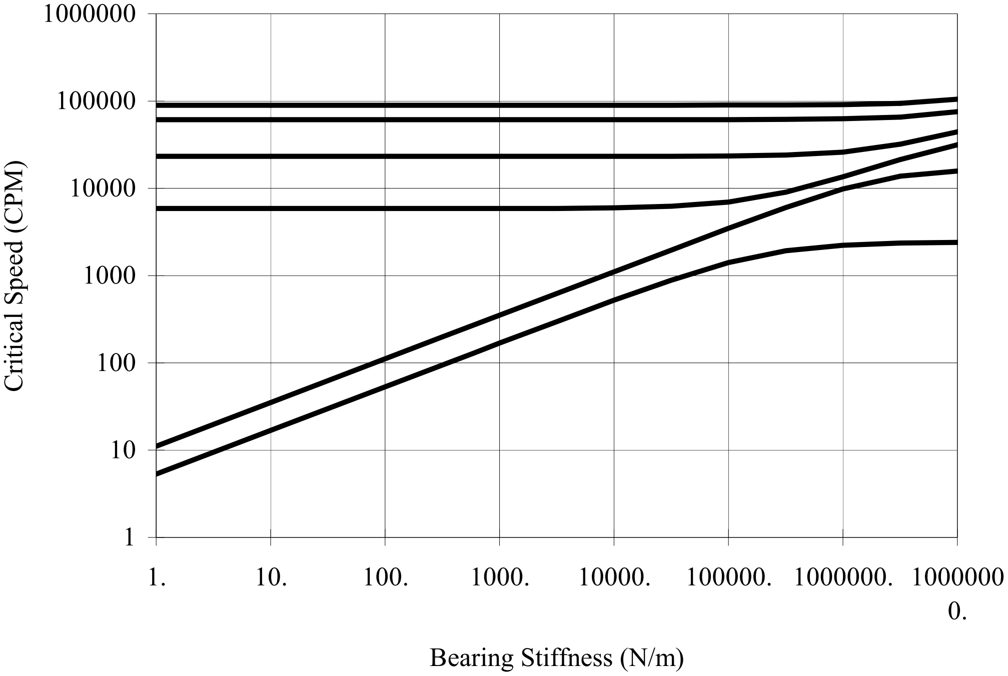

**Figure 3.10 Undamped critical speed map showing critical speed as a function of bearing stiffness.**

The ball bearings used for support of the rotor are Conrad type deep groove ball bearings. Equation (3.1), provided by the manufacturer, gives the stiffness of this type of bearing as a function of load.

$$k_b = 1166(\cos^{\frac{5}{3}} \theta_b)(I_b Z)^{\frac{2}{3}} (D_b)^{\frac{1}{3}} (F_b)^{\frac{1}{3}} \tag{3.1}$$

where:

$k_b$ = bearing stiffness [ $\frac{\text{N}}{\text{m}}$ ]
$\theta_b$ = contact angle = 0°
$I_b$ = number of active rows = 1
$Z$ = number of balls = 15
$D_b$ = ball diameter = 3.5 mm
$F_b$ = radial load [N]

The rotor being approximately 6.35 kg yields a radial load of about 31 N per bearing. This gives a radial stiffness of approximately $34 \times 10^6 \frac{\text{N}}{\text{m}}$. This value was used for modeling. Also, a value of $10\,\frac{\text{N-s}}{\text{m}}$ was assumed for damping and cross coupling of stiffness and damping was neglected.

### 3.3.2 Magnetically Levitated Rotor

The FE model with 33 stations, for the configuration with small disk and AMB support, is shown in Fig. 3.11. The Campbell diagram for the rotor supported on AMB's is presented in Fig. 3.12, and indicates number of rotor natural frequencies (critical speeds) and their change as function of speed. The summary of critical speeds and corresponding mode shapes is listed in Table 3.13.

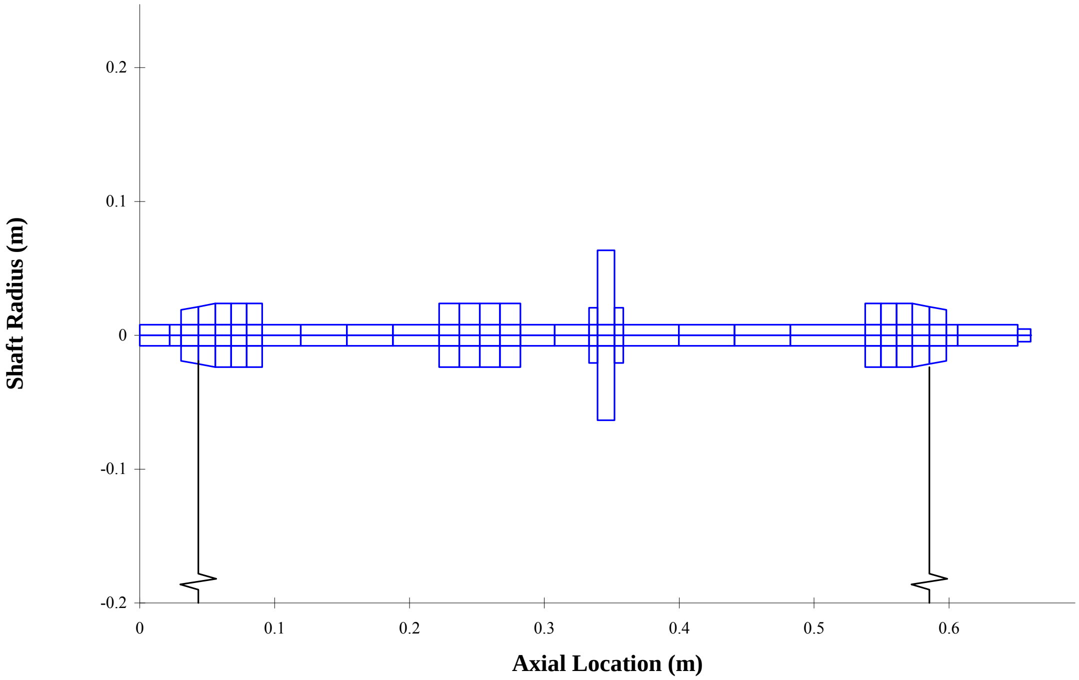

**Figure 3.11 XLRotor finite element model of rotor supported on AMB's showing dimensions.**

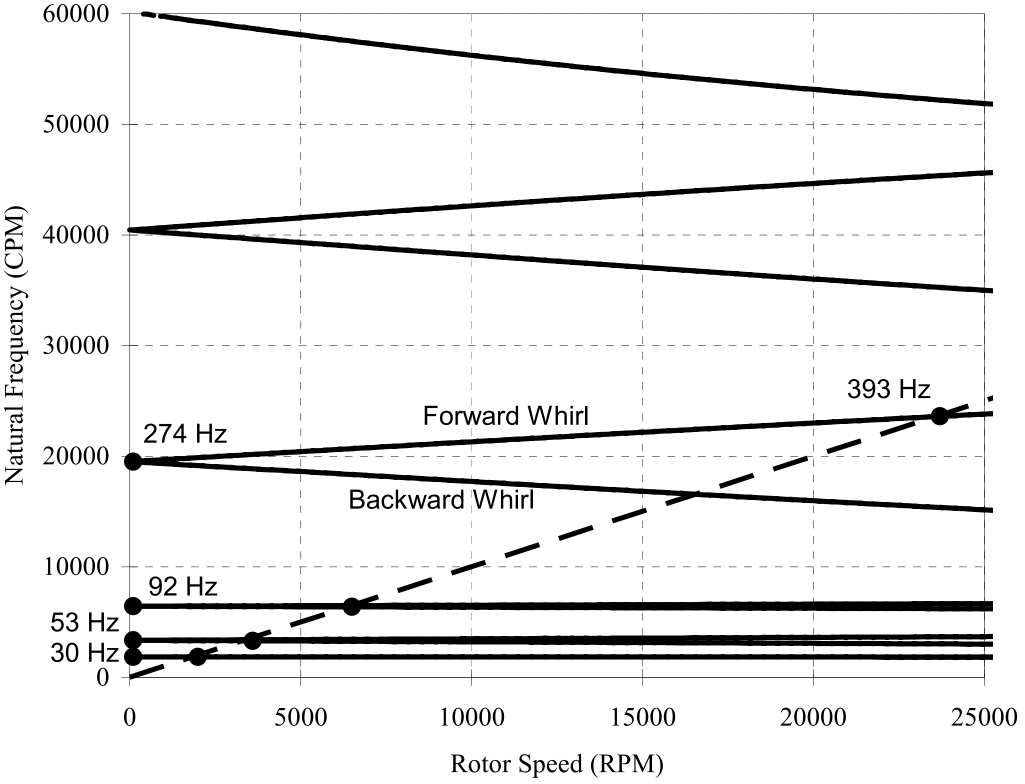

**Figure 3.12 Campbell diagram for rotor on AMB's.**

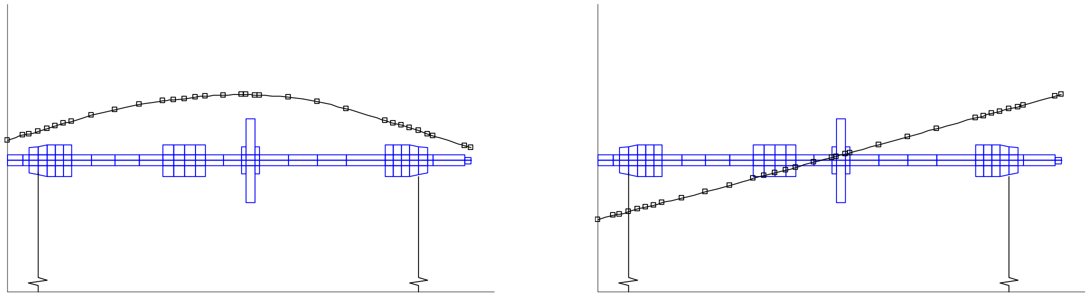

(a) 30 Hz

(b) 53 Hz

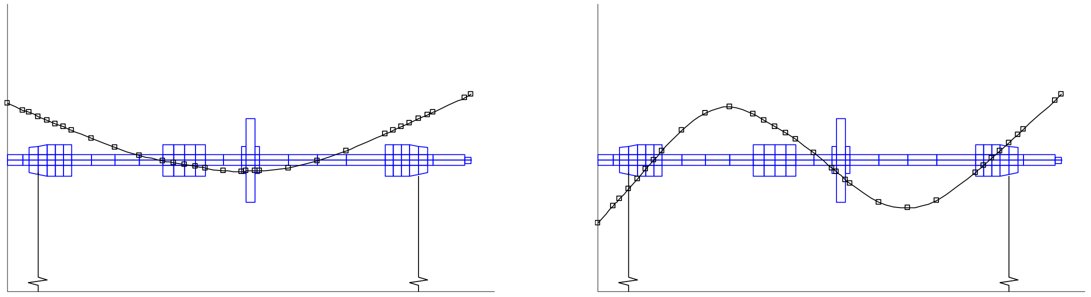

(c) 92 Hz

(d) 274 Hz

**Figure 3.13 Natural frequencies and mode shapes of the rotor supported on AMB's.**

## 3.4 Estimation of Injected Force and External Excitation Input

The force from a magnetic bearing actuator is directly proportional to the square of the current in the coil and inversely proportional to the square of the distance between the magnet and to rotor. This comes from classic magnetic theory and is brought to conclusion in the following equation (3.2). Note that this is the sum of the forces from the top and bottom magnets.

$$F = C\left[\left(\frac{I_{top}}{2\left(g_{ap}-q\right)}\right)^2 - \left(\frac{I_{bottom}}{2\left(g_{ap}+q\right)}\right)^2\right] \tag{3.2}$$

Here: $F$ = force [N]

$C$ = force calibration factor [ $\frac{\text{N-}\mu\text{m}^2}{\text{A}^2}$ ]

$I_{top}$ = current in the top coil [A]

$I_{bottom}$ = current in the bottom coil [A]

$g_{ap}$ = effective gap between the magnet and the rotor = 401.55 μm

$q$ = displacement of the rotor [μm]

The linearized stiffnesses used for the feedback control loop can be found by taking the partial derivative of the force equation with respect to displacement, $x$, and control current. The top current is the sum of the control current and the bias current and the bottom current is the difference between them.

$$F = C\left[\frac{(I_{bias}+I_{control})^2}{4(g_{ap}-q)^2} - \frac{(I_{bias}-I_{control})^2}{4(g_{ap}+q)^2}\right] \tag{3.3}$$

$$k_q \equiv \frac{\partial F}{\partial q} = C\left[(-2)(-1)\frac{(I_{bias}+I_{control})^2}{4(g_{ap}-q)^3} - (-2)(1)\frac{(I_{bias}-I_{control})^2}{4(g_{ap}+q)^3}\right] \tag{3.4}$$

$$k \equiv_i \frac{\partial F}{\partial I_{control}} = C\left[(2)(1)\frac{(I_{bias}+I_{control})}{4(g_{ap}-q)^2} - (2)(-1)\frac{(I_{bias}-I_{control})}{4(g_{ap}+q)^2}\right] \tag{3.5}$$

In this case, the set point is the center of the bearing, so the equation is linearized around $x = 0$. And, with no deflection, $I_{control} = 0$. Making these substitutions, the equations can be simplified to:

$$k_q = \frac{CI_{bias}^2}{g_{ap}{}^3} \tag{3.6}$$

$$k_i = \frac{CI_{bias}}{g_{ap}{}^2} \tag{3.7}$$

The calibration factor, *C*, is theoretically given by equation (3.8):

$$C = \mu_0 A N^2 \cos(\alpha) \tag{3.8}$$

With $\mu_0$ being the permeability of a vacuum ($4\pi\times10^{-7}\ \frac{\mathrm{H}}{\mathrm{m}}$), *A* being the area of a pole face, *N* being the number of windings in a coil and *α* being the angle of the pole face. See Plonus [1978] for a derivation of equation (3.8) and a thorough explanation of the force generated by an electromagnet.

The value of *C* in equation (3.2) was experimentally determined to be $\mathrm{C} = 21\,\frac{\mathrm{N}\text{-}\mu\mathrm{m}^2}{\mathrm{A}^2}$. This was accomplished by the measurement of the stiffness of the rotor and then matching it with the slope of the force-displacement relationship curve which obtained experimentally. In other words, the displacement of the shaft in response to known forces was measured and plotted below. Then, the displacement of the MB rotor in response to known currents was measured. Then, Equation (3.2) was used to plot force-displacement relationship on the same plot and the value of *C* was tuned so the curves would coincide.

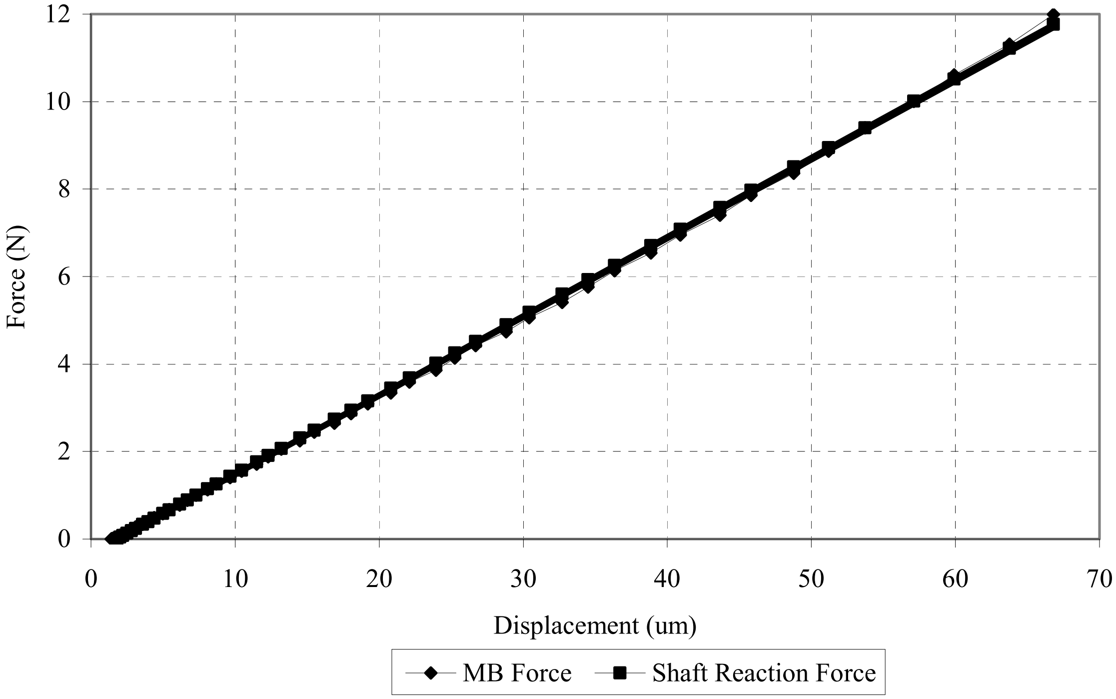

**Figure 3.14 Force balance between magnetic bearing and shaft reaction force to tune magnetic bearing calibration factor.**

For the given AMB, this calibration factor results in a nominal static load carrying capacity of 293 N (66 lbs) for the AMB's used in this work. The value of this limiting force corresponds to the maximum DC current (assuming zero displacement) in equation (3.2). The magnetic bearing is essentially an R-L circuit because the magnetic coil has some internal resistance and acts as an inductor. The transfer function of R-L circuits is readily known.

$$I(s) = \frac{V(s)}{Ls + R} \tag{3.9}$$

Here, *I* is current in amps, *V* is voltage in volts, *L* is inductance in Henrys and *R* is resistance in Ohms. Force from the magnetic actuator is a function of current, which is limited by the available voltage. This limit is called the *slew rate* of the bearing. For this particular AMB, the dynamic load capacity of the bearing is shown in Fig 3.15 below.

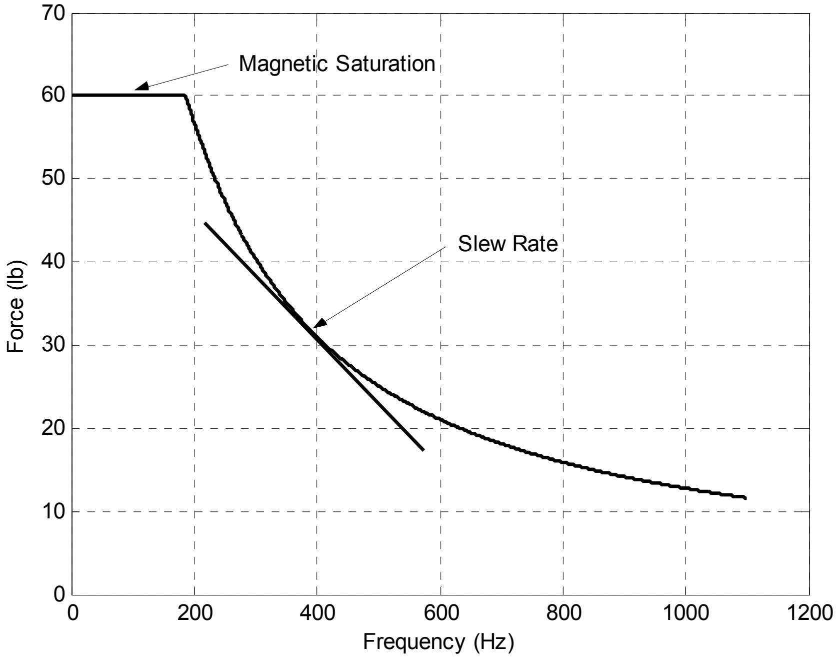

**Figure 3.15 Dynamic load capacity chart for AMB showing slew rate.**

Note that the magnetic saturation can be seen at 60 lb.

For this experiment, the harmonic signal injection must therefore have and amplitude of less than 266 N (60 lb.) and remain below approximately 200 Hz. It will be seen that the selected injections are well within these bounds.

# CHAPTER IV

# DAMAGE DETECTION: EXPERIMENTAL RESULTS

## 4.1 Introduction

As previously stated, there are two parts to this experiment, damage detection for a rotor on ball bearing supports and damage detection for a magnetically levitated rotor. For each, an undamaged (healthy) rotor is run at steady state and vibration data collected. Then the rotor is run again with a harmonic current input to a magnetic bearing and the position data collected. The exciter magnetic bearing is used for force injection in the vertical axis in the ball bearing trials. The outboard AMB (furthest from the motor) is used to inject harmonic force at 45° in the magnetic levitation trials. The integers 2, 3, and 4 are selected as *n* values in equation (2.14) to calculate force injection frequencies. The frequency spectrum is found for each set of position data sets by using the FFT algorithm. The same force injection cases are repeated with rotor shafts intentionally damaged with a wire EDM cut at the bearing midspan. The wire EDM cut is approximately 0.1143 mm (4.5 mils) wide and has a curved radius at the edge shown in Figure 4.1. Then the frequency response of the cut shaft is found and compared to that of the healthy rotor. The difference between the damaged rotor response and the undamaged rotor response is found by subtracting the undamaged frequency spectrum from the damaged one. The difference is plotted along with the two frequency spectrums.

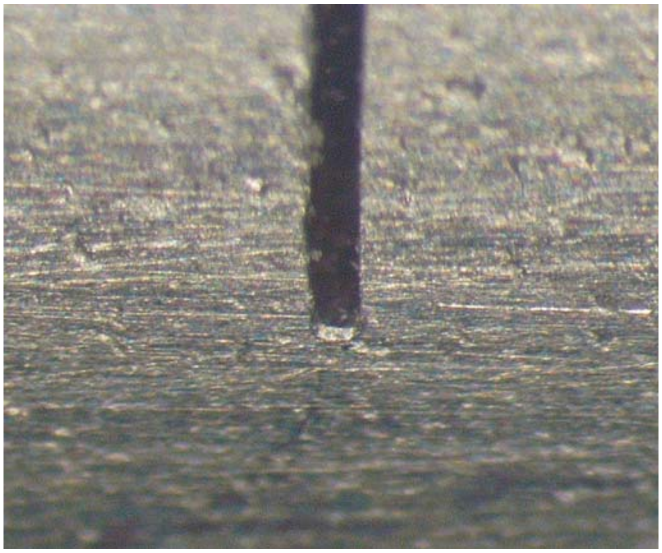

**Figure 4.1 Bottom of a wire EDM cut in a steel 0.625 in. diameter shaft.**

The ball bearing support trials include a healthy shaft, 25% diameter cut shaft, and 40% diameter cut shaft. Also, in an attempt to achieve true breathing behavior, a metal shim is inserted into the 25% and 40% cuts, and two more trials are run. The EDM cut, small as it is, does not close when it is on the underside of the rotating shaft. Without this periodic opening and closing in time with rotation, the situation will not be equivalent to what was modeled mathematically and simulated. Care was taken to assure that the shim is only large enough to just fit in the cut and thus leave no residual stresses in the shaft.

This is a total of 20 cases and 16 comparisons. For each, data is collected for 30 seconds at 10 kHz and the frequency spectrum of 4 data collections is averaged.

The magnetic levitation trials include only a 40% diameter EDM cut shaft and healthy shaft rotors. These cases prove sufficient in demonstrating the crack detection method is viable for magnetically levitated rotors. This gives a total of 8 cases and 4 comparisons. For each, data is again collected for 30 seconds at 10 kHz but the frequency spectrum of 18 data collections is averaged.

## 4.2 Conventional Bearing Support

### 4.2.1 Identification of Transfer Function

For system identification, the transfer function is found for each undamaged shaft trial and each EDM cut shaft trial. This is done using MBScope Analyzer tool which injects a harmonic force over a range of frequencies and measures the amplitude of response at each frequency. Figure 4.2 below shows results for the healthy shaft and Figure 4.3 below shows the change in first natural frequency between the healthy rotor and the 40% cut rotor. The first natural frequency is expected to drop due to the decrease in stiffness of the shaft due to the damage.

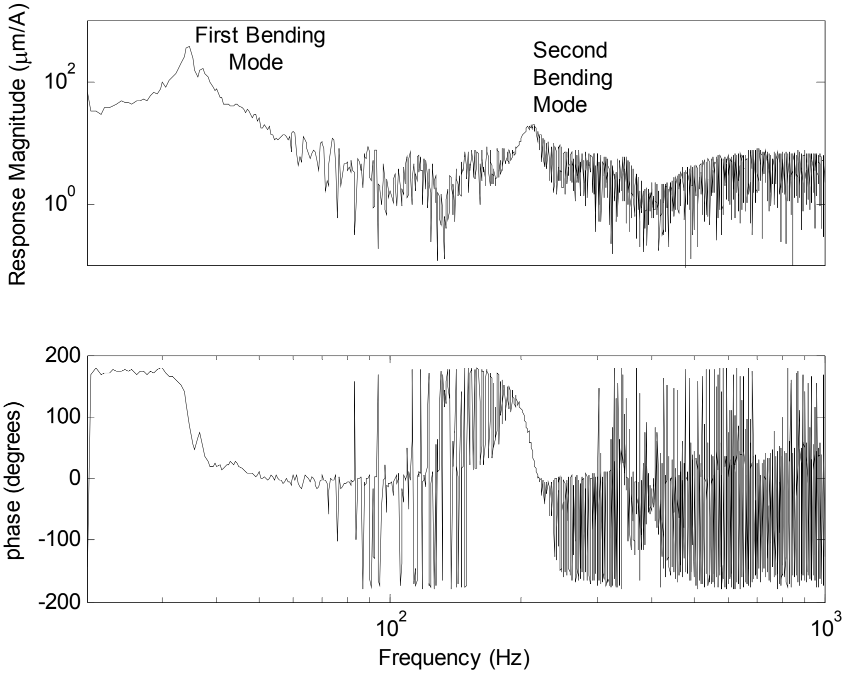

**Figure 4.2 Bode Plot of undamaged shaft on ball bearings rotating at 600 RPM. Input at magnetic bearing actuator and output at actuator sensor. Data collected using MBScope Analyzer tool.**

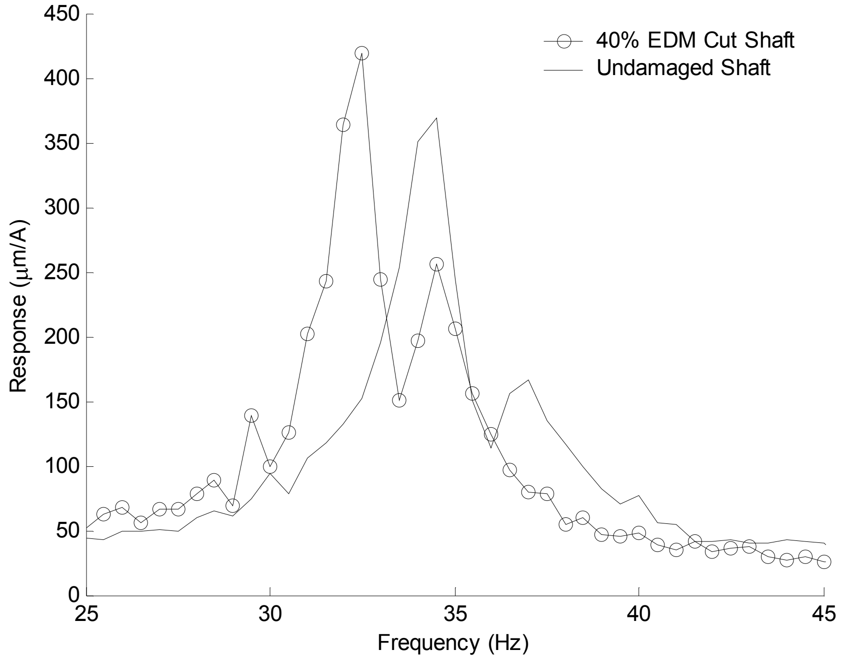

**Figure 4.3 Close up of first resonance peek of Figure 4.2. Transfer function of damaged shaft also included for comparison.**

### 4.2.2 Experimental Results: Healthy and Damaged Rotor

A harmonic current is input to the exciter magnetic bearing however, as shown in equation (3.2), the resulting force on the rotor is a function of both current and rotor position. Figure 4.4 below shows the actual periodic force injected to the system as calculated by equation (3.2). The main frequency in the injection force is the current injection frequency. Figure 4.4 also includes the values of the injection frequencies and magnitudes. Note that higher injection amplitudes are possible because the mass of the rotor is of course a second order system and the deflection is less at higher frequencies.

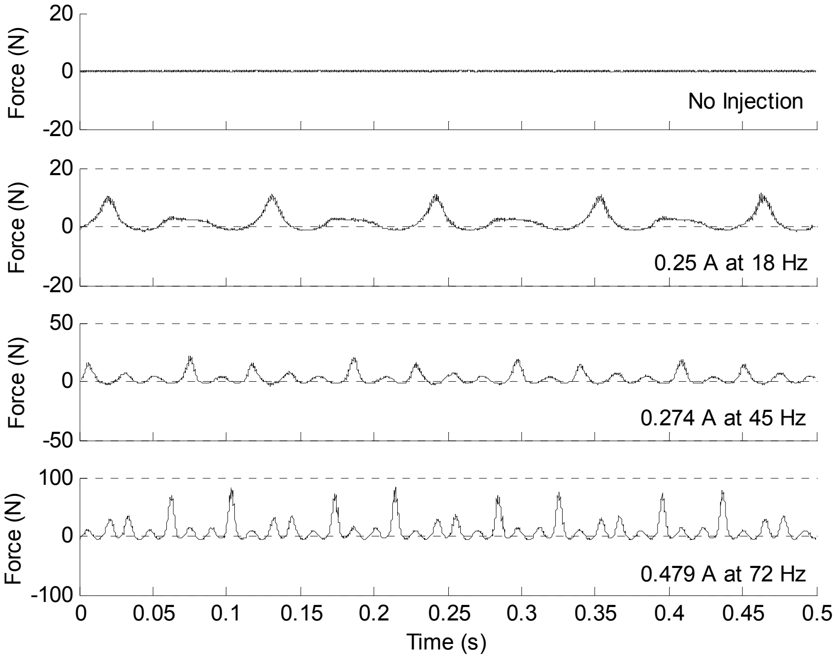

**Figure 4.4 Example of four force injection cases for ball bearing trials calculated from experimental current and position data using equation (3.2).**

Figures 4.5 through 4.8 show the four injection cases for the 25% diameter EDM cut shaft. In Figure 4.5 where there is no damage and no injection, there is a large peek at one times running speed due to unbalance which causes a synchronous force. Also present are peeks at multiples of the running speed indicating the non-crack rotor malfunctions discussed in chapter one such as misalignment and dynamic unbalance. These peeks are very small compared to the 1X peek; note the logarithmic scale. The small transient response peek also can be seen at the natural frequency, 36 Hz. In Figure 4.5, where there is damage and no injection, much the same results are found. The difference between these results shows only a peek at 1X and the shift in natural frequency. The growth in 1X component is predicted because of the decrease in shaft stiffness but is most likely actually due to a small difference in shaft bow between the healthy and cut shafts. A difference in 2X component is also predicted due to non symmetric shaft stiffness, but is not found experimentally. Upon force injection in Figures 4.6-4.8, the same results are seen with the addition of combinational frequency peeks at the predicted frequencies. Unlike the numerical simulation in Chapter 2, the combinational frequencies appear in both the damaged and control trials. This may be due to nonlinearities in the real system, other than a crack, that causes the same cross talk between frequencies and resulting combined frequencies. There is almost no observable difference in combinational frequency peeks with the exception of the 18 Hz peek when a frequency of 72 Hz in injected. See Figure 4.8.

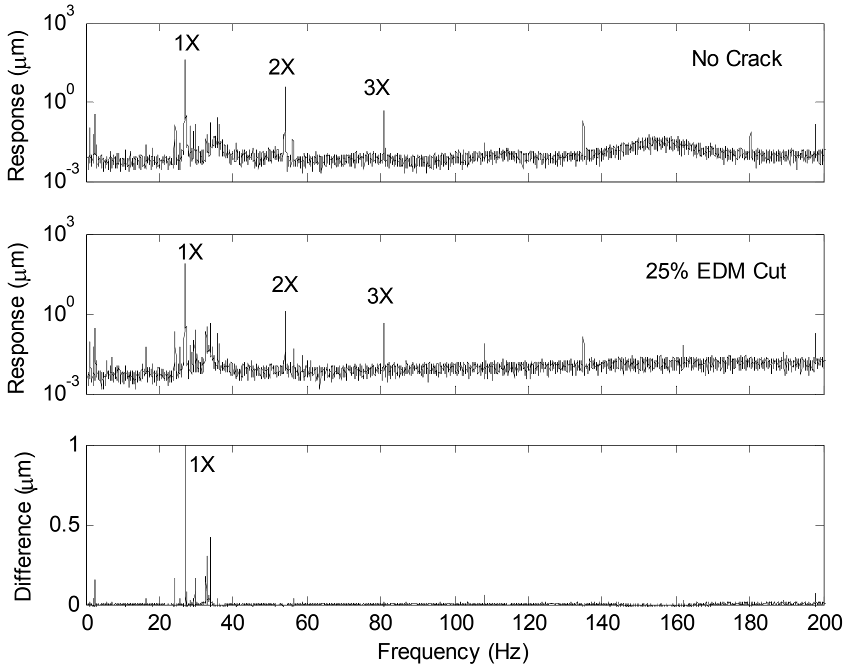

**Figure 4.5 Frequency spectrum of healthy shaft and 25% EDM (not filled) cut shaft rotating at 27 Hz on ball bearings with no force injection.**

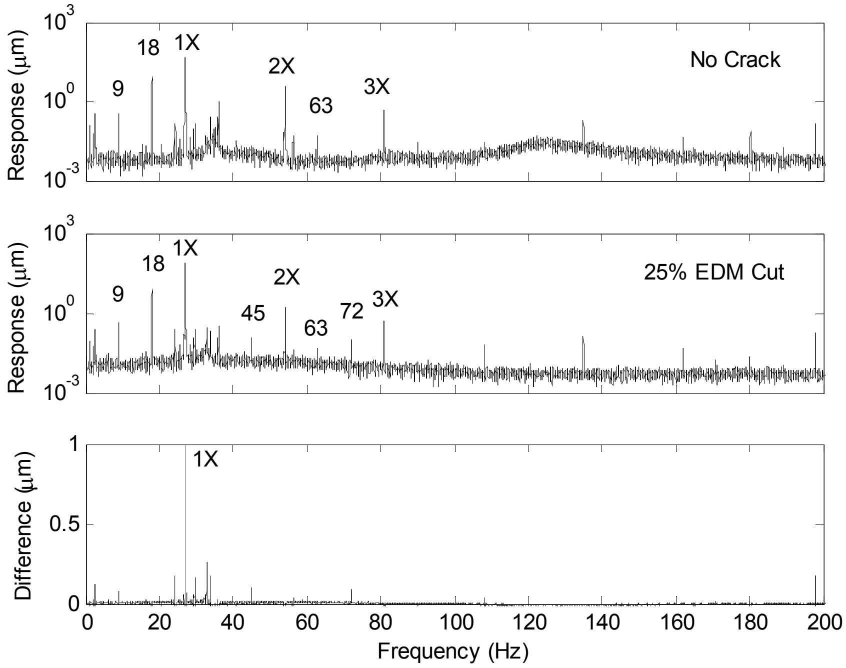

**Figure 4.6 Frequency spectrum of healthy shaft and 25% EDM (not filled) cut shaft rotating at 27 Hz on ball bearings with force injection of 0.209 A at 18 Hz.**

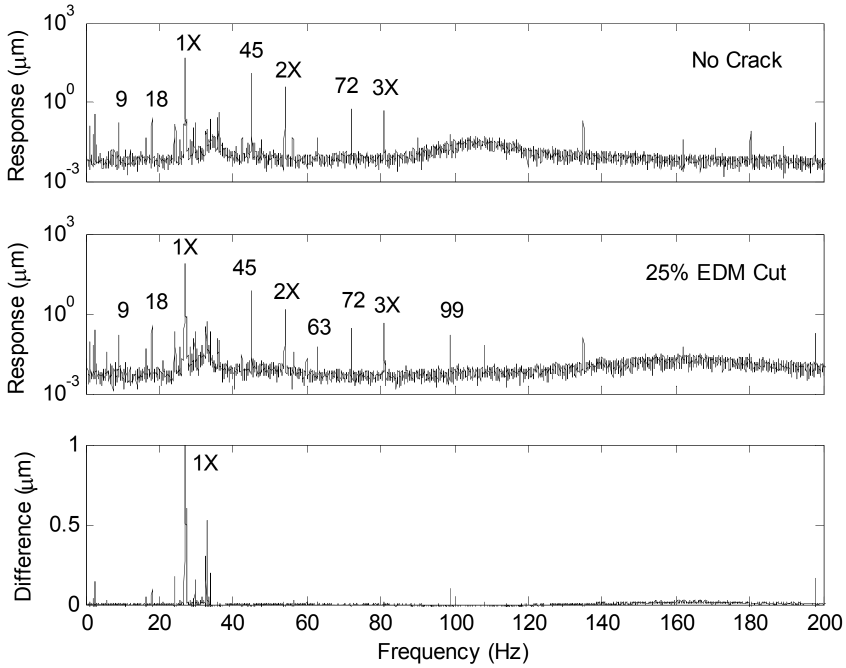

**Figure 4.7** Frequency spectrum of healthy shaft and 25% EDM (not filled) cut shaft rotating at 27 Hz on ball bearings with force injection of 0.221 A at 45 Hz.

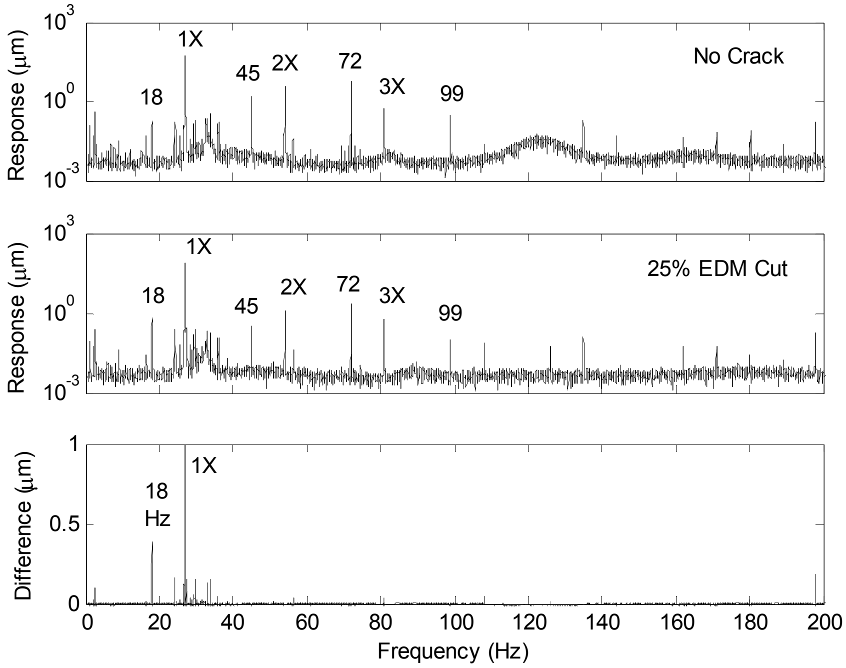

**Figure 4.8** Frequency spectrum of healthy shaft and 25% EDM (not filled) cut shaft rotating at 27 Hz on ball bearings with force injection of 0.297 A at 72 Hz.

Figures 4.9 through 4.12 show the results for the 40% diameter EDM cut shaft trials. Figure 4.9, no force injection, shows similar results as Figure 4.5, no injection for the 25% cut. The main difference is that now the predicted 2X peek is seen, the 40% cut causing significantly more asymmetric stiffness than the 25% cut. The 1X and 2X peeks can also be seen in the injection trials. Figure 4.10 shows results for 18 Hz injection and an observable difference in many combinational frequencies can be seen between the cut shaft and the control specimen. Figures 4.11 and 4.12, for 45 Hz and 72 Hz injection respectfully, show only difference peeks at the 18 Hz combined frequencies.

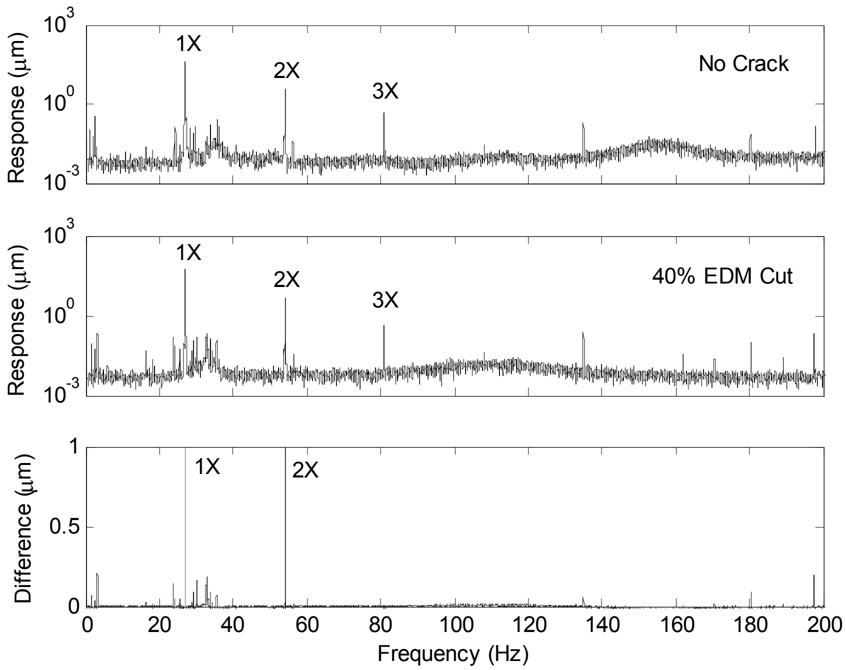

**Figure 4.9 Frequency spectrum of healthy shaft and 40% EDM (not filled) cut shaft rotating at 27 Hz on ball bearings with no force injection.**

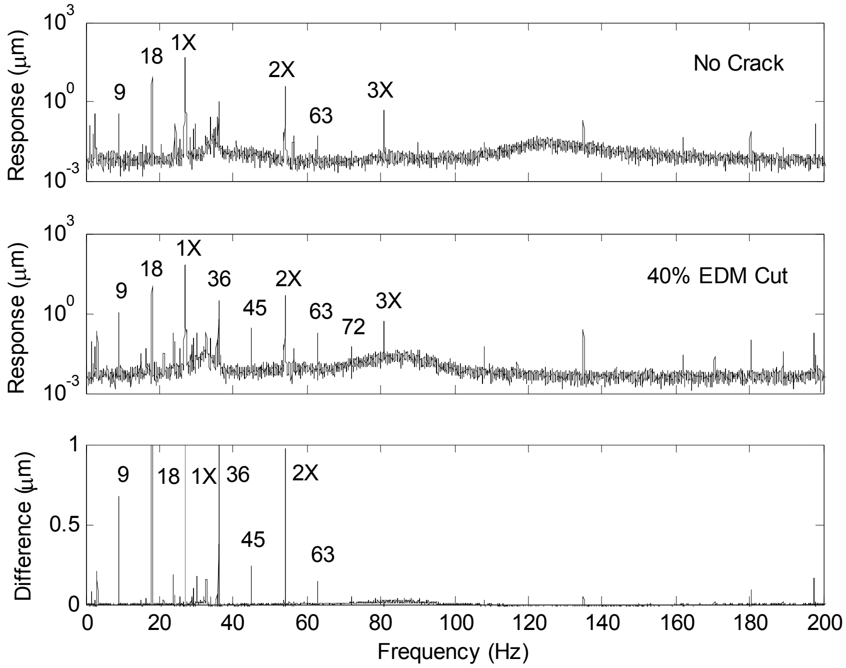

**Figure 4.10 Frequency spectrum of healthy shaft and 40% EDM (not filled) cut shaft rotating at 27 Hz on ball bearings with force injection of 0.25 A at 18 Hz.**

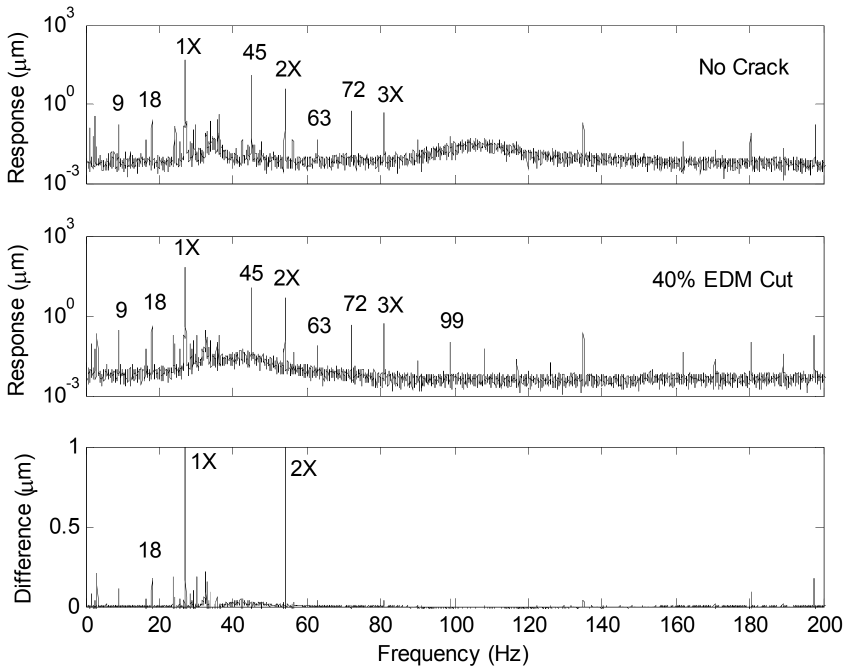

**Figure 4.11 Frequency spectrum of healthy shaft and 40% EDM (not filled) cut shaft rotating at 27 Hz on ball bearings with force injection of 0.274 A at 45 Hz.**

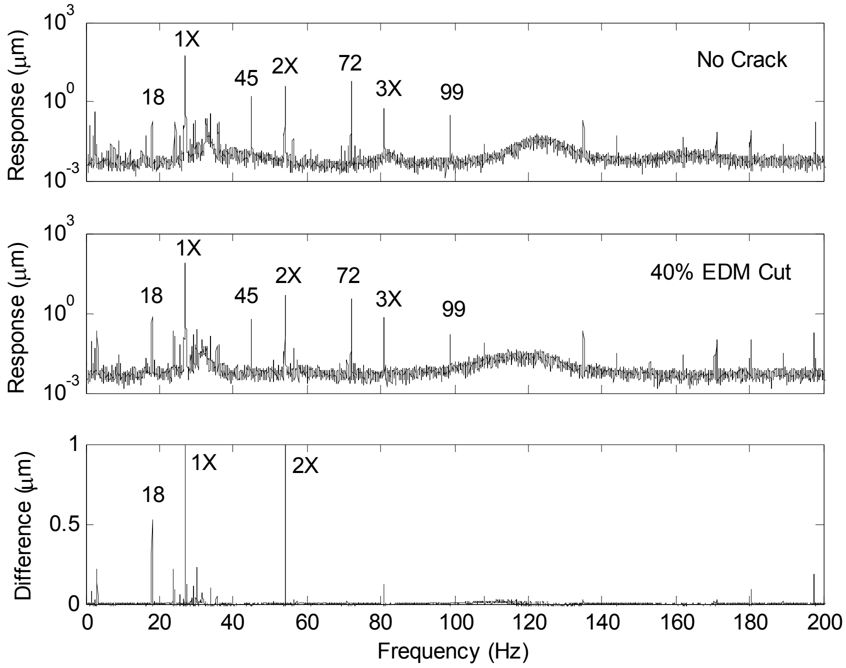

**Figure 4.12 Frequency spectrum of healthy shaft and 40% EDM (not filled) cut shaft rotating at 27 Hz on ball bearings with force injection of 0.368 A at 72 Hz.**

Figures 4.13 through 4.16 show results for the shim filled 25% diameter EDM cut shaft trials. For no injection, 1X difference and natural frequency shift can be seen similar to the non shim filled case. For 18 Hz injection, Figure 4.14, a difference in the combinational frequency at 45 Hz can be seen. Also, the difference in the 1X component is much less. In Figures 4.15 and 4.16, injection at 45 Hz and 72 Hz respectfully, almost no difference between the damaged and undamaged rotors can be seen at all.

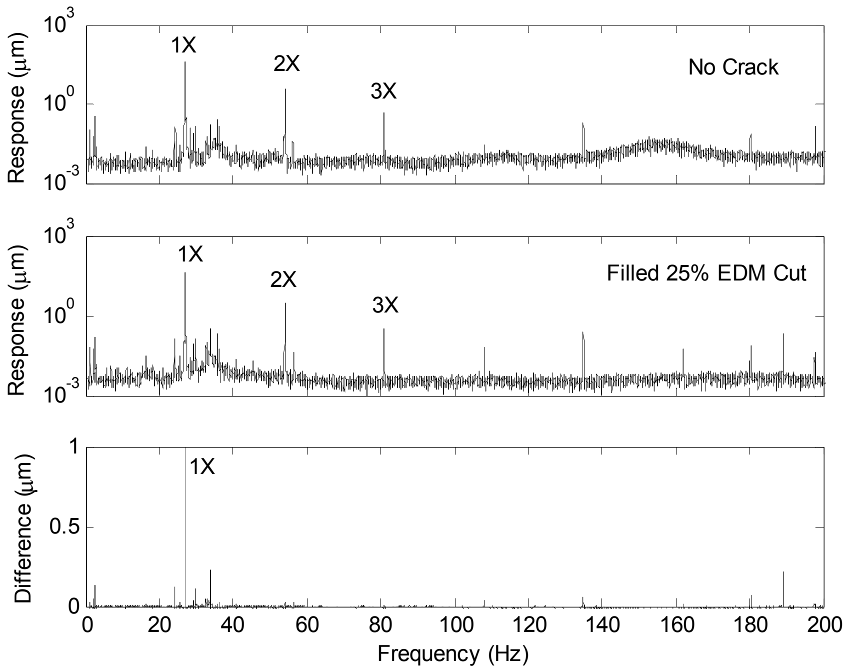

**Figure 4.13 Frequency spectrum of healthy shaft and 25% EDM (filled) cut shaft rotating at 27 Hz on ball bearings with no force injection.**

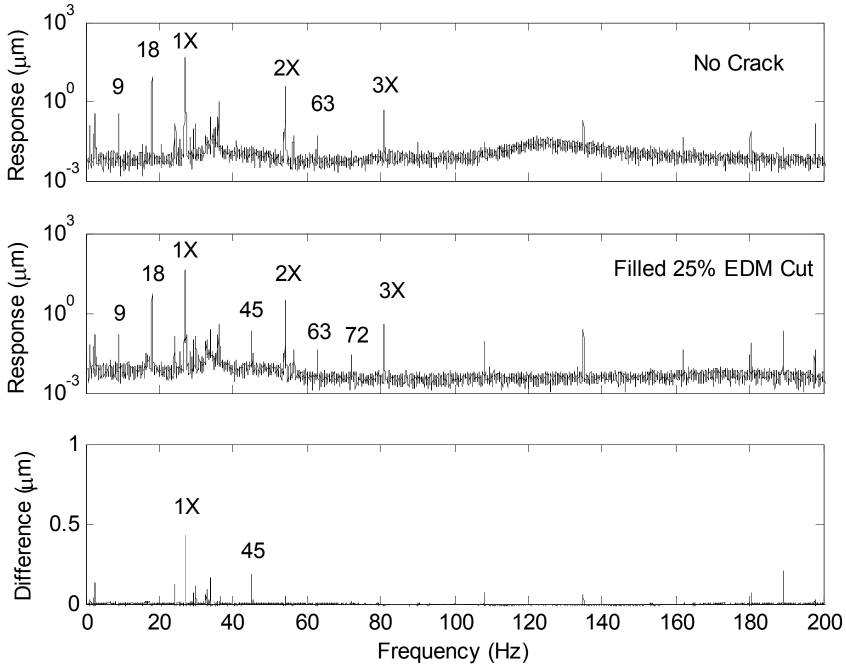

**Figure 4.14 Frequency spectrum of healthy shaft and 25% EDM (filled) cut shaft rotating at 27 Hz on ball bearings with force injection of 0.209 A at 18 Hz.**

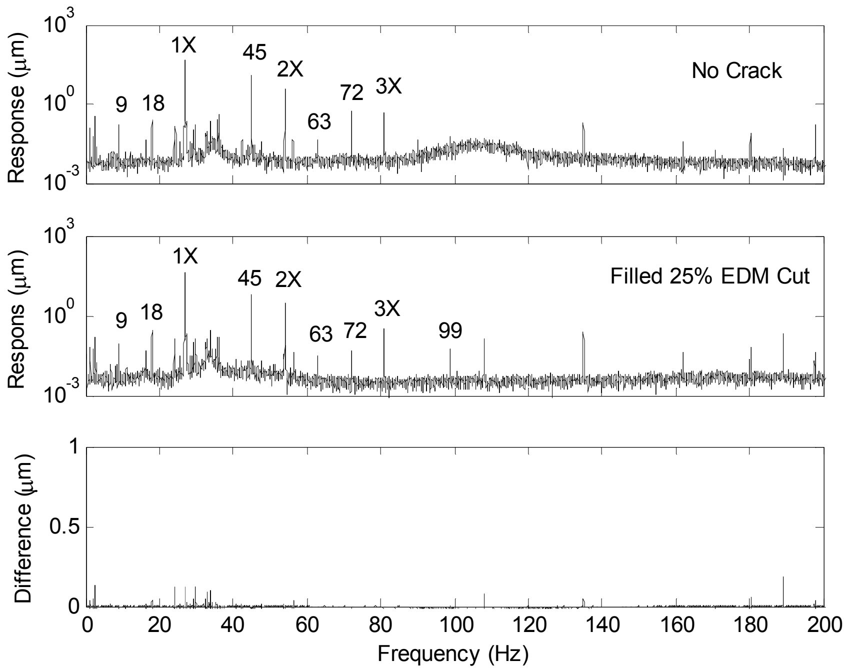

**Figure 4.15 Frequency spectrum of healthy shaft and 25% EDM (filled) cut shaft rotating at 27 Hz on ball bearings with force injection of 0.221 A at 45 Hz.**

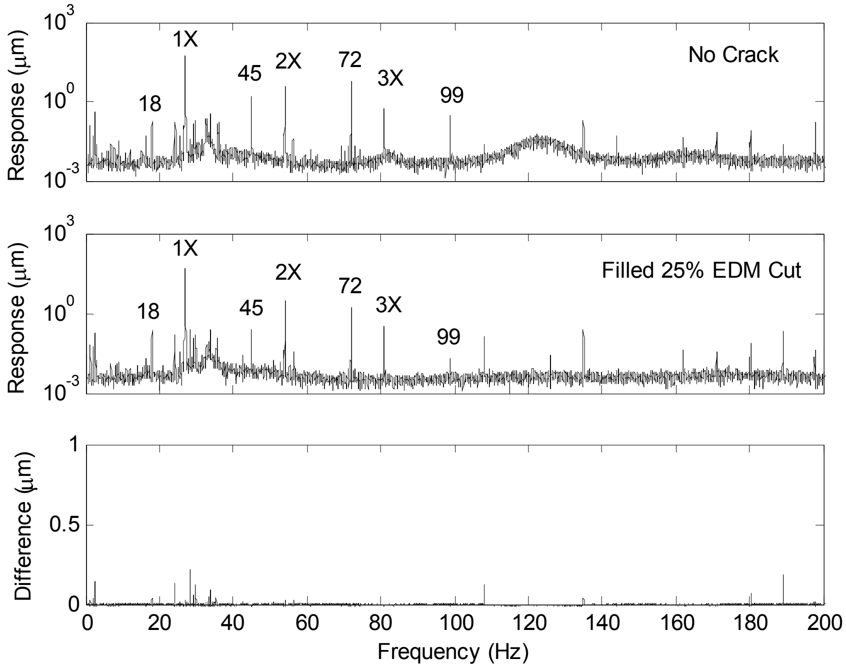

**Figure 4.16 Frequency spectrum of healthy shaft and 25% EDM (filled) cut shaft rotating at 27 Hz on ball bearings with force injection of 0.299 A at 72 Hz.**

Figures 4.17 through 4.20 show results for the shim filled 40% diameter EDM cut shaft. Figure 4.17 shows results for no force injection and the results are similar to the non shim filled case with the important difference of a larger difference in 3X component and a lesser difference in 2X component. This is change due to the presence of the shim. This change may also be present in the 25% cut case but be two small identify. The injection for the shimmed 40% EDM cut reveals combinational frequencies, especially for the 18 Hz injection case.

Figures 4.21 through 4.24 compare the simulation results from Chapter 2 to the experimental results. Only the 40% damage cases were compared as the 25% showed very little experimental results. Each figure contains three plots of the difference between the damaged case and the undamaged case. The top plot in each figure is the simulation results, the middle plot is for the EDM cut experimental results, and the bottom plot is for the shim filled EDM cut experimental results. Figure 4.21 shows the differences with no injection. There are no combined resonances present. The simulation shows vibration components at 2X and 3X running speed indicating a crack. The experimental results however show a 2X component in the EDM cut case and a 3X component in the shim filled EDM cut case. This indicates that a shim filled EDM cut may not be a perfect synthesis of a crack. Figures 4.22-4.24 show results for 18 Hz, 45 Hz and 72 Hz injection cases. In each, combined resonances are present at the simulation predicted frequencies. Also, the 2X and 3X component discrepancy found in the no injection case is present.

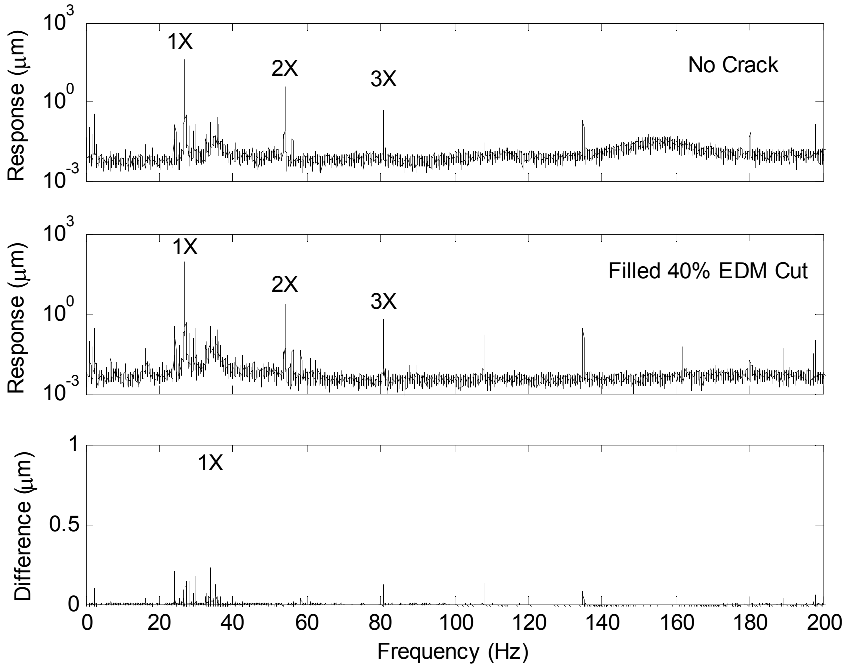

**Figure 4.17 Frequency spectrum of healthy shaft and 40% EDM (filled) cut shaft rotating at 27 Hz on ball bearings with no force injection.**

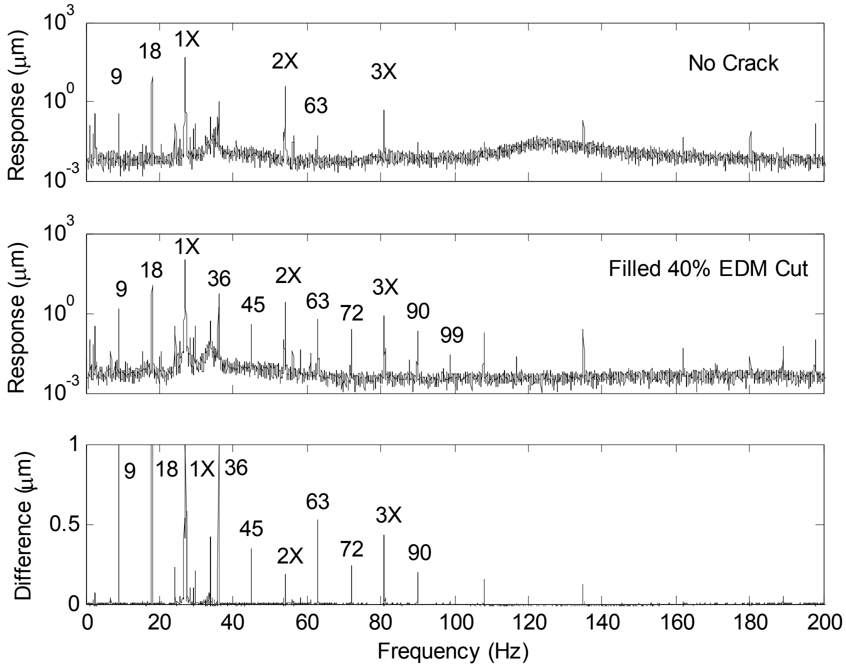

**Figure 4.18 Frequency spectrum of healthy shaft and 40% EDM (filled) cut shaft rotating at 27 Hz on ball bearings with force injection of 0.25 A at 18 Hz.**

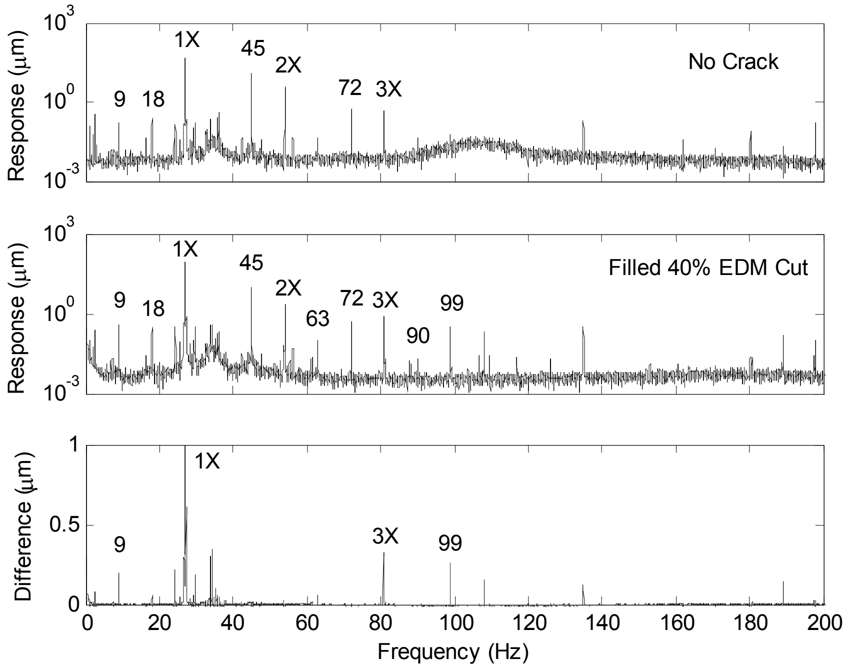

**Figure 4.19 Frequency spectrum of healthy shaft and 40% EDM (filled) cut shaft rotating at 27 Hz on ball bearings with force injection of 0.274 A at 45 Hz.**

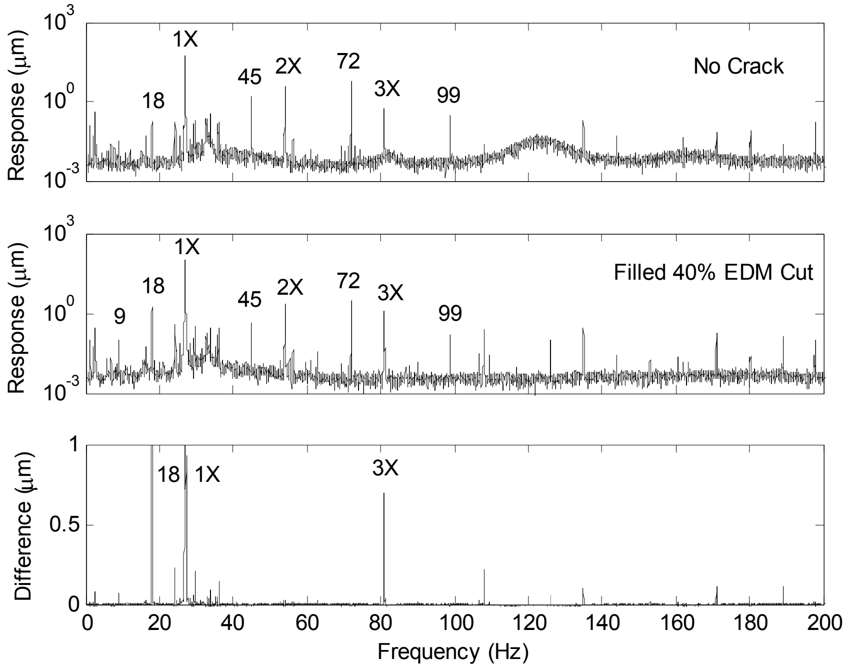

**Figure 4.20 Frequency spectrum of healthy shaft and 40% EDM (filled) cut shaft rotating at 27 Hz on ball bearings with force injection of 0.368 A at 72 Hz.**

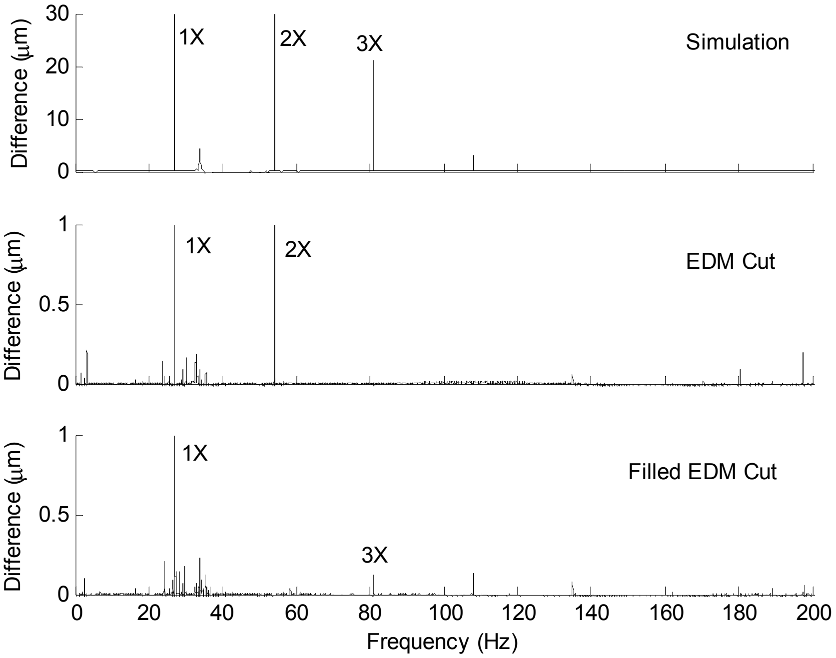

**Figure 4.21** Comparison of difference from control test for simulation and experimental results for 40% cut shaft and no injection (See Figures 2.9, 4.9 and 4.17).

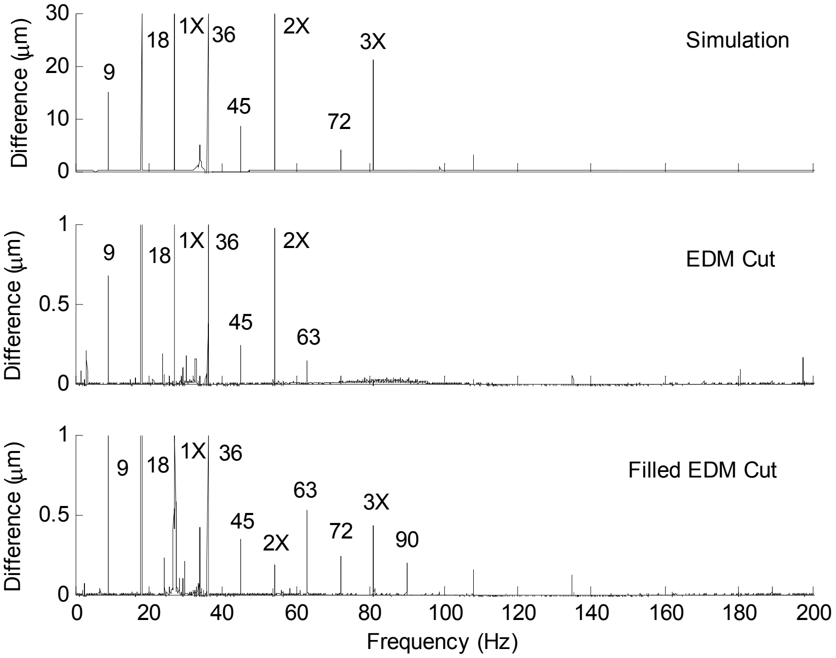

**Figure 4.22** Comparison of difference from control test for simulation and experimental results for 40% cut shaft and 18 Hz injection (See Figures 2.10, 4.10 and 4.18).

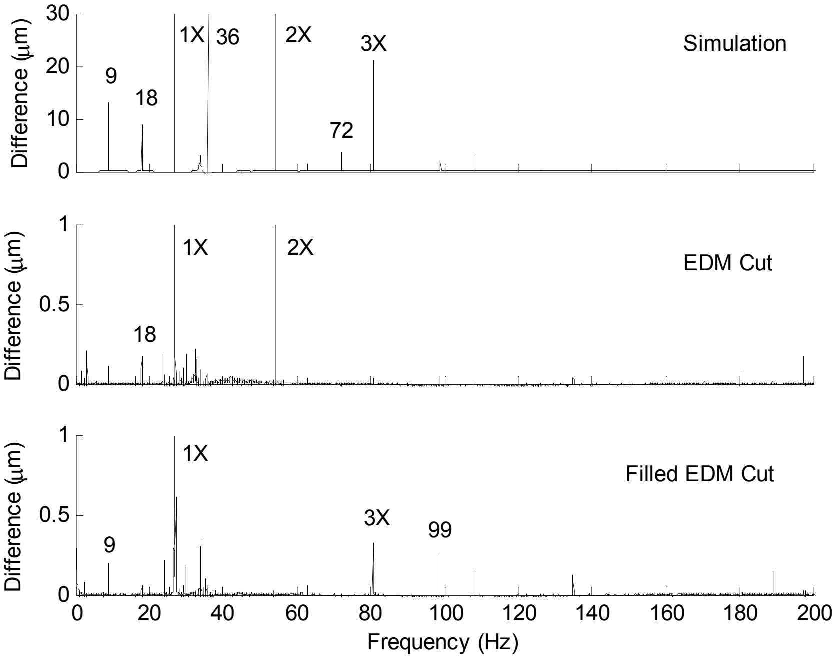

**Figure 4.23 Comparison of difference from control test for simulation and experimental results for 40% cut shaft and 45 Hz injection (See Figures 2.11, 4.11 and 4.19).**

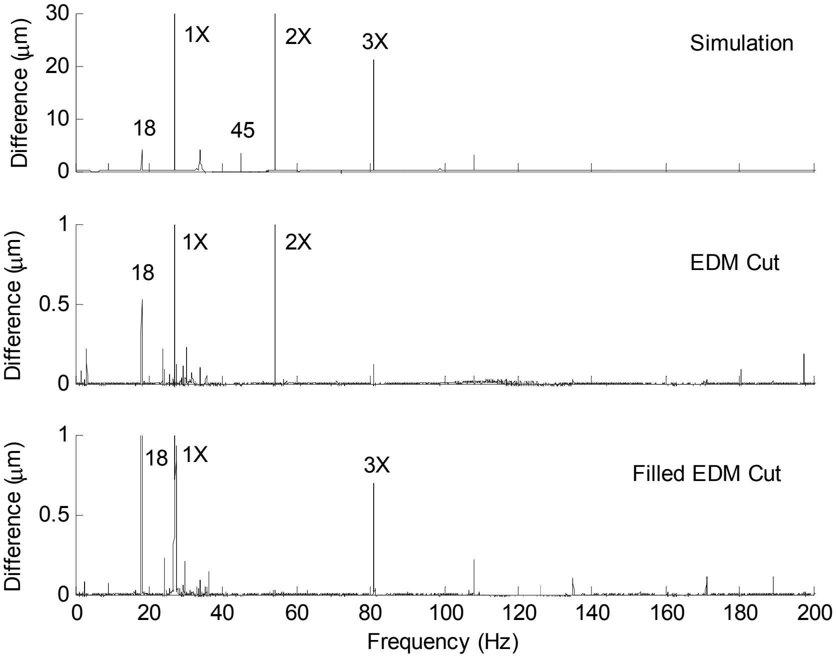

**Figure 4.24 Comparison of difference from control test for simulation and experimental results for 40% cut shaft and 72 Hz injection (See Figures 2.12, 4.12 and 4.20).**

## 4.3 Magnetically Levitated Rotor

### 4.3.1 Controller Design and Implementation

A MatLab Simulink model is used to design and examine the behavior and verify the stability of the magnetic levitation controller before the levitated trials are conducted experimentally. Figure 4.25 shows the Simulink model of the overall closed loop feedback control system. A state-space representation of the rotor is generated using the program MODAL version 1.5 which is part of the software package generated by the University of Virginia Rotating Machinery and Controls (ROMAC) Laboratory. This serves as the plant in the control loop and has six force inputs and eight position outputs. Each magnetic bearing is controlled independently in SISO fashion. Figure 4.26 shows the model for each magnetic bearing axis. The linear approximations discussed in section 3.2.1 are used.

An impulse input at 1 sec. was used to test the controller's stability. Figures 4.27 and 4.28 show the impulse response. Figure 4.27 is the response of a levitated non-rotating rotor and Figure 4.28 shows the response of a rotor spinning at 27 Hz with corresponding unbalance force at the disk. An unbalance of 0.001 kg-m is used.

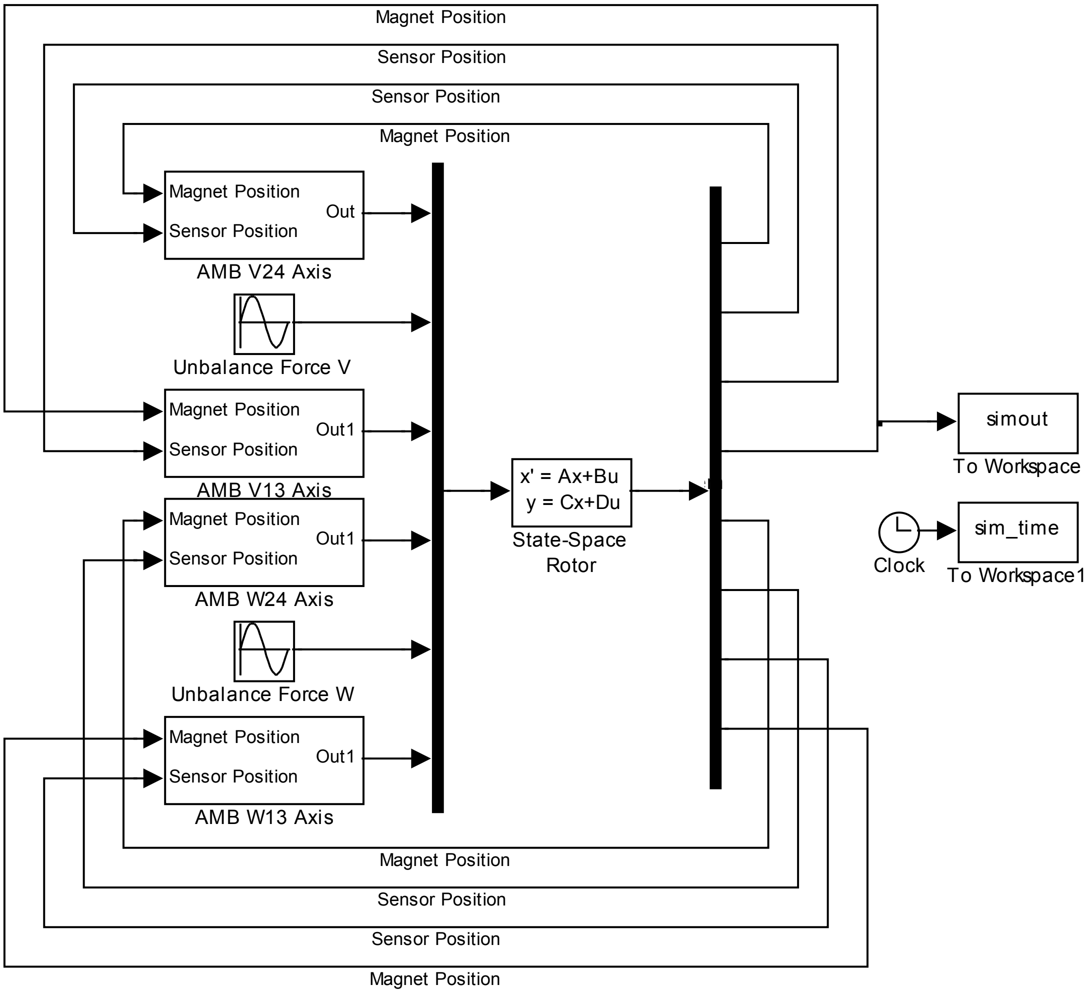

Figure 4.25 Simulink model used to test manufacturer provided PID control values.

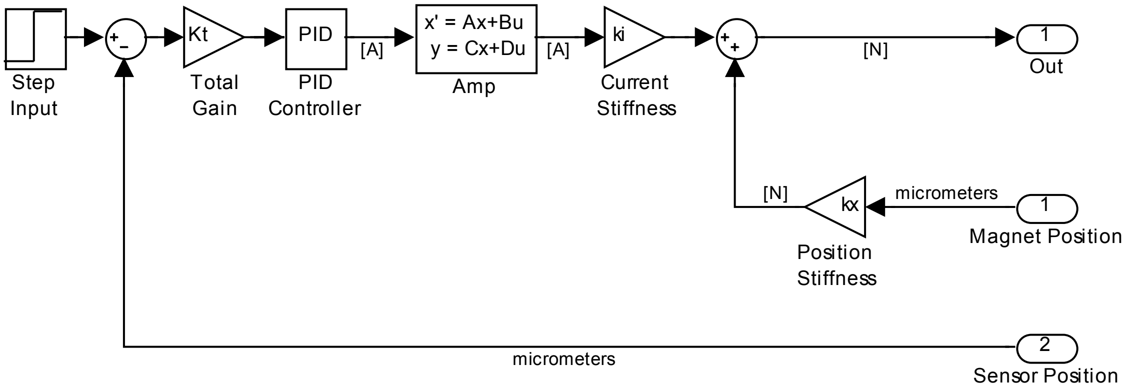

Figure 4.26 Model of controller and AMB used in Simulink model shown in Figure 4.25.

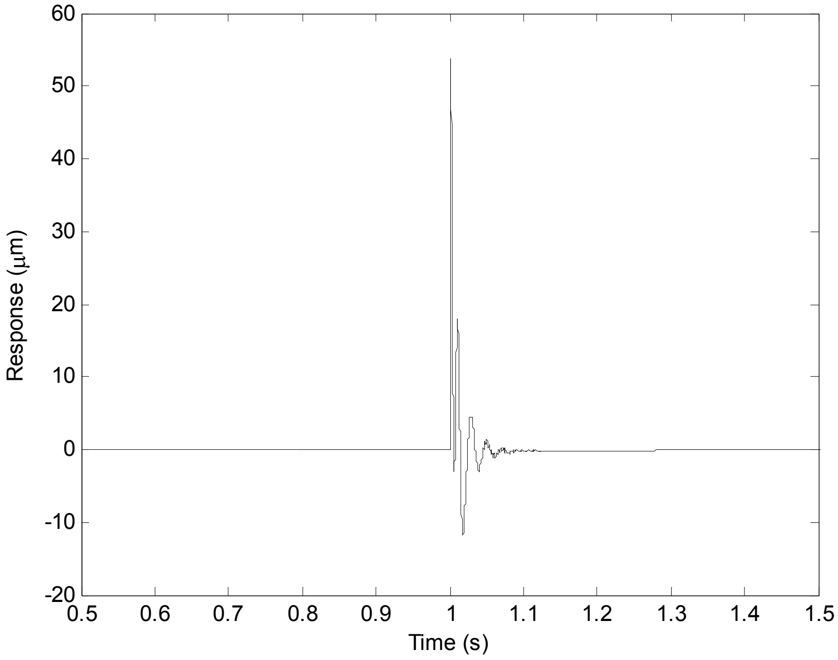

**Figure 4.27 Impulse response of simulated magnetically levitated rotor.**

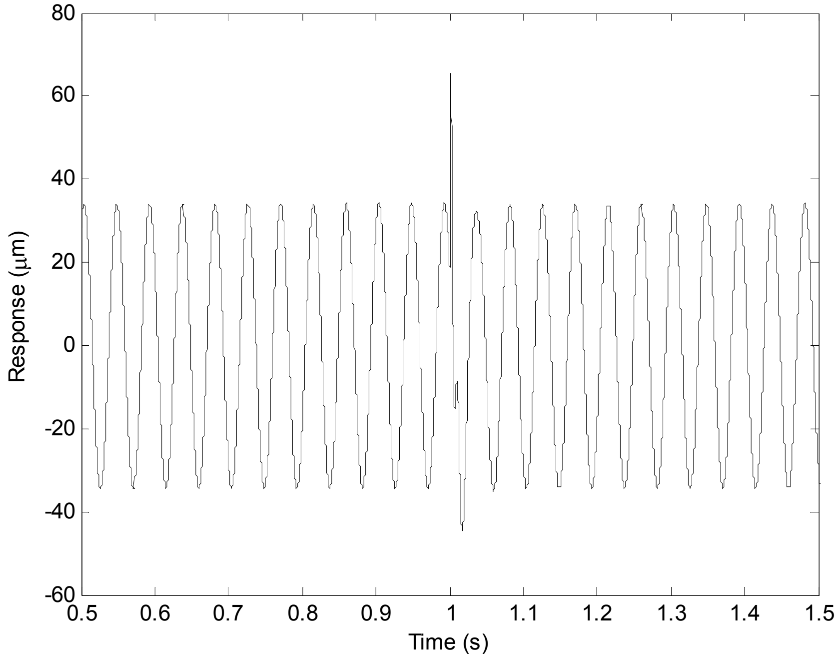

**Figure 4.28 Impulse response of simulated magnetically levitated rotor including force due to unbalance.**

If the nonlinear (more accurate) system is desired instead of the linear approximation, the model shown in Figure 4.29 can be used to represent a single magnetic bearing axis. The function in block "MB Force Function" is equation (3.2). The response is very similar to that shown in Figures 4.27 and 4.28 indicating the linearized current and position stiffnesses are a good approximation.

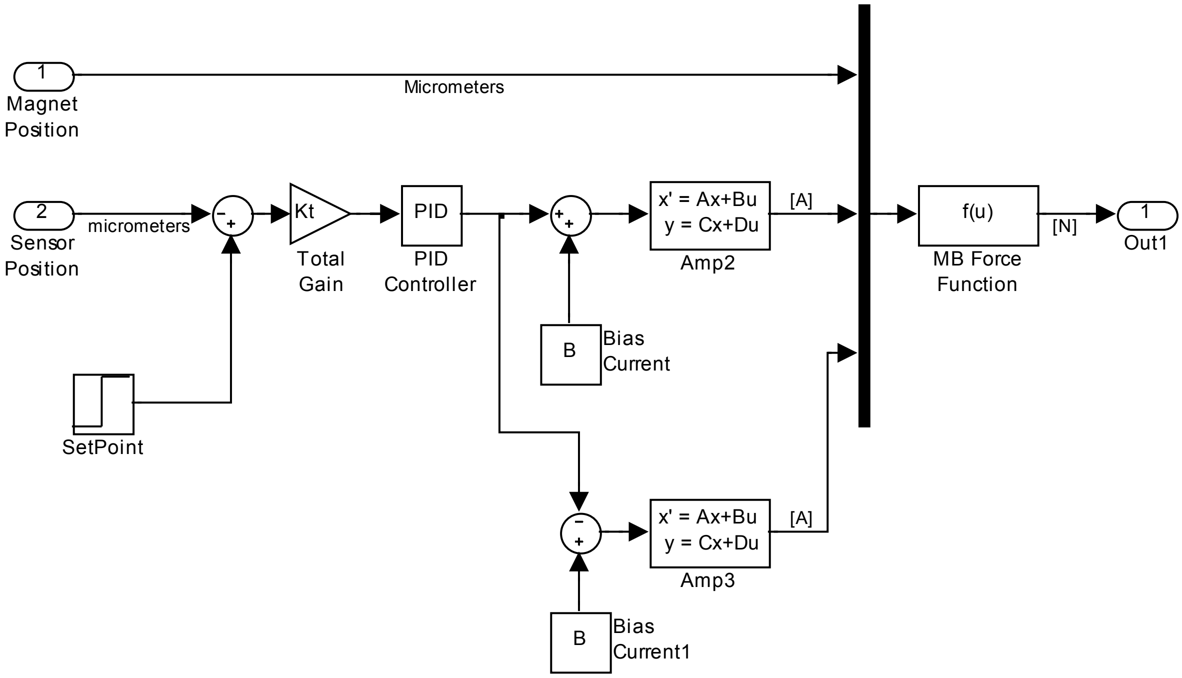

**Figure 4.29 Alternate model of controller and AMB used in Simulink model shown in Figure 4.21.**

### 4.3.2 Identification of Transfer Function

For system identification, the transfer function is found for the undamaged shaft trial and the 40% diameter EDM cut shaft trial. This is again done using MBScope Analyzer tool. Figure 4.30 below shows results for the healthy shaft and Figure 4.31 below shows the change in first natural frequency between the healthy rotor and the 40% cut rotor. The first natural frequency is expected to drop due to the decrease in stiffness of the shaft due to the damage.

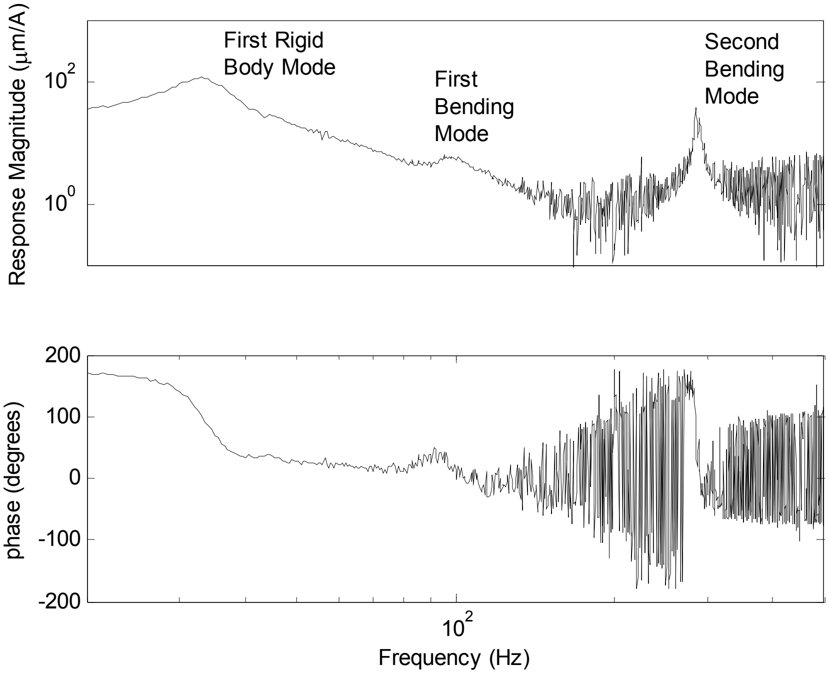

**Figure 4.30 Bode Plot of undamaged shaft on magnetic bearings. Input at magnetic bearing actuator and output at actuator sensor. Data collected using MBScope Analyzer tool.**

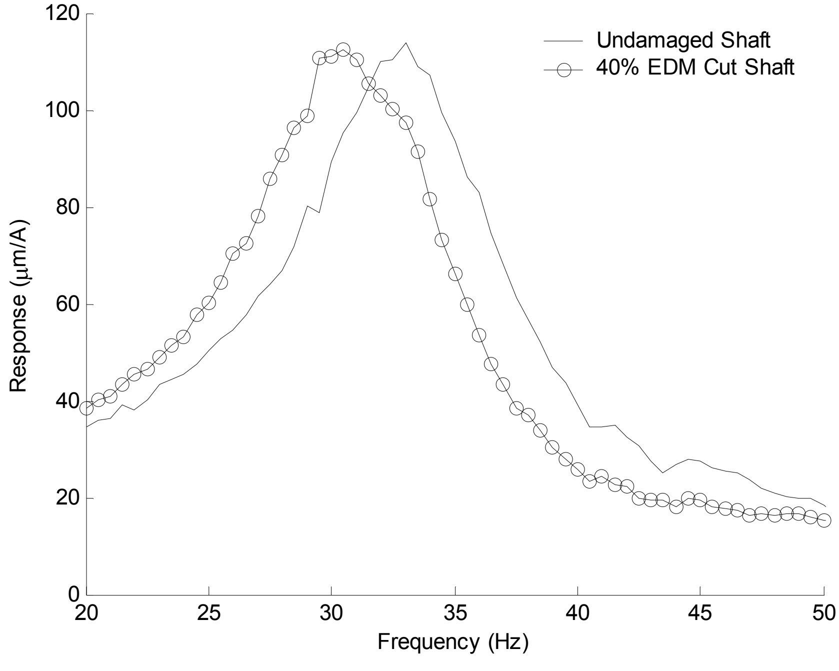

**Figure 4.31 Close up of first resonance peek of Figure 4.30. Transfer function of damaged shaft also included for comparison.**

### 4.3.3 Experimental Results: Healthy and Damaged Rotor

The rotor is levitated and spinning at constant speed. The sinusoidal current injection is superimposed on the levitation current in one axis of the AMB outboard from the drive motor. The resulting current in that axis is the sum of the control, bias, and injection currents. Despite the computer generated input harmonic force, the experimentally measured actual force is periodic with the dominant frequency equal to the injection frequency. The total current data and position data are collected and the force on the rotor is calculated with equation (3.2). Samples of the four force injection cases are shown in Figure 4.32. Unlike the ball bearing trials, the force is not about zero and there is force present even when no injection takes place. Figure 4.32 also shows the injection magnitude and frequency.

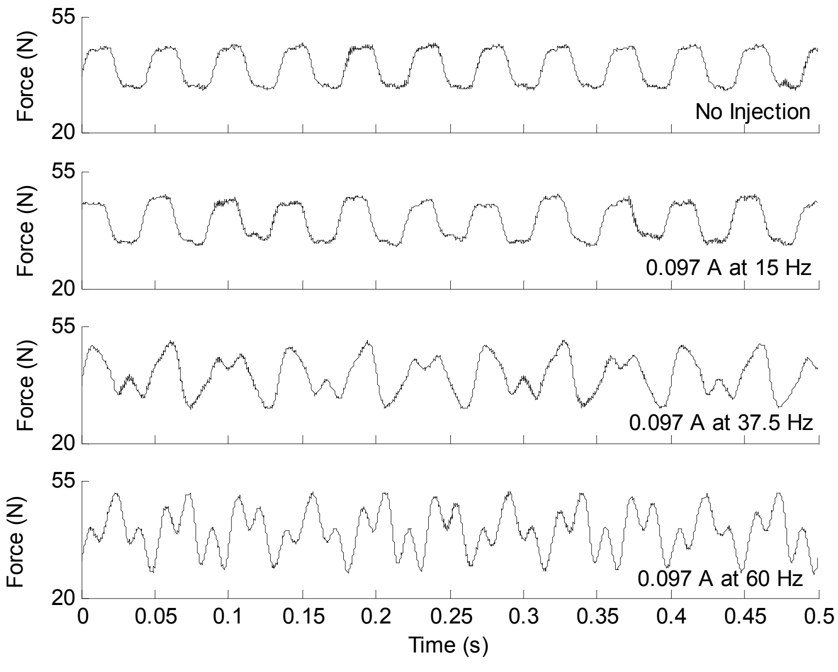

**Figure 4.32 Example of four force injection cases for magnetic bearing trials calculated from experimental current and position data using equation (3.2).**

Figures 4.33 through 4.36 show the frequency spectrums and comparison for the undamaged and 40% diameter EDM cut shafts for the four different injection cases. For no injection, Figure 4.33, the multiples of running speed can be seen in both rotors. There is a strong 2X difference as well as a small peeks at 3X and 4X. In Figure 4.34, when injection is at 15 Hz, some combined frequencies can be seen. The only difference between the damaged rotor and control rotor are what is seen when no injection is present and a peek at the injection frequency of 15 Hz. Figures 4.35 and 4.36, 37.5 Hz and 60 Hz injection respectfully, show significant combinational frequency excitation with a strong difference between the cut shaft and control shaft at the combined frequencies. Also, in addition to the running speed multiples differences seen in the no injection case, a 1X difference is observed.

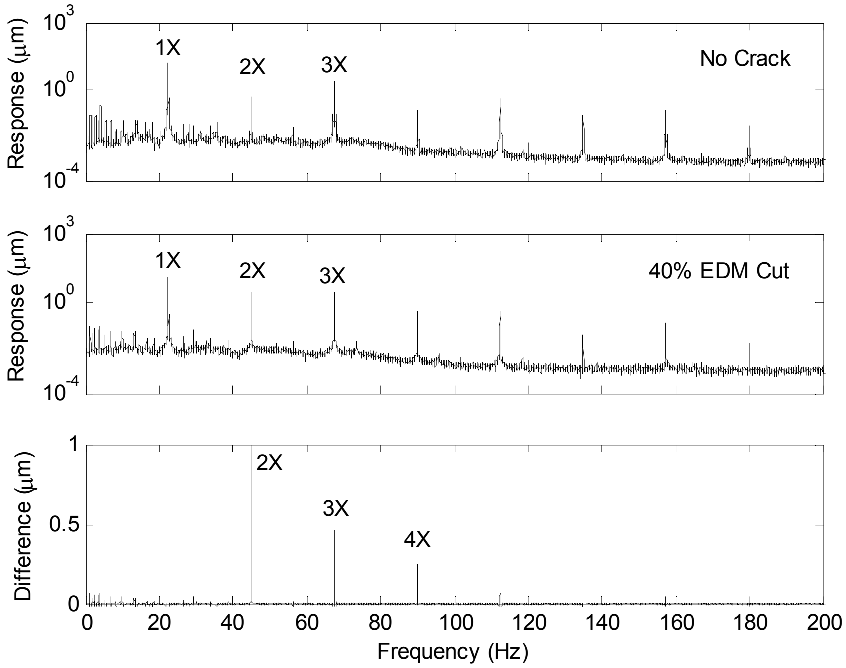

**Figure 4.33 Frequency spectrum of healthy shaft and 40% EDM (not filled) cut shaft rotating at 22.5 Hz on active magnetic bearings with no force injection.**

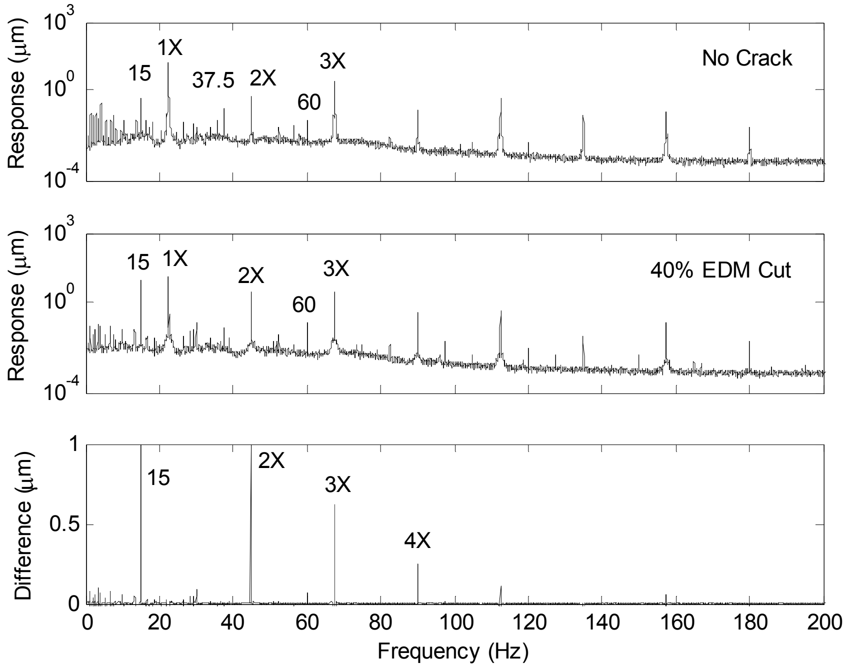

**Figure 4.34 Frequency spectrum of healthy shaft and 40% EDM (not filled) cut shaft rotating at 22.5 Hz on active magnetic bearings with force injection of 0.097 A at 15 Hz.**

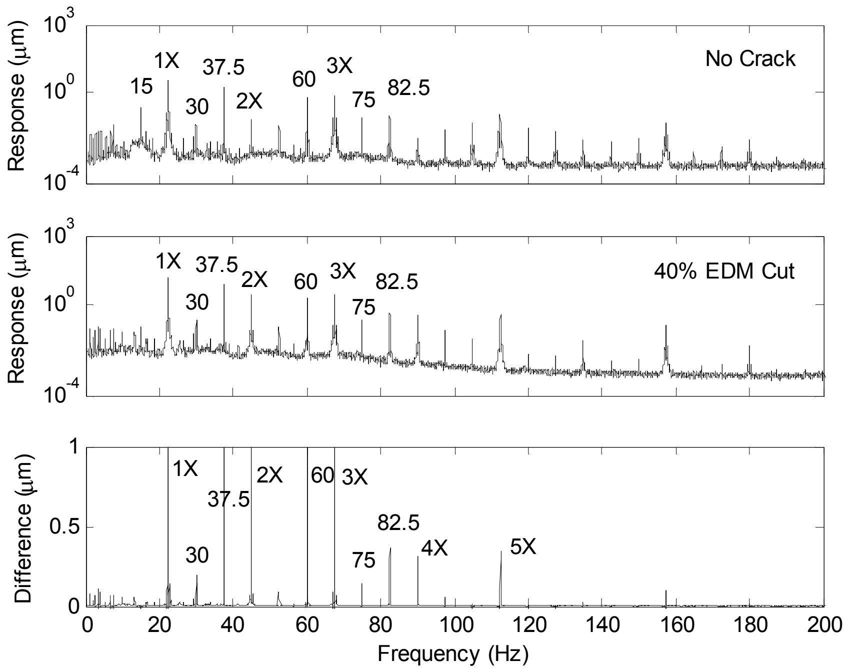

**Figure 4.35** Frequency spectrum of healthy shaft and 40% EDM (not filled) cut shaft rotating at 22.5 Hz on active magnetic bearings with force injection of 0.097 A at 37.5 Hz.

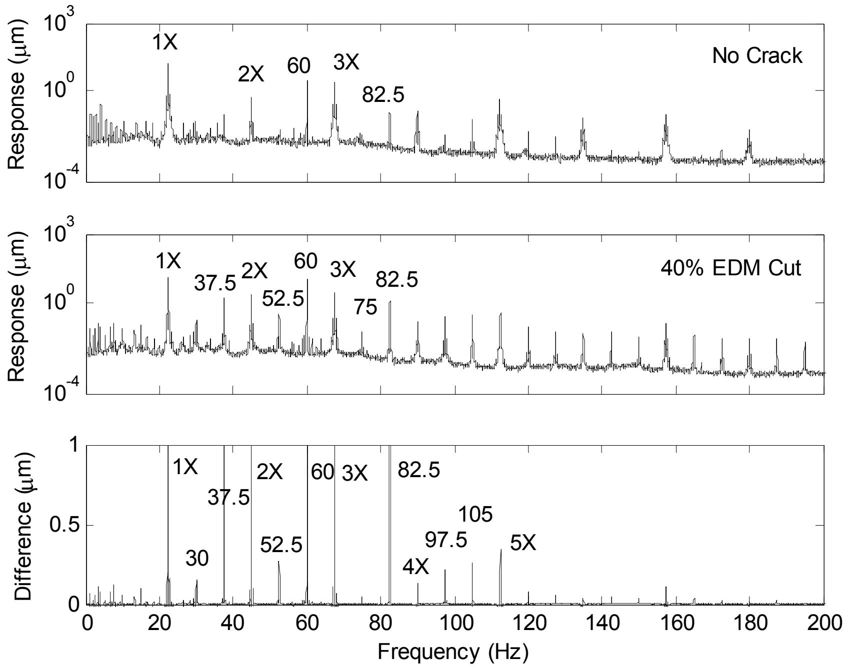

**Figure 4.36** Frequency spectrum of healthy shaft and 40% EDM (not filled) cut shaft rotating at 22.5 Hz on active magnetic bearings with force injection of 0.097 A at 60 Hz.

# CHAPTER V

# CONCLUSIONS

## 5.1 Contributions

Condition monitoring of machinery is a vast growing industry. In the last two decades a variety of approaches have been proposed to try to make use of the changes in the dynamics of a rotor to identify and possibly locate a crack (and other faults) in the rotor at an early stage in their development.

In this thesis, the modeling of the cracked Jeffcott rotor subjected to residual unbalance, gravity force and externally applied harmonic force excitation has been presented in attempt to use the changes in the dynamics of the rotor to identify the presence of a crack. The generated simulation results demonstrate that the use of an active magnetic bearing (AMB) to excite the rotor with a harmonic force at a carefully selected frequency produces components in the system response at many frequencies which are combinations of the rotor speed, the AMB excitation frequency and the system natural frequency which are not present in an un-cracked rotor.

In order to verify the predicted results an extensive experimental matrix has been followed using a dedicated crack detection experimental facility. The conducted experimental study involved external excitation applied between the supporting bearings and at the supporting bearing. In the first case the rotor was supported on ball bearings while in the second case the rotor was magnetically levitated. The PID controller, of which, was successfully developed for magnetic rotor levitation. A check of the stability and robustness of the controller has been carried out using MatLab Simulink.

This work contributes to the art of online health monitoring by experimentally confirming the presence of combinational frequencies in a cracked rotor's vibration. In most of the tested operating conditions, the measured rotor response for the cracked rotor exhibited the same frequency components as predicted in the simulation. Those components, being combination frequencies of three main, different system frequencies present in a system, have a potential to be used to detect cracks in the rotor. It is also a noteworthy contribution that the combination frequencies were also found in the response of the magnetically levitated cracked rotor with the excitation applied at the supporting bearing.

### 5.2 Further Research Directions

Further research is needed to make the presented approach a practical condition monitoring technique. Although AMB technology seems to lend itself naturally to the role of calibrated actuator or force transducer, accuracy limits are significant. Also, a more robust technique is needed to determine the presence, location and severity of a crack from the combination frequencies in the response. Furthermore the effect of adding an extra force to the system might encourage a faster crack growth, which is obviously a disadvantage. This method can be applied to magnetically levitated systems with no additional hardware, but for traditionally supported rotors, an additional component would have to be provided.

Areas of research needed to develop practical application of this crack detection method include the following. This simulation and experiment should be repeated for a wider range of parameters including but not limited to crack location and depth, rotor dimensions, operating speeds, and injection frequencies. This method should be tested using proper safety precautions on a rotor with a true crack. This method should be tested on an actual operable machine to serve as a case study in finding optimum force injection values and frequencies.

# BIBLIOGRAPHY

Adams, M.L., 2001, *Rotating Machinery Vibration. From Analysis to Troubleshooting*, Marcel Dekker, Inc., New York.

Baaklini, G., Gyekenyesi, A.L., Smith, K.D., Sawicki, J.T., and Brasche, L., 2002, "Structural Health Monitoring for On-Wing Engine Diagnostics", *Structural Health Monitoring Conference*, Paris, France, July 10-12.

Bash, T. 2005, "Active Magnetic Bearings used as an Actuator for Rotor Health Monitoring in Conjunction with Conventional Supported Bearings", Thesis, Virginia Polytechnic Institute and State University, Blacksburg, VA, USA

Bently, D.E., Muszynska, A., 1995, "Vibration Monitoring and Analysis for Rotating Machinery", *Noise and Vibration 1995 Conference*, Pretoria, South Africa, November, Keynote address paper, pp. 7-9.

Dimarogonas, A. D., 1996, "Vibration of Cracked Structures: A State of the Art Review", *Engineering Fracture Mechanics*, vol. 55 (5), pp. 831–857.

Dimentberg, F.M., 1961, *Flexural Vibrations of Rotating Shafts*, Butterworths, London, England

Doebling, S.W., Farrar, C.R., Prime, M.B., and Shevitz, D.W., 1996, Los Alamos National Laboratory Report LA-13070-MS.

Dimarogonas, A.D., 1973, “Newkirk Effect, Thermally Induced Dynamic Instability of High Speed Rotors”, *International Gas Turbine Conference*, Washington, D.C., ASME Paper No. 73-GT-26.

Dimarogonas, A.D., 1983, “Analytical Methods in Rotor Dynamics”, Applied Science Publishers, London.

Earnshaw, S., 1842, *On the Nature of the Molecular Forces Which Regulate the Constitution of the Lumiferous Ether*, Trans. Camb. Phil. Soc., 7, Part I: 97–112.

Ehrich, F., ed., 1992, *Handbook of Rotordynamics*, McGraw Hill Inc., New York.

Evans, D.J., Pusey, H.C., 2002, “Shock and Vibration Standards”, *Harris' Shock and Vibration Handbook, Fifth Edition*, McGraw-Hill, New York.

Gasch, R., 1976, “Dynamic Behaviour of a Simple Rotor with a Cross Sectional Crack”, *International Conference on Vibrations in Rotating Machinery*, IMechE , Paper C178/76, pp. 123-128.

Gasch, R.A., 1993, "Survey of the Dynamic Behavior of a Simple Rotating Shaft with a Transverse Crack", *Journal of Sound and Vibration*, Vol. 160, pp. 313-332.

Gasch, R. 2008 "Dynamic Behaviour of the Laval Rotor with a Transverse Crack", *Mechanical Systems and Signal Processing*, Vol. 22, pp. 790-804.

Gyekenyesi, A.L., Sawicki, J.T., and Baaklini, G., 2002, "Application of Vibration Monitoring Techniques for Damage Detection in Rotating Disks", *The 9th International Symposium on Transport Phenomena and Dynamics of Rotating Machinery*, ISROMAC-9, Honolulu, Hawaii, 10-14 February.

Ishida, Y., Tsuyoshi, I. 2006, "Detection of a Rotor Crack Using a Harmonic Excitation and Nonlinear Vibration Analysis", *Journal of Vibration and Acoustics*, Vol. 128, pp. 741-749.

Iwatsubo, T., Arii, S. and Oks, A., 1992, "Detection of a transverse crack in a rotor shaft by adding external force", *Proc. IMechE Vibrations in Rotating Machinery*, Vol. C432/093, pp. 275-282 .

Kasarda, M., Quinn, D.D., Bash, T., Mani, G., Inman, D., Kirk, R.G., Sawicki, J.T., 2005, "Magnetic Bearings for Non-destructive Health Monitoring of Rotating Machinery Supported in Conventional Bearings", *Key Engineering Materials*, Vols. 293-294, pp. 383-390.

Kellenberger, W., 1980, “Spiral Vibrations Due to Seal Rings in Turbogenerators. Thermally Induced Interaction between Rotor and Stator”, *ASME Journal of Mechanical Design*, Vol. 102, pp. 177-184.

Mani, G., Quinn, D., Kasarda, M. 2006, “Active Health Monitoring in a Rotating Cracked Shaft Using Active Magneitc Bearings as Force Actuators”, *Journal of Sound and Vibration*, Vol. 294, pp. 454-465.

Mani, G., Quinn, D.D., Kasarda, M.E.F., Inman, D.J. and Kirk, R.G., 2005, “Health Monitoring of Rotating Machinery Through External Forcing”, *Proceedings of ISCORMA-3*, Cleveland, Ohio, USA.

Mayes, I.W. and Davies, W.G.R., 1980, “A Method of Calculating the Vibrational Behaviour of Coupled Rotating Shafts Containing a Transverse Crack”, *International Conference on Vibrations in Rotating Machinery*, Paper C254/80, IMechE, pp. 17-27.

Mayes, I. W. and Davies, W. G. R., 1984, “Analysis of the Response of a Multi-Rotor-Bearing System Containing a Transverse Crack in a Rotor”, *ASME Journal of Vibration, Acoustics, Stress, and Reliability in Design,* Vol. 106, pp. 139-145.

Mitchell, J.S., 1993, *Introduction to Machinery Analysis and Monitoring, Second Edition*, Penn Well Books, Tulsa, OK.

Muszynska, A., 1993, "Thermal Rub Effect in Rotating Machines," *ORBIT*, Vol. 14, No. 1, pp. 8-13.

Morton, P.G., 1975, "The Derivation of Bearing Characteristics by Means of Transient Excitation Applied Directly to a Rotating Shaft", *UTAM Symposium, Dynamics of Rotors*, pp. 350-370.

Muszynska, A., 1995, "Vibrational Diagnostics of Rotating Machinery Malfunctions", *International Journal of Rotating Machinery*, vol. 1, no. 3-4, pp. 237-266..

Newkirk, B.L., 1926, "Shaft Rubbing. Relative Freedom of Rotor Shafts from Sensitiveness to Rubbing Contact When Running Above Their Critical Speeds", *Mechanical Engineering*, vol. 48, No. 8, pp. 830-832.

Nordmann, R., Aenis, M., 2004, "Fault Diagnosis in a Centrifugal Pump Using Active Magnetic Bearings", *International Journal of Rotating Machinery*, Vol. 10(3), pp. 183-191.

Nordmann, R. and Schollhorn, K., 1984, "Identification of Modal Parameters of an Elastic Rotor with Oil Film Bearings", *ASME Journal of Vibration, Acoustics, Stress, and Reliability in Design*, Vol. 106.

Penny, J., Friswell, M., Zhou, C., 2006, "Condition Monitoring of Rotating Machinery Using Active Magnetic Bearings", *Proceedings of ISMA 2006*, pp. 3497-3506.

Plonus, M. A., 1978, "Applied Electromagnetics", McGraw-Hill, New York, pp. 410, 414-416.

Pusey, H.C., 1999, "An Assessment of Turbomachinery Condition Monitoring and Failure Prognosis Technology", *Proceedings of 17th International Modal Analysis Conference*, Kissimmee, FL, February, pp. 1310-1316.

Quinn, D., Mani, G., Kasarda, M., Bash, T., Inman, J., Kirk, G., 2005, "Damage Detection of a Rotating Cracked Shaft Using an Active Magnetic Bearing as a Force Actuator – Analysis and Experimental Verification", *IEEE/ASME Transactions on Mechatronics*, Vol. 10, No. 6, pp. 640-647.

Rieger, N.F., McCloskey, T.H., and Dewey, R.P., 1990, "The High Cost of Failure of Rotating Equipment", *Proceedings of 44th Meeting of the Mechanical Failure Prevention Group*, Vibration Institute.

Sawicki, J.T., 2002, "Some Advances in Diagnostics of Rotating Machinery Malfunctions", *Proceedings of the Int. Symposium on Machine Condition Monitoring and Diagnosis*, The University of Tokyo, Tokyo, pp. 138-143.

Sawicki, J., Friswell, M., Pesch, A., Wroblewski, A., 2008, “Condition Monitoring of Rotor Using Active Magnetic Actuator”, *Proceedings of ASME Turbo Expo 2008: Power for Land Sea and Air*, Berlin, Germany.

Sawicki, J.T., Genta, G., 2001, “Modal Uncoupling of Damped Gyroscopic Systems”, *Journal of Sound and Vibration*, vol. 244(3), pp. 431-451.

Sawicki, J.T., Montilla-Bravo, A., and Gosiewski, Z., 2003, “Thermo-Mechanical Behavior of Rotor with Rubbing”, *International Journal of Rotating Machinery*. Vol. 9(1), pp. 41-47.

Sawicki, J.T., Padovan, J., and Al-Khatib, R., 1999, “The Dynamics of Rotor with Rubbing”, *International Journal of Rotating Machinery*, Vol. 5, no. 4, pp. 295-304.

Taylor, H.D., 1924, “Rubbing Shafts Above and Below the Critical Speed”, *General Electric Review,* Vol. 27.

Tonnesen, J. and Lund, J., 1988, “Experimental techniques for rotordynamic analysis”, *CISM Course No. 297, Rotordynamics 2*.

Wauer, J., 1990, “On the Dynamics of Cracked Rotors:  A Literature Survey”, *Trans. ASME, J. Appl. Mech.*, Vol. 43, pp. 13-17.

# APPENDICES

# APPENDIX A

# MAGNETIC BEARING SPECIFICATIONS

| | | |
|---|---|---|
| **A.1** | **Bearing Performance Specifications** | |
| | Static Load Capacity | 60 lbf |
| | Saturation Current | 3.00 A |
| | | |
| | ***Class A Tuning (Bias = 1.5 A)*** | |
| | Dynamic Load Capacity (@ Freq) | 11 lbf |
| | Frequency | 1000 Hz |
| | Current Stiffness ($K_i$) | 40.77 lbf/amp |
| | Position Stiffness ($K_x$) | 3804.2 lbf/in |
| **A.2** | **Bearing Geometry** | |
| | Number Of Poles Per Quadrant | 2 |
| | Stator Stack Length | 0.850 in |
| | Stator OD | 4.528 in |
| | Stator ID | 1.920 in |
| | Rotor OD | 1.890 in |
| | Rotor lamination ID | 1.197 in |
| | Nominal Gap | 0.015 in |
| | Pole Width | 0.514 in |
| | Pole Height | 0.742 in |
| | Slot Width (at ID) | 0.233 in |
| | Pole Centreline Angle | 22.5° |
| **A.3** | **Material Properties** | |
| | Material Grade: Stator | M-19, C-5 |
| | Rotor | Arnon 5, C-5 |
| | Saturation Flux Density | 1.25 T |
| | Relative Permeability | 3000 |
| | Lamination Thickness: Stator | 0.014 in |
| | Rotor | 0.005 in |
| | Material Resistivity | 18.9 μΩ-in |
| | Density | 0.276 lb/in$^3$ |
| | Temperature | 1350°F |
| | Insulation | C-5 Both Sides |
| | Stacking Factor | 96% |

| | | |
|---|---|---|
| **A.4** | **Coil Specifications** | |
| | Wire Gauge | 23 AWG |
| | Wire type | Hyslik 200 heavy/round |
| | Coil Insulation | 0.0135 in |
| | Packing Factor | 97% |
| | Turns Per Coil (N) | 124 |
| | Coil Extension (max) | 0.200 in |
| | Quadrant Resistance (calculated) | 1.578 Ω |
| | Quadrant Inductance (nominal) | 20 mH |
| **A.5** | **Power Amplifier Specifications** | |
| | Maximum Continuous Current | 3 A |
| | Peak Current | 10 amp for 2 seconds |
| | Max DC Supply Voltage | 48V unregulated |
| | Minimum Required Voltage | 38.67 V |
| | Minimum Load Inductance | 250 μH |
| | Switching Frequency | 20 kHz |
| | Power Dissipation @ Cont. Current | 20 W |
| **A.6** | **Position Sensor Specifications** | |
| | Type | Variable Reluctance |
| | Number per axis | 2 |
| **A.7** | **Speed Sensor** | |
| | Type | Hall Effect |
| **A.8** | **MBForce Coefficients** | |
| | Calibration Factor (C) | 19.826 N-$\mu m^2/A^2$ |
| | Effective Gap (gap) | 401.55 μm |

# APPENDIX B

## XLRotor Input File

### B.1 Rotor on Ball Bearing Supports

**INPUT TABLE OF BEAM AND STATION DEFINITIONS, MORE THAN ONE BEAM PER STATION IS OK**

| Station | Length | OD Left | ID Left | OD Right | ID Right |
|---|---|---|---|---|---|
| # | meters | meters | meters | meters | meters |
| 1 | 0.022225 | 0.015875 | 0 | 0.015875 | 0 |
| 2 | 0.010795 | 0.015875 | 0 | 0.015875 | 0 |
| 3 | 0.0254 | 0.015875 | 0 | 0.015875 | 0 |
| 3 | 0.0254 | 0.0381 | 0.015875 | 0.0479 | 0.015875 |
| 4 | 0.01164167 | 0.015875 | 0 | 0.015875 | 0 |
| 4 | 0.01164167 | 0.0479 | 0.015875 | 0.0479 | 0.015875 |
| 5 | 0.01164167 | 0.015875 | 0 | 0.015875 | 0 |
| 5 | 0.01164167 | 0.0479 | 0.015875 | 0.0479 | 0.015875 |
| 6 | 0.01164167 | 0.015875 | 0 | 0.015875 | 0 |
| 6 | 0.01164167 | 0.0479 | 0.015875 | 0.0479 | 0.015875 |
| 7 | 0.03381375 | 0.015875 | 0 | 0.015875 | 0 |
| 8 | 0.03381375 | 0.015875 | 0 | 0.015875 | 0 |
| 9 | 0.03381375 | 0.015875 | 0 | 0.015875 | 0 |
| 10 | 0.03381375 | 0.015875 | 0 | 0.015875 | 0 |
| 11 | 0.01508125 | 0.015875 | 0 | 0.015875 | 0 |
| 11 | 0.01508125 | 0.0479 | 0.015875 | 0.0479 | 0.015875 |
| 12 | 0.01508125 | 0.015875 | 0 | 0.015875 | 0 |
| 12 | 0.01508125 | 0.0479 | 0.015875 | 0.0479 | 0.015875 |
| 13 | 0.01508125 | 0.015875 | 0 | 0.015875 | 0 |
| 13 | 0.01508125 | 0.0479 | 0.015875 | 0.0479 | 0.015875 |
| 14 | 0.01508125 | 0.015875 | 0 | 0.015875 | 0 |
| 14 | 0.01508125 | 0.0479 | 0.015875 | 0.0479 | 0.015875 |
| 15 | 0.0254 | 0.015875 | 0 | 0.015875 | 0 |
| 16 | 0.0254 | 0.015875 | 0 | 0.015875 | 0 |
| 17 | 0.0155 | 0.015875 | 0 | 0.015875 | 0 |
| 17 | 0.0155 | 0.127 | 0.015875 | 0.127 | 0.015875 |
| 18 | 0.0155 | 0.015875 | 0 | 0.015875 | 0 |
| 18 | 0.0155 | 0.127 | 0.015875 | 0.127 | 0.015875 |
| 19 | 0.012 | 0.015875 | 0 | 0.015875 | 0 |
| 19 | 0.012 | 0.03 | 0.015875 | 0.03 | 0.015875 |
| 20 | 0.021 | 0.015875 | 0 | 0.015875 | 0 |
| 20 | 0.021 | 0.035 | 0.015875 | 0.035 | 0.015875 |
| 21 | 0.007755 | 0.015875 | 0 | 0.015875 | 0 |
| 22 | 0.041275 | 0.015875 | 0 | 0.015875 | 0 |
| 23 | 0.041275 | 0.015875 | 0 | 0.015875 | 0 |

| | | | | | |
|---|---|---|---|---|---|
| 24 | 0.041275 | 0.015875 | 0 | 0.015875 | 0 |
| 25 | 0.01164167 | 0.015875 | 0 | 0.015875 | 0 |
| 25 | 0.01164167 | 0.0479 | 0.015875 | 0.0479 | 0.015875 |
| 26 | 0.01164167 | 0.015875 | 0 | 0.015875 | 0 |
| 26 | 0.01164167 | 0.0479 | 0.015875 | 0.0479 | 0.015875 |
| 27 | 0.01164167 | 0.015875 | 0 | 0.015875 | 0 |
| 27 | 0.01164167 | 0.0479 | 0.015875 | 0.0479 | 0.015875 |
| 28 | 0.0254 | 0.015875 | 0 | 0.015875 | 0 |
| 28 | 0.0254 | 0.0479 | 0.015875 | 0.0381 | 0.015875 |
| 29 | 0.010795 | 0.015875 | 0 | 0.015875 | 0 |
| 30 | 0.04445 | 0.015875 | 0 | 0.015875 | 0 |
| 31 | 0.009525 | 0.009525 | 0 | 0.009525 | 0 |
| 32 | 0 | 0 | 0 | 0 | 0 |

## B.2 Magnetically Levitated Rotor

**INPUT TABLE OF BEAM AND STATION DEFINITIONS, MORE THAN ONE BEAM PER STATION IS OK**

| Station # | Length meters | OD Left meters | ID Left meters | OD Right meters | ID Right meters |
|---|---|---|---|---|---|
| 1 | 0.02223 | 0.015875 | 0 | 0.015875 | 0 |
| 2 | 0.0084 | 0.015875 | 0 | 0.015875 | 0 |
| 3 | 0.0127 | 0.015875 | 0 | 0.015875 | 0 |
| 3 | 0.0127 | 0.0381 | 0.015875 | 0.042862 | 0.015875 |
| 4 | 0.0127 | 0.015875 | 0 | 0.015875 | 0 |
| 4 | 0.0127 | 0.042862 | 0.015875 | 0.047625 | 0.015875 |
| 5 | 0.0116 | 0.015875 | 0 | 0.015875 | 0 |
| 5 | 0.0116 | 0.047625 | 0.015875 | 0.047625 | 0.015875 |
| 6 | 0.0116 | 0.015875 | 0 | 0.015875 | 0 |
| 6 | 0.0116 | 0.047625 | 0.015875 | 0.047625 | 0.015875 |
| 7 | 0.0116 | 0.015875 | 0 | 0.015875 | 0 |
| 7 | 0.0116 | 0.047625 | 0.015875 | 0.047625 | 0.015875 |
| 8 | 0.0285 | 0.015875 | 0 | 0.015875 | 0 |
| 9 | 0.0342 | 0.015875 | 0 | 0.015875 | 0 |
| 10 | 0.0342 | 0.015875 | 0 | 0.015875 | 0 |
| 11 | 0.0342 | 0.015875 | 0 | 0.015875 | 0 |
| 12 | 0.01508 | 0.015875 | 0 | 0.015875 | 0 |
| 12 | 0.01508 | 0.047625 | 0.015875 | 0.047625 | 0.015875 |
| 13 | 0.01508 | 0.015875 | 0 | 0.015875 | 0 |
| 13 | 0.01508 | 0.047625 | 0.015875 | 0.047625 | 0.015875 |
| 14 | 0.01508 | 0.015875 | 0 | 0.015875 | 0 |
| 14 | 0.01508 | 0.047625 | 0.015875 | 0.047625 | 0.015875 |
| 15 | 0.01508 | 0.015875 | 0 | 0.015875 | 0 |
| 15 | 0.01508 | 0.047625 | 0.015875 | 0.047625 | 0.015875 |

| | | | | | |
|---|---|---|---|---|---|
| 16 | 0.0254 | 0.015875 | 0 | 0.015875 | 0 |
| 17 | 0.0254 | 0.015875 | 0 | 0.015875 | 0 |
| 18 | 0.00635 | 0.015875 | 0 | 0.015875 | 0 |
| 18 | 0.00635 | 0.041275 | 0.015875 | 0.041275 | 0.015875 |
| 19 | 0.0127 | 0.015875 | 0 | 0.015875 | 0 |
| 19 | 0.0127 | 0.127 | 0.015875 | 0.127 | 0.015875 |
| 20 | 0.00635 | 0.015875 | 0 | 0.015875 | 0 |
| 20 | 0.00635 | 0.041275 | 0.015875 | 0.041275 | 0.015875 |
| 21 | 0.0413 | 0.015875 | 0 | 0.015875 | 0 |
| 22 | 0.0413 | 0.015875 | 0 | 0.015875 | 0 |
| 23 | 0.0413 | 0.015875 | 0 | 0.015875 | 0 |
| 24 | 0.0556 | 0.015875 | 0 | 0.015875 | 0 |
| 25 | 0.0116 | 0.015875 | 0 | 0.015875 | 0 |
| 25 | 0.0116 | 0.047625 | 0.015875 | 0.047625 | 0.015875 |
| 26 | 0.0116 | 0.015875 | 0 | 0.015875 | 0 |
| 26 | 0.0116 | 0.047625 | 0.015875 | 0.047625 | 0.015875 |
| 27 | 0.0116 | 0.015875 | 0 | 0.015875 | 0 |
| 27 | 0.0116 | 0.047625 | 0.015875 | 0.047625 | 0.015875 |
| 28 | 0.0127 | 0.015875 | 0 | 0.015875 | 0 |
| 28 | 0.0127 | 0.047625 | 0.015875 | 0.042862 | 0.015875 |
| 29 | 0.0127 | 0.015875 | 0 | 0.015875 | 0 |
| 29 | 0.0127 | 0.042862 | 0.015875 | 0.0381 | 0.015875 |
| 30 | 0.0084 | 0.015875 | 0 | 0.015875 | 0 |
| 31 | 0.04445 | 0.015875 | 0 | 0.015875 | 0 |
| 32 | 0.00953 | 0.009525 | 0 | 0.009525 | 0 |
| 33 | 0 | 0 | 0 | 0 | 0 |

## APPENDIX C

## Testing Matrix

### C.1 Ball Bearing Support Trials

| | No Injection | 18 Hz Injection | 45 Hz Injection | 72 Hz Injection |
|---|---|---|---|---|
| Healthy Shaft | X | X | X | X |
| 25% Dia EDM Cut Shaft | X | X | X | X |
| 40% Dia EDM Cut Shaft | X | X | X | X |
| Filled 25% Dia EDM Cut Shaft | X | X | X | X |
| Filled 40% Dia EDM Cut Shaft | X | X | X | X |

### C.2 AMB Support Trials

| | No Injection | 15 Hz Injection | 37.5 Hz Injection | 60 Hz Injection |
|---|---|---|---|---|
| Healthy Shaft | X | X | X | X |
| 40% Dia EDM Cut Shaft | X | X | X | X |

# APPENDIX D

## Experimental Results Summary

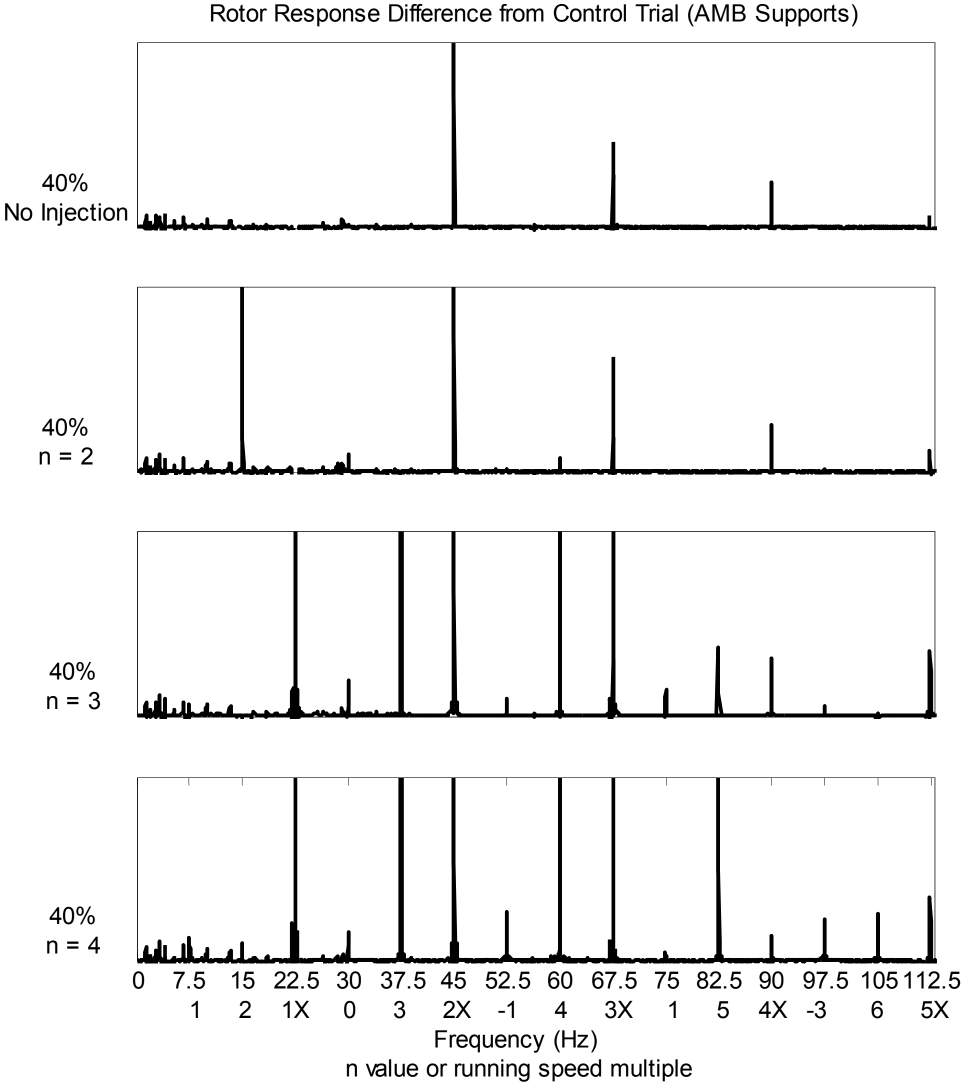

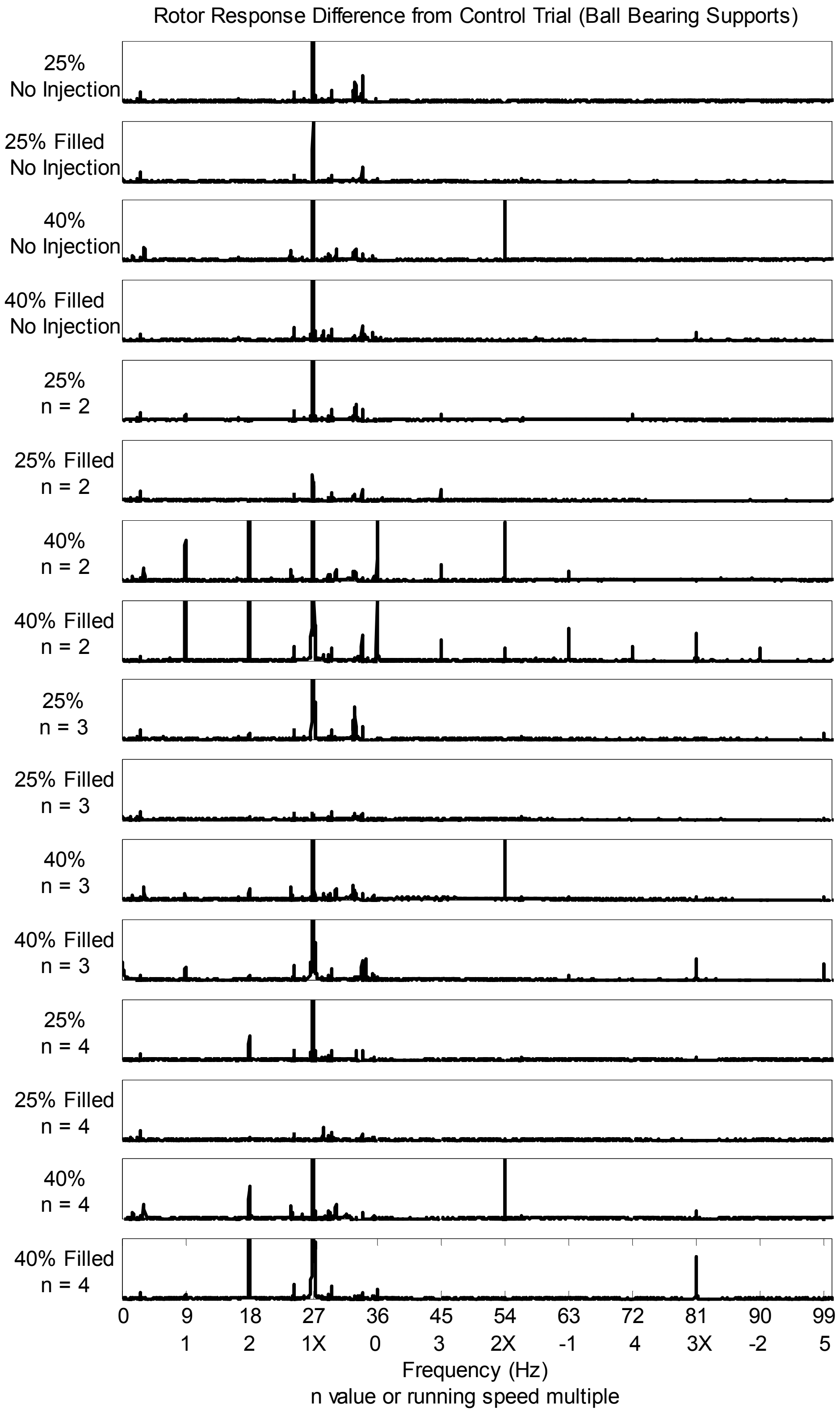
Rotor Response Difference from Control Trial (Ball Bearing Supports)
25% No Injection
25% Filled No Injection
40% No Injection
40% Filled No Injection
25% n = 2
25% Filled n = 2
40% n = 2
40% Filled n = 2
25% n = 3
25% Filled n = 3
40% n = 3
40% Filled n = 3
25% n = 4
25% Filled n = 4
40% n = 4
40% Filled n = 4
0
9
18
27
36
45
54
63
72
81
90
99
1
2
1X
0
3
2X
-1
4
3X
-2
5
Frequency (Hz)
n value or running speed multiple